

Durham E-Theses

A Compact, High Resolution Hyperspectral Imager for Remote Sensing of Soil Moisture

GRAHAM, CHRISTOPHER,JOHN

How to cite:

GRAHAM, CHRISTOPHER,JOHN (2023) *A Compact, High Resolution Hyperspectral Imager for Remote Sensing of Soil Moisture*, Durham theses, Durham University. Available at Durham E-Theses Online: <http://etheses.dur.ac.uk/15151/>

Use policy



This work is licensed under a [Creative Commons Attribution 3.0 \(CC BY\)](https://creativecommons.org/licenses/by/3.0/)

A Compact, High Resolution Hyperspectral Imager for Remote Sensing of Soil Moisture

Christopher Graham

A thesis presented for the degree of
Doctor of Philosophy



Centre for Advanced Instrumentation
The University of Durham
United Kingdom
January 2023

A Compact, High Resolution Hyperspectral Imager for Remote Sensing of Soil Moisture

Christopher Graham

Abstract

Measurement of soil moisture content is a key challenge across a variety of fields, ranging from civil engineering through to defence and agriculture. While dedicated satellite platforms like SMAP and SMOS provide high spatial coverage, their low spatial resolution limits their application to larger regional studies. The advent of compact, high lift capacity UAVs has enabled small scale surveys of specific farmland sites.

This thesis presents work on the development of a compact, high spatial and spectral resolution hyperspectral imager, designed for remote measurement of soil moisture content. The optical design of the system incorporates a bespoke freeform blazed diffraction grating, providing higher optical performance at a similar aperture to conventional Offner-Christoph designs.

The key challenges of UAV-borne hyperspectral imaging relate to using only solar illumination, with both intermittent cloud cover and atmospheric water absorption creating challenges in obtaining accurate reflectance measurements. A hardware based calibration channel for mitigating cloud cover effects is introduced, along with a comparison of methods for recovering soil moisture content from reflectance data under varying illumination conditions. The data processing pipeline required to process the raw pushbroom data into georectified images is also discussed.

Finally, preliminary work on applying soil moisture techniques to leaf imaging are presented.

Supervisors: Cyril Bourgenot and John Girkin

Acknowledgements

Firstly, I would like to thank my supervisors, Cyril Bourgenot and John Girkin for their support and mentorship throughout the last three and a half years. Their endless enthusiasm was an inspiration, even throughout the long lockdowns. I would also like to thank Patrick Stowell and Anthony Brown for their invaluable help in all things UAV, without whom this project would have never gotten off the ground.

I have to thank everyone within CfAI. Despite the strange world of lockdowns and social distancing, I've had a incredible time thanks to the brilliant atmosphere in the group. Special thanks must go to the students and postdocs of the Biophotonics group, with the weekly meetings about anything and everything being a highlight of the first lockdown. Many thanks also to my office mates in 011 (Craig, Jeremi, Lily, Polly, and Puttiwat...) as well as all of the other PhD students for the continuous distractions and discussions, and generally making CfAI such a great place to do a PhD.

Many thanks to long time friends Tom N, Jordan, and Tom L, for preserving my sanity through the lockdowns and write-up.

Lastly, I would like to thank my parents and family, for their constant support and encouragement through the years.

Contents

Declaration	vi
List of Figures	vii
List of Tables	xv
Nomenclature	xvi
1 Introduction	1
1.1 Remote Sensing and Hyperspectral Imaging	1
1.1.1 Early Remote Sensing	1
1.1.2 Hyperspectral Imagers	3
1.1.3 Commercial Market	6
1.1.4 Modern Instrumentation	8
1.2 Hyperspectral Remote Sensing in Precision Agriculture	9
1.2.1 Environmental Impacts of Agriculture	9
1.2.2 Precision Agriculture	10
1.2.3 Soil Moisture Measurement Methods	12
1.3 Thesis Outline	16
2 Technical Background and Theory	18
2.1 Fundamentals of hyperspectral imagery	18

2.1.1	Spatial Scanners	19
2.1.2	Spectral Scanners	22
2.1.3	Snapshot Imagers	23
2.2	Remote Soil Moisture Measurement	27
2.2.1	Spectral Indices	27
2.2.2	Index Space Methods	29
2.2.3	Spectral Shape Fitting	31
3	Instrument Design	37
3.1	Freeform Optics	37
3.2	Design Overview	39
3.3	Spectral Calibration and Throughput Testing	46
3.4	Camera Selection	47
3.5	Dual Channel Variant (to be finalised)	50
3.6	Enclosure	54
4	Fibre Optic Downwelling Irradiance Sensor	56
4.1	Fibre Calibration Channel	56
4.2	Throughput Analysis	59
4.3	Optical Design	63
4.4	Calibration Method	65
4.5	Demonstration	66
4.6	Conclusion	71
5	Data Collection & Data Processing	73
5.1	Overview	73
5.2	Lab & Ground Based Processing	74
5.3	Index Selection Method	77
5.4	Radiative Transfer Models	88
5.4.1	Method Discussion	93
5.5	Conclusion	94

6	Drone Integration	96
6.1	Hardware Changes	96
6.2	UAV Data Collection	97
6.3	UAV Data Processing	99
6.4	Conclusion	108
7	Other agricultural uses	109
7.1	Importance of Measuring Crop Stress	109
7.1.1	Leaf Water Content Experiment	110
7.1.2	Results	110
7.2	Conclusions	113
8	Conclusions	114
8.1	Summary	114
8.2	Future Work	116
	Bibliography	122

Declaration

The work in this thesis is based on research carried out at the Centre for Advanced Instrumentation, Department of Physics, University of Durham, England. No part of this thesis has been submitted elsewhere for any other degree or qualification, and it is the sole work of the author unless referenced to the contrary in the text.

Some of the work presented in this thesis has been published in journals and conference proceedings - the relevant publications are listed below.

Publications

Christopher Graham, John M. Girkin, and Cyril Bourgenot, "Freeform based hYperspectral imager for MOisture Sensing (FYMOS)," *Optics Express* 29, 16007-16018 (2021)

Graham, C., Girkin, J. & Bourgenot, C. Spectral index selection method for remote moisture sensing under challenging illumination conditions. *Scientific Reports* 12, 14555 (2022)

Christopher Graham, John M. Girkin, and Cyril Bourgenot, "Integrated fiber optic spectrally resolved downwelling irradiance sensor for pushbroom spectrometers," *Optics Express* 30, 45592-45598 (2022)

Copyright © 2023 by Christopher Graham.

"The copyright of this thesis rests with the author. No quotation from it should be published without the author's prior written consent and information derived from it should be acknowledged".

List of Figures

1.1	Early "unmanned" aerial photography, using camera equipped carrier pigeons. From https://publicdomainreview.org/collection/dr-julius-neubronner-s-miniature-pigeon-camera	2
1.2	Example photograph taken using Aerochrome film. The film maps infrared, red and green light to a red, green and blue respectively as a false colour image. Note the red colour of vegetation due to its high infrared reflectance. Photo courtesy of Rob Walwyn: https://www.robwalwyn.com/aerochrome	3
1.3	AVIRIS "Advertising" image, courtesy NASA/JPL-Caltech.	5
1.4	Trend showing the number of research papers per year containing the keywords "UAV" and "Hyperspectral" since 1990, as collated from Google Scholar	7
1.5	Terra/MODIS image of the UK on 10th August 2022 during heat-wave, courtesy of NASA Worldview. Worldview is part of the NASA Earth Observing System Data and Information System (EOSDIS) (https://worldview.earthdata.nasa.gov/)	11
1.6	Example soil sensors at Spen Farm. (a) Shows an unplanted soil sensor, (b) shows the main hub, with cables running outwards towards planted soil sensors. Photo Credit: Murilo Vianna	13

2.1	The main hyperspectral acquisition methods: (A) whiskbroom scanning; (B) pushbroom scanning; (C) spectral scanning; (D) snapshot imager. Adapted from 10.1016/j.ifset.2013.04.014.	19
2.2	(a) Illustration of whiskbroom scanning method, with the scan area part way across full track width. With this design, the linear sensor array images each pixel on the ground sequentially, scanning across the full track width before the platform moves forwards one pixel. (b) Illustration of pushbroom scanning method. While each ground spatial pixel imaged on the ground is maintained at the same size, the 2D detector array enables imaging of the entire cross track width simultaneously. . .	20
2.3	Pushbroom design using dichromatic filters. These integrated filter sensors enable extremely compact designs, requiring only imaging optics in front of the sensor.	21
2.4	Snapshot imager comparison, adapted from [55]. Figure (a) is an example of a "division of focal plane" design, where filters are placed directly onto the detector pixels at the focal plane, resembling a Bayer style pattern. Figure (b) shows an example "division of aperture" design, where macro sized colour filters are used in conjunction with a micro lens array, in a configuration similar to a plenoptic camera. Depending on the design, imaging optics may be placed in front of the spectral filters.	24
2.5	The three main types of integral field unit (IFU). These systems use (a) lenslet coupling, (b) lenslet-fibre coupling, or (c) image slicing mirrors. .	26
2.6	Liquid water absorption spectrum [64]	27
2.7	Example OPTRAM Model, adapted from [70]	29
2.8	MARMIT model diagram adapted from [72]. Wet soil is modeled as dry soil covered in a thin liquid layer. T_w is the transmittance through the water, R_D the reflectance of dry soil, r_{xy} and t_{xy} are the Fresnel reflection and transmission coefficients at the water/air boundaries. n_w is the wavelength dependant refractive index of water.	32

3.1	Classic symmetrical all spherical Offner Relay	39
3.2	Seidel third order aberrations	40
3.3	(a) Optical Diagram of the FYMOS spectrograph, (b) render of mechanical design inset	42
3.4	Comparison of 4 optimization cases. (a) is an all-spherical design, which is, in essence, an Offner relay with a spherical grating. (b) is similar to (a) but with a tilted spherical grating. (c) is an Offner-Chrisp design the primary and Tertiary mirrors have different radii of curvature. (d) is the design use for FYMOS, which is similar to (b) but with a X0Y1 X2Y1 term polynomial added to the spherical grating. The grating lines are along the Y axis.	43
3.5	Bar chart showing the average wavefront RMS figure in the spatial and spectral fields (grey bars), with a breakdown of the first 11 standard Zernike terms, plus the higher orders (magenta). The Zernike terms add up in RMS to produce the average wavefront RMS.	45
3.6	(a) Spot size RMS in the field. The square is of size 10 x 10 microns for comparison. (b), the distortion (Smile and Keystone) is computed to be respectively less than 10 microns and 1 micron (c) surface Sag at the best fit sphere (40mm) showing the amplitude of the freeform correction needed. The colorbar is in microns. (d) diffraction efficiency computed with the NIST pySCATMECH, computed for the S polarization in blue, the P polarization in Orange, and an unpolarized incident beam (green dashed line).	46
3.7	Modeled optical throughput of the system, compared against experimental measurements. The model is based on manufacturer's data for the lens transmission, quantum efficiency of the InGaAs sensor, the diffraction grating efficiency modelled with scalar diffraction theory, and the tungsten filament lamp irradiance at 2796 K. The errors were calculated using the manufacturer's stated uncertainties.	48

3.8	Grating diffraction efficiency for first and second order	52
3.9	Optical layout of dual channel camera system	53
3.10	Rendering of the dual camera instrument	54
3.11	(a) 3D printed casing in PLA, (b) Prototype single piece carbon fibre case	55
4.1	Example of the non-uniform lighting conditions caused by intermittent cloud cover. Two images recorded 6 seconds apart, using a DJI Mavic Mini.	58
4.2	Geometry used for calculating the instantaneous field of view (IFOV) of a single pixel in a focal plane array.	59
4.3	Calculating area observed on ground at an operating altitude of 30 m above ground level (AGL) using a 25 mm focal length lens and a 15 μm pixel size.	60
4.4	Calculating reflected energy from the ground collected by the lens using solid angles.	61
4.5	Schematic overview of the fibre calibration system. The output end of the fibre is positioned at the top edge of the slit, minimising occlusion of the slit.	63
4.6	Rendering of fibre system, showing (a) a wide angle view of the system, (b), a close up of the fibre/needle assembly, and (c), a close up of the needle and mounting plate.	64
4.7	(a) Raw camera image at 1100 nm as cloud passes overhead,(b) Correc- ted for decrease in downwelling irradiance using cosine corrector chan- nel,(c) Raw spectral signal measured under clear and overcast skies ,(d) Corrected reflectance calculated using integrated calibration channel, (e) RGB image of scene taken from a Pixel 4a. See Visualisations for demonstration https://sites.google.com/view/hyperspec-imager/fibre-calibration- system	68

4.8	(a) Uncorrected reflectance measurement of uniform dry soil as cloud passes by. Note the measured reflectance values for the left of the image vary significantly from the right. (b) Reflectance measurements corrected for changing illumination using FODIS. With this setup, each pixel covers a square of side 0.4 mm	69
4.9	Residuals in measured reflectance after correction. Calculated by comparing measurements of the same sample taken under cloudy and blue sky conditions.	70
4.10	Normalised incident light intensity as measured using the FODIS for two wavelengths as cloud passes through.	71
5.1	Illustration of data cube formation from individual sensor readings of a pushbroom hyperspectral imager.	74
5.2	Example of the Python GUI used to control the camera and motor assembly on the ground. The GUI provides a live view of the sensor readout, enabling exposure controls and focus to be set quickly.	75
5.3	Example screenshot of the Python data analysis GUI, used to quickly check data quality in the field	77
5.4	(a) Ratio map of a local soil, wetted in the shape of the Durham University Shield, with the central cross and exterior (red end of the colour bar) being saturated. Regions of interest (ROI) for wet and dry soil used in the histogram are shown, marked in green and white respectively (b) Histogram of per pixel ratio values within the marked ROIs	78
5.5	(a) Surface plot of the difference between reflectance ratios calculated for wet and dry soil (metric 1) (b) Standard deviation of per pixel reflectance ratio calculated for wet soil sample (metric 2) (c) Overall ranking surface, with darker blue colours best suited for differentiating wet and dry soil. The ratio picked for this analysis is marked with a white cross, chosen after atmospheric absorption bands were discarded (shown as greyed out).	79

5.6	Flow chart describing the hyperspectral image analysis method (HIAM)	81
5.7	Ranking surface plots for (a) Weber contrast ratio and (b) Michelson contrast ratio	82
5.8	Wavelengths comprising existing indices WISOIL and NSMI, along with the index proposed in this work, imposed on atmospheric transmission spectrum computed using LOWTRAN. [105]	83
5.9	(a) Soil ratios from two sets of samples plotted against a mean calibration curve. These samples were measured under controlled illumination. The predicted and measured SMC_g values agree within a 3% error. (b) Soil samples measured under solar illumination, plotted against the same calibration curve.	84
5.10	Calibration curves created for datasets provided by [107].	85
5.11	Predicted vs measured soil moisture content from calibration curves created in Figure 5.10.	87
5.12	Plotting the mean reflectance spectrum of loose soil from Spen Farm in Leeds at a range of moisture levels. The lines marked with "+"s are the measured reflectance, while the solid lines are the calculated best fit using the MARMIT model. Measurements carried out under controlled illumination in a lab.	90
5.13	Calibration curve linking the mean water thickness estimated by the MARMIT model with the gravimetrically measured soil moisture content of the test samples. The best fit curve is plotted as a sigmoid function.	91
5.14	Estimated vs gravimetric soil moisture contents calculated for two test samples taken from another part of the field.	91

5.15	(a) Reflectance map of mixed wet and dry soil sample taken at 1440 nm.(b) Map of mean water depth (in micron), calculated excluding 1400 nm atmospheric absorption band. (c) Image of damp soil taken with a Pixel 4a. The petri dish has a diameter of 90 mm. (d) Mean water depth value calculated from MARMIT model decreasing monotonically with time. This was calculated as a mean of 100 spatial pixels in a 10x10 pixel square.	92
5.16	(a) Two lines with the same φ value, which don't overlap at any point. (b) Two lines with very different φ values, which do overlap and remain close in the 1200-1300 nm region. Both plots used a flat line at $y=1$ as a starting point.	93
6.1	Picture of FYMOS system attached to UAV in early testing.	98
6.2	Example capture of QGroundControl, software used to generate flight paths	99
6.3	Flowchart detailing the processing pipeline for converting raw images taken with a UAV to geo-rectified images	100
6.4	Generalised 2D Homographic transformation diagram placeholder	101
6.5	Example of an OpenCV perspective transform. Figure (a) shows an image of a poster taken at an angle with a smartphone. Figure (b) shows the transformed image to show the poster "square on".	103
6.6	Geometry for calculating the coordinates of the vertices of the slit projection onto the ground in the x direction. The same geometry is used in the y direction, substituting roll for pitch.	104
6.7	Calculating rotation around a point	104
6.8	Figure demonstrating the change in shape of the entrance slit projection based on angle. (a) and (c) Illustrate the geometry and resultant slit projection for the slit positioned normal to the surface, while (b) and (d) show the same for an angled slit.	105

6.9	Geometry for calculating the scaling factor needed to account for the angle between the normal of the cosine corrector and the Sun.	107
7.1	(a) Freshly picked leaf, (b) leaf after 90 minutes of drying, (c) histogram of ratios in a 100x100 pixel AOI in the centre of the leaf. The colour map represents the ratio of reflectance at 1564/1524 nm. The scales on the side indicates pixel numbers. For scale, the diameter of the plate under the leaf is 100 mm	111
7.2	(a) Surface plot of 2 wavelength ratios between fresh and dry leaf, with brighter colours showing a larger difference between the leaves, (b) surface plot of standard deviation of wavelength ratios of the fresh leaf, with darker colours meaning a lower standard deviation, (c) overall ranking surface, with darker colours indicating the wavelength pairings best suited to differentiating fresh and dry leaves.	112
7.3	(a) Image of leaf, with areas of interest labeled, (b) Mean Ratio of leaf plotted against mass loss, (c) Comparing change in reflectance between leaf vein and lamina, (d) Comparing reflectance gradients of the lamina at the centre of the leaf and near the edge.	112

List of Tables

2.1	Examples of modern soil moisture indices [65, 66]	28
2.2	Table comparing soil moisture reflectance measurements	36
3.1	Table comparing sensor technologies for hyperspectral imaging cameras	49
3.2	Table comparing camera models used in this project	51
5.1	Contrast ratios considered in this analysis	79

Nomenclature

AOTF acousto-optic tunable filter

CCD charge coupled device

CMOS complementary metal oxide semiconductor

NIR near infrared

SWIR short wave infrared

COTS consumer off-the-shelf

PA precision agriculture

IoT Internet of Things

AI artificial intelligence

UAV unmanned aerial vehicle

UAS unmanned aerial system

IFU integral field unit

FYMOs Freeform based hYperspectral imager for MOisture Sensing

NDVI normalised difference vegetation index

UPRFC ultra precise raster fly cutting

SPDT single point diamond turning

InGaAs indium gallium arsenide

InP indium phosphide

MCT mercury cadmium telluride

FODIS fibre optic downwelling irradiance sensor

HIAM hyperspectral image analysis method

GUI graphical user interface

IMU inertial measurement unit

Glossary

Ground spatial distance The distance between the centres of two adjacent spatial pixels as would be measured on the ground.

Hyperspectral Relating to instruments or data sets that provide continuous spectral coverage with high spectral resolution within a set wavelength range. Typically features hundreds of spectral bands.

Imaging Spectrometer Another name for a hyperspectral imager, commonly used by NASA.

Internet of Things A system of interconnected devices including computers, machinery and sensor networks, able to communicate autonomously.

LOWTRAN Low resolution computer model for simulating atmospheric transmission and background radiance, developed by the US Air Force in the 1970s.

MARMIT Multilayer radiative transfer model of soil reflectance, a radiative transfer based full spectrum model for predicting soil moisture content from reflectance data.

Multispectral Relating to instruments or data that provide information in several (often 4-6) individual spectral bands.

Near Infra-Red Infrared light spectrum that sits close to visible wavelengths, typically defined as 700-1000 nm.

Precision Agriculture Agricultural practices involving the use of sensors and precision interventions to more accurately apply the correct amounts of water, fertiliser, pesticides etc.

Pushbroom Aquisition technique where images are captured one single row of spatial pixels at a time. Flatbed scanners are a common every day example.

Radiative Transfer Model A physically based model simulating the transmission of light through materials and across material boundaries. .

Short Wave Infra-Red A region of the infra-red spectrum that at wavelengths longer than NIR, typically defined as 1000-2500 nm.

Spectral Index A comparison of the measured intensity of 2 or more spectral bands, usually a ratio or normalised difference.

Unmanned Aerial System Total system including the vehicle, instrumentation, and the command and control station.

Introduction

1.1 Remote Sensing and Hyperspectral Imaging

Remote sensing can be defined as the process of acquiring information about a subject without making physical contact. The process involves measuring the emitted or reflected electromagnetic and sound radiation from a target. Remote sensing has become an integral part of our everyday lives, from the satellite photography used in popular mapping applications to the radar systems involved in air traffic control and meteorological forecasting.

1.1.1 Early Remote Sensing

The history of remote sensing began with the invention of photography. Soon after the first permanent images were recorded in the early 19th century, photographers such as Nadar began to produce airborne photography using hot air balloons. [1] With the rapid development of photographic technology, by the turn of the 20th century cameras had become compact enough to be regularly flown on kites. It was also around this time that the first "unmanned" aerial photography started taking off, with the German apothecary and photographer Julius Neubronner demonstrating the first pigeon mounted cameras in 1908. [2] Example photographs of both a camera pigeon and an airborne picture are shown in Figure 1.1. These pigeon

photographers saw limited work through both world wars, with the newly invented aeroplanes producing the bulk of aerial photography by the end of World War 1.

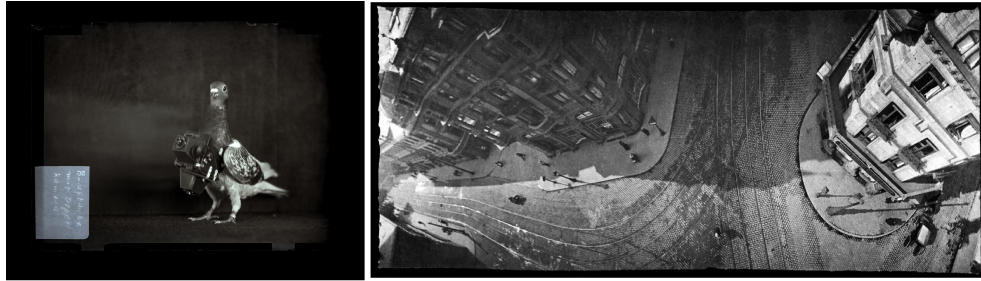


Figure 1.1: Early "unmanned" aerial photography, using camera equipped carrier pigeons. From <https://publicdomainreview.org/collection/dr-julius-neubronner-s-miniature-pigeon-camera>

Technology development during WW1 was not limited to developing more compact and lighter weight cameras. Shortly before WW2, Kodak released the 3 colour Kodachrome film, enabling the practical use of colour photography. During the war, Kodak went on to release Kodacolor Aero-Reversal-Film (later Aerochrome), combining an infrared sensitive layer with visible colour film for the first time. [3] This film was used heavily in aerial photography for its ability to distinguish camouflage from vegetation, due to the higher infrared reflectance of live vegetation. This provided an early example of the powerful utility of multispectral imaging. An example photograph taken with Aerochrome film is shown in Figure 1.2.

The modern era of satellite remote sensing began with the launch of Sputnik 1 in 1957, igniting the "Space Race". By the late sixties, an increasing number of civilian meteorology satellites were being launched, providing a platform for the first civilian Earth observation program in 1972. [4] These Landsat satellites became the first civilian satellites equipped with multi spectral imagers. Landsats 1 through 5 carried the Multispectral Scanner (MSS), operating in 4 x 100 nm bands, covering green and red visible wavelengths, and two near infrared (NIR) bands. [5] The ground resolution of the scanner was re-sampled to 60 meters.

While the data from these early Landsat satellites proved to be sufficient in early land use and inventory experiments, the 100 nm spectral resolution was found



Figure 1.2: Example photograph taken using Aerochrome film. The film maps infrared, red and green light to a red, green and blue respectively as a false colour image. Note the red colour of vegetation due to its high infrared reflectance. Photo courtesy of Rob Walwyn: <https://www.robwalwyn.com/aerochrome>

to be too low for other applications. Later Landsat satellites would carry the Thematic Mapper (TM) instruments, providing up to 11 spectral bands with the currently operational Landsat 8. [6] Multispectral imagers still form the basis of the largest Earth observation programs, with the Sentinel-2 satellites also focusing on multispectral instruments. [7]

1.1.2 Hyperspectral Imagers

The development of analytical spectroscopy techniques in relation to remote sensing was a driving force in the increasing number of spectral bands, with the enhanced spectral resolution being used to better identify mineral and crop types. [8] The next step in this path was the development of the imaging spectrometer. Where multispectral imagers record images in a number of pre-selected, non-contiguous bands, hyperspectral imagers record images in 100 or more contiguous spectral bands. This enables laboratory like reflectance spectra to be recorded for each pixel

in an image, providing large amounts of spectral information for data processing.

The first imaging spectrometer for Earth observation was the Airborne Imaging Spectrometer (AIS), first flown in 1982. [9] Initially built to test infrared area array detectors, AIS featured a 32x32 element area array. This provided a spectral coverage from 1.2 to 2.4 μm , with a spectral bandwidth of 9.3 nm, achieved using a 4 position diffraction grating to record 128 bands using the 32 spectral pixels on the detector.

While AIS successfully demonstrated the usefulness of hyperspectral data in Earth observation, its use as an engineering test bed with experimental detectors made it unsuitable for regular, long duration scientific use. [10] As a result, the Airborne Visible/Infrared Imaging Spectrometer (AVIRIS) was proposed and developed, with the purpose of providing well calibrated and stable instrument for the Earth science community. [11]

As 2D area array IR detectors were still a highly experimental technology in 1983, AVIRIS was designed around the use of linear array detectors. With many fewer detector elements than area detectors, the use of linear detectors reduced difficulties in manufacturing, calibration, and data readout. This led to the AVIRIS design using scanning foreoptics to capture cross track data in a whisk-broom mode. An explanation of whisk-broom, and other common acquisition modes, is given in Chapter 2.

The light from the scanning foreoptics was fed by optical fibres into 4 spectrometers, giving AVIRIS a spectral coverage of 0.4-2.5 μm , with an average spectral bandwidth of 10 nm. AVIRIS was designed to be flown on multiple aircraft platforms, including both the Twin Otter and the ER-2, providing a large range in working altitudes. When operating onboard an ER-2 at 20 km altitude, AVIRIS covered a ground swath of 11 km with a 17 m ground sampling distance. At this altitude, the aircraft is flying above 99% of the Earth's atmosphere, providing similar viewing conditions to satellite observations. This made the data collected by AVIRIS valu-

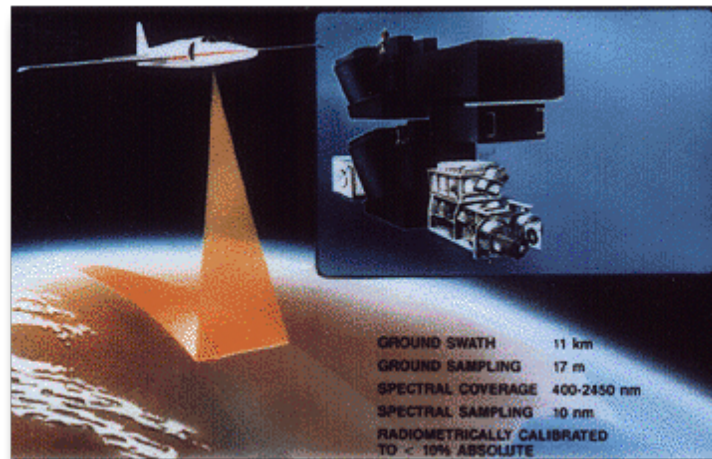


Figure 1.3: AVIRIS "Advertising" image, courtesy NASA/JPL-Caltech.

able for prototyping data processing pipelines to be used by later satellite based hyperspectral imagers. Due to the high standard of calibration, along with regular hardware updates, and a range of external factors, AVIRIS has had a long lifetime, still being flown for science missions as of 2021. An example image of AVIRIS is shown in Figure 1.3.

Following AVIRIS, there would be a long time period before the next generation facility level hyperspectral imagers would be in use. The large data volumes created by hyperspectral imagery limited the widespread access of high quality datasets, resulting in a low level of familiarity and advocacy for hyperspectral instruments. After the Challenger shuttle disaster, the planned Shuttle Imaging Spectrometer Experiment (SISEX) was cancelled, and the High Resolution Imaging Spectrometer (HIRIS) was removed from the Earth Observing System (EOS) plans, while the unplanned re-entry of the Lewis Spacecraft Mission destroyed the hyperspectral imager onboard. [12, 13] It would not be until Hyperion launched onboard the EO-1 satellite in late 2000 that a hyperspectral imager would enter and remain in Earth orbit. [14]

At present, agency level hyperspectral imagers remain fairly uncommon, both in airborne and satellite contexts. AVIRIS (Now called AVIRIS Classic) has now

been supplemented by AVIRIS-NG, using an Offner Relay pushbroom design offering a spectral resolution increase to 5 nm sampling. [15] For satellites, the highest profile current mission is the PRecursores IperSpettrale della Missione Applicativa (PRISMA) technology demonstrator operated by the Italian Space Agency. [16] Satellite hyperspectral instruments do look to have a strong future however, with both ESA and NASA having plans to launch more EO satellites, including Copernicus Hyperspectral Imaging Mission for the Environment (CHIME) and Hyperspectral Infrared Imager (HypIRI). [17, 18]

1.1.3 Commercial Market

While publicly funded hyperspectral imagers were slow to take off, private sector companies began producing the first commercial hyperspectral imagers in the late 1980's. [12] Designed to be flown on small airplanes, and marketed towards both the research community and commercial mineral mapping. One particularly successful design was the Compact Airborne Spectrographic Imager (CASI) by the ITRES Corporation. Using 2D silicon detectors, CASI covered the VIS-NIR range up to 900 nm in over 200 spectral bands. [19]

Development of this style of hyperspectral imager continued, resulting in increasing spatial and spectral resolution, with several now established brands starting up. As InGaAs and MCT sensors developed and became more affordable, imaging spectrometers with extended spectral ranges were made practically available to the consumer market. This was aided by advancements in computing hardware and software development, enabling the large hyperspectral datasets to be processed more quickly.

The next revolution came in the late 2000s, when multi rotor unmanned aerial vehicles (UAVs) became commercially available. While small UAVs had been used by research groups before this, most of these UAVs were of fixed wing type, often with 2m wingspans and requiring catapults for launching. The expertise and

equipment required to operate these drones limited their use to specialist groups. Multirotor UAVs combined the in flight stability of fixed wing aircraft, with the compact size and vertical take-off and landing capabilities of earlier helicopter style rotary airframes, while being easier to pilot than either.

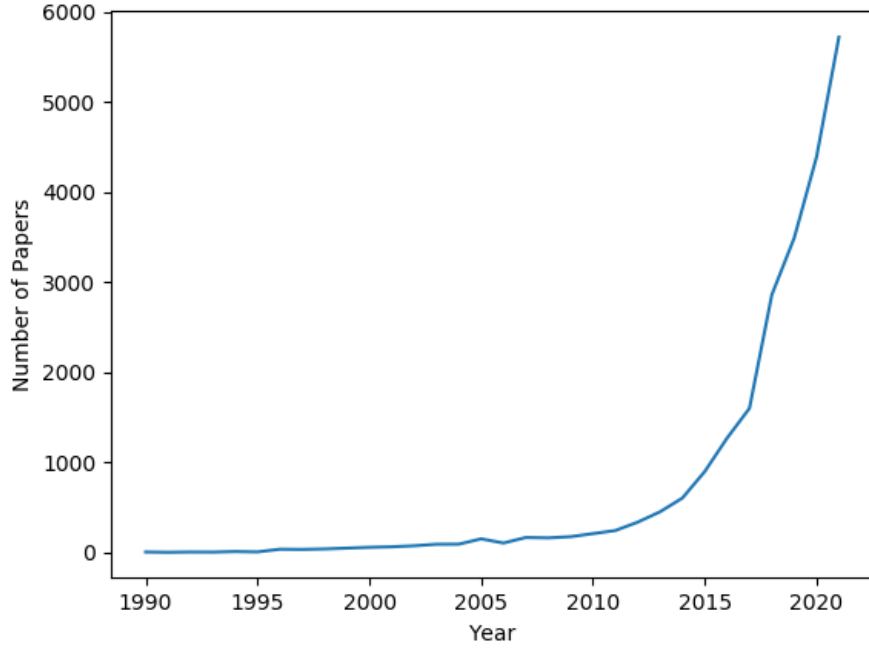


Figure 1.4: Trend showing the number of research papers per year containing the keywords "UAV" and "Hyperspectral" since 1990, as collated from Google Scholar

With the reducing cost and rising lift capacity of new UAV models, combined with the improving compactness of hyperspectral imagers, airborne hyperspectral imagery became increasingly available to the wider research community. While flights for high level facility instruments like AVIRIS are planned many months in advance, the reduced logistics of small drone flights enables much greater flexibility in both flight locations and pre-planning lead time. This has resulted in a boom in research in the area, evidenced by the keyword trend shown in Figure 1.4.

1.1.4 Modern Instrumentation

The surge in use of drone instrumentation, both in research and commercially, has driven a diverse market for off the shelf hyperspectral imagers from a variety of companies. Established companies like ITRES have developed compact UAV sized versions of their full sized instruments (e.g. MicroCASI), while many newer companies such as Headwall and HySpex have emerged.

Across many companies, the design concept of the imaging optics has converged, with most using all reflective concentric optical systems. See Section 3.2 for more detail on why these designs are so widely used. Most instruments are offered with a choice of silicon or InGaAs detectors, covering spectral ranges of 400-1000 nm and 900-1700 nm respectively, with some manufacturers offering MCT detectors to extend spectral range further into the short wave infrared (SWIR). The masses for these dispersive instruments range between 1 and 4 kg depending on detector types, suitable for the professional UAVs available from drone manufacturers, such as the DJI Matrice 600.

With recent innovations in miniaturised fabrication and sensor technologies, electronics manufacturers like IMEC have started producing hyperspectral sensors, with the spectral filtering built directly onto the detectors at a silicon level. The development of these extremely compact systems enables the use of hyperspectral imaging in more fields of remote sensing, including under water applications.

The main downsides of consumer off-the-shelf (COTS) hyperspectral imagers are the high costs, and the software and hardware lock-ins than can exist within manufacturer ecosystems. This has left room for research groups to continue developing hyperspectral instrumentation, focusing either on reduced cost to improve availability of instruments, or novel designs and manufacturing techniques to further optimise high end instruments towards specific applications.

1.2 Hyperspectral Remote Sensing in Precision Agriculture

1.2.1 Environmental Impacts of Agriculture

Agriculture has changed significantly over the last century, with increasing mechanization resulting in farm and field sizes growing immensely. While enlarged farms benefit from advantages of economies of scale, the larger field sizes raise the challenges of crop management, especially with respect to irrigation, fertiliser and pesticide use. [20] Without detailed information on crop conditions, farmers often over apply interventions such as fertilisers to ensure sufficient levels of plant nutrition throughout a field. [21] This has resulted in nearly a 700% global increase in the use of fertiliser over the last 40 years. The surplus of fertiliser is often washed away during heavy rainfall, running off the fields into local water ways. [22] This has led to major impacts on water quality even in the UK, resulting in blooms of harmful algae, fish deaths, and dead zones of limited biodiversity in UK coastal areas. [23, 24]

A similar pattern is seen with the use of artificial irrigation, which has seen a 70% increase in area coverage globally over the same timescale. The use of irrigation in some UK regions like Kent has been linked to soil erosion hot-spots in those areas. [25] Furthermore, irrigated UK farmlands tend to be concentrated, with the majority of irrigated farmlands situated in water catchments that are already overdrawn. [26] This is compounded by the fact that irrigation is often used as a supplement to rainfall, with the greatest demand coinciding with the driest periods.

While irrigation only accounts for 1% water usage in England, globally agriculture accounts for 70% of all fresh water usage. [22] By the early 2000s, the 17% of the world's farmland that was irrigated accounted for nearly 40% of the global crop output, with staple foods such as wheat and rice benefiting the most. [27]

Although irrigation provides the greatest benefit to arid regions, it also represents a large danger to farmland in these areas. When water evaporates from the soil, salts are deposited in the upper soil layers, resulting in soil salinisation. As irrigation increases the water supply to the soil, the rate of salinisation increases. Most crops are not tolerant to saline conditions, resulting in reduced yields, and even abandonment of farmland. In total, close to 10 million hectares of farmland are destroyed by salinisation each year world wide. [28]

With world population projections expecting to reach almost 10 billion by 2050, and with growth centred on developing countries, the pressure to increase world wide food production will continue to mount. Climate change is also expected to add to the difficulty of achieving sufficient food production, with serious examples even happening in the UK. In 2020, UK wheat yields dropped by 40% compared to the previous year, caused by both heavy rainfall and droughts happening during inopportune times during the growing season. This is an indicator of the sort of effect unpredictable climate patterns can have on future harvests. Satellite imagery from MODIS clearly shows the drought conditions experienced during the UK heatwave in August 2022, illustrated in Figure 1.5.

Due to these pressures, the area of land used for arable farming, and specifically irrigation supported land, has been increasing steadily. [29] As irrigated farmland offers such high efficiency for food production, this trend is expected to continue into the following decades. In order to ensure the sustainability of this practice, both in terms of water and soil conservation, improved management methods will need to be introduced.

1.2.2 Precision Agriculture

Precision agriculture (PA) is the umbrella term for the management methods aiming to help improve the sustainability of the agricultural sector. The idea of precision agriculture is to bring the technologies and concepts of the Internet of



Figure 1.5: Terra/MODIS image of the UK on 10th August 2022 during heatwave, courtesy of NASA Worldview. Worldview is part of the NASA Earth Observing System Data and Information System (EOSDIS) (<https://worldview.earthdata.nasa.gov/>)

Things (IoT) and Big Data analysis to agriculture, enabling advanced monitoring of plant and soil health, providing farmers with better decision support tools. These tools can be used by farmers to either aid decisions on manual interventions, or set up fully automated systems based on artificial intelligence (AI) models. [30, 31]

In order for PA to be effective, the monitoring system needs to collect relevant data that is resolved to a suitable spatial and temporal resolution. Due to variations in topology, underlying geology, or boundary conditions, individual fields can have local biases that can cause low spatial resolution measurements to be unrepresentative of conditions over the whole field. Sampling at too high a resolution, however, requires more expensive sensor networks, larger data storage solutions and longer processing times, without additional benefit. Although a plant by plant based management system would be the ideal end point for precision agriculture, such a set up is not practical in the real world. More realistically, a field can be split up into management zones, within each the field can be considered homogeneous.

Often, the limit on the size of these management zones depends on the irrigation, spraying or harvesting equipment used to manage the field. [20]

While implementations of precision agriculture can cover a wide range of activities including weed control, fertilisation and harvesting, this thesis will focus mostly on soil moisture management and irrigation. Soil moisture measurement is one of the keystones of precision agriculture. Practical studies have shown that variable rate irrigation can result in significant water savings, over 25% at some sites. [32] Aside from precision irrigation, measurement of soil moisture variability can also help to provide better understanding of (i) soil water retention capacity and erosion [33] (ii) drought forecasting and monitoring [34] (iii) as well as crop yield estimation and evapotranspiration rates. [35, 36] Correct deficit irrigation of crops may increase or maintain yields with a reduced volume of water consumption. [37] With regards to climate change, soil moisture content may also have a significant effect on both land carbon uptake and surface air temperatures. [38, 39]

1.2.3 Soil Moisture Measurement Methods

As precision agriculture has developed, and wide ranging variety of techniques for measuring soil moisture content have evolved. The most direct and accurate method of measuring soil moisture is through gravimetric measurements. Soil samples are collected, sealed and weighed. The samples are then gently oven dried, before being weighed again. The change in mass can then be used to calculate the percentage water content of the original sample. While this method is extremely accurate, it is extremely time consuming, requiring significant human involvement, making it difficult to implement and not financially sustainable in a competitive commercial environment.

In situ soil probes have developed into being one of the most commonly used form of soil sensors. The permittivity and resistivity of soil are sensitively dependant on soil moisture, enabling detection using either capacitance or resistance based

sensors. [40] The simplicity of the sensors, combined with volumes of scale, has resulted in them being commercially available for very low cost. These sensors are even available for home use, with sensors available to suit low cost single board computers like the Raspberry Pi.

These low cost sensors are also suited to creating larger sensor networks in the commercial market. [41] One of the greatest advantages of these sensors have is the ability to measure soil humidity at different depths, allowing for moisture content at the root level to be determined. However, in situ sensors do have practical drawbacks. As each sensor only records the soil moisture at a single point in space, requiring large numbers of sensors to gain spatial resolution. These large networks can be time consuming and labour intensive to set up. These sensors require power or communications wiring, often leaving some trailing cable on the soil surface. The trailing wires would be damaged by vehicles driving in the field, requiring the removal and subsequent replanting of the sensors each time this occurs. An example of industrial sensors from Spen Farm is shown in Figure 1.6.

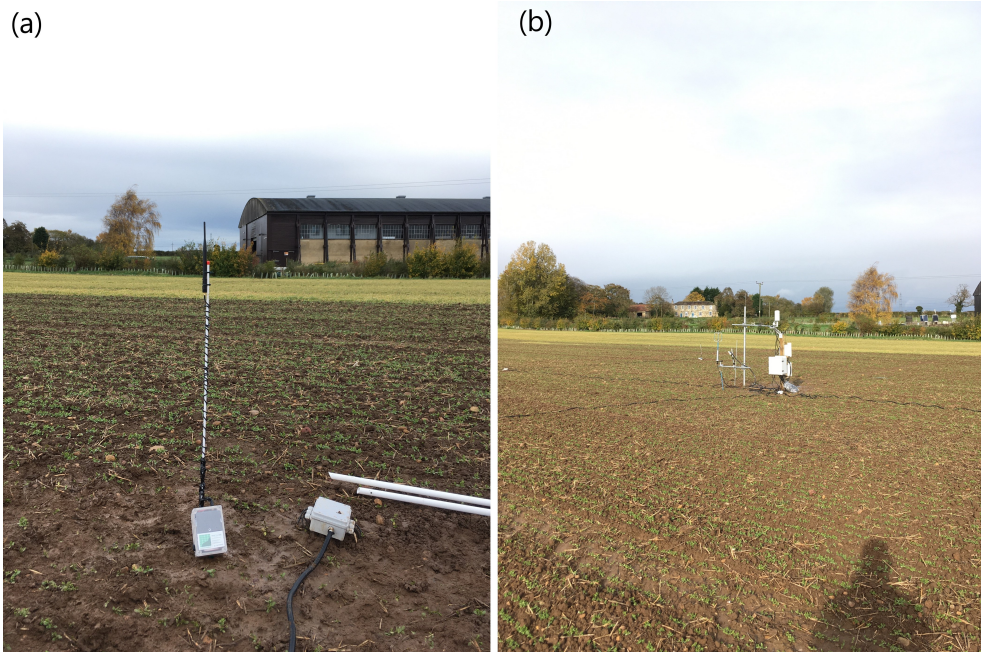


Figure 1.6: Example soil sensors at Spen Farm. (a) Shows an unplanted soil sensor, (b) shows the main hub, with cables running outwards towards planted soil sensors. Photo Credit: Murilo Vianna

Due to these limitations of in situ sensors, the remote sensing community has seen a range of developments aiming at remote measurement of soil moisture content. These techniques span from microwave radar measurements, through to thermal infrared and optical measurements, discussed in descending wavelength order below.

Radar systems have long been used for soil moisture analysis. [42] Radar return from terrain is strongly dependent on the dielectric properties of the terrain, making the radar backscatter sensitive to moisture content. Early experiments involved stationary crane mounted radar systems, with the technology developing towards the satellite based synthetic aperture radars used today. These systems, operated by NASA in the form of Soil Moisture Active Passive (SMAP) and ESA with the Soil Moisture and Ocean Salinity (SMOS) satellites, are still in operation today. [43, 44] These microwave radar based systems have some advantages over other systems. Due to their longer operating wavelengths, these instruments have the ability to observe through cloud cover. They also cover very large swath widths, with both SMAP and SMOS covering a swath of 1000 km. This enables these satellites to rapidly cover large areas of land, with SMAP making global moisture maps every 2 to 3 days. The trade-off of the high swath width is a relatively low spatial resolution. While SMAP was designed to have a ground spatial distance of 9 km, an electrical failure in its active radar system limits its resolution to 36 km, similar to SMOS's 35 km. [45] This resolution is suited to measuring regional variations of moisture content, but is much too coarse to be useful for precision agriculture.

In order to improve the spatial resolution of soil moisture measurements, shorter wavelengths in the thermal infrared, and the SWIR and NIR ranges have been investigated. [46] While development of thermal infrared techniques has been more focused on upscaling lower resolution surveys, Vis/NIR/SWIR multi- and hyper-spectral imagers have seen significant usage in soil monitoring. [47] Further details on the working principles of these instruments and how they are used to measure soil moisture content are given in Chapter 2. Spectral soil sensing techniques have

some unique advantages over other measurement methods. The broad spectral coverage of hyperspectral imagers enables a high level of versatility to be extracted from datasets. This means that along with soil moisture, hyperspectral data can be used to track other soil and plant health factors, along with weed tracking. Hyperspectral imagers have also been in deployment in various forms for almost 40 years, providing a long back catalogue of data which can be used to extract long term trends.

Hyperspectral imaging methods do have some drawbacks. Although airborne and satellite hyperspectral imagery has been available for decades, the high expense and complex logistics, along with the moderate spatial and temporal resolution, has limited its use in commercial settings. While developments in compact and reduced cost instruments and UAVs have seen expanded deployment, high costs and complex workflow procedures have still limited their use to larger farms and research groups. [48] More development in automated data processing pipelines and simplified user interfaces is needed before these instruments can be deployed without expert personnel. Compared to microwaves, the short wavelength infrared light used by these instruments has little penetrating power, and is strongly affected by both vegetation coverage and cloud cover. This prevents the use of hyperspectral imagery for soil moisture measurement during certain crop cycles and weather conditions.

Aside from the electromagnetic spectrum, some novel techniques use other "messengers" to remotely sense soil moisture. One example is the COsmic-ray Soil Moisture Observing System (COSMOS), which measures neutron densities generated by cosmic rays interacting with air and soil. [49] The rate of production of fast neutrons, and the strength of the material's moderation, both depend on the atomic mass number of the material. As hydrogen nuclei are the strongest moderating nuclei, water content of a material strongly affects its fast neutron stopping power, and thus allowing detection of moisture content. These sensors effectively calculate the average soil moisture within a circular detection area, typically with a diameter of

approximately 670 m. [50] This area averaging is an advantage over sparsely placed capacitance probes, as point measurements can be affected by the strong heterogeneity of soil moisture content. This enables a single COSMOS sensor to provide a representative average soil moisture over a large area, at the expense of spatial resolution.

Each of these methods for measuring soil moisture content have their own strengths and trade-offs. As a result, no one method will be perfect for all working conditions. Going forwards, the most robust sensor networks will be a fusion of complementary sensor types.

1.3 Thesis Outline

The work presented in this thesis towards developing a compact, pushbroom hyperspectral imager followed several parallel paths, presented in this order:

- Chapter 2 provides the technical background to understand the many differing types of hyperspectral imagers, along with their associated benefits and trade-offs. The theory behind 3 common methods of soil moisture retrieval from soil reflectance data is presented.
- Chapter 3 presents the optical and mechanical design of the FYMOS hyperspectral imager, the instrument used throughout this work.
- Chapter 4 describes the fibre optic downwelling irradiance calibration channel integrated into the FYMOS design, enabling the use of the instrument under changeable cloud cover.
- Chapter 5 introduces the data collection and processing methods used for transforming raw sensor readings into corrected reflectance datacubes ready for use. Methods for extracting soil moisture content from this data are also demonstrated.

- Chapter 6 discusses the changes in hardware and data processing required to use the hyperspectral imager onboard a UAV platform.
- Chapter 7 discusses some of the other agricultural uses of hyperspectral data, demonstrating its use in measuring moisture content in plant leaves.
- Finally Chapter 8 presents the conclusions of this thesis.

Supplementary material, including animations and videos relating to figures in this thesis, can be found at <https://sites.google.com/view/hyperspec-imager/thesis-animations>.

Technical Background and Theory

The aim of this chapter is to provide the reader with an understanding of the range of technologies available in the hyperspectral imaging world, and how they may be used to remotely measure moisture content. The chapter is split into two sections, with the first covering a range of the most common hyperspectral imaging system designs, while the second describes methods used to derive moisture content from reflectance data.

2.1 Fundamentals of hyperspectral imagery

Hyperspectral imaging is a field which is experiencing rapid development. Advancements in optical design, sensor technologies and computing power combine to enable large inter-generational developments in spatial, spectral and temporal resolutions, along with improvements to stability and signal to noise ratio. The wide ranging applications of hyperspectral imagery, from medical imaging to food quality inspection and from art conservation to airborne remote sensing, have resulted in a diverse range of hyperspectral imaging cameras. These can be split into 3 main groups depending on their acquisition modes: spatial scanners, spectral scanners, and snapshot imagers. The main differentiator between these groups is how each sensor reading corresponds to the final completed data set, often called a data cube. These cubes are usually three dimensional, having two spatial dimen-

sions and one spectral dimension. A summary diagram showing an example sensor reading from each type is shown in Figure 2.1.

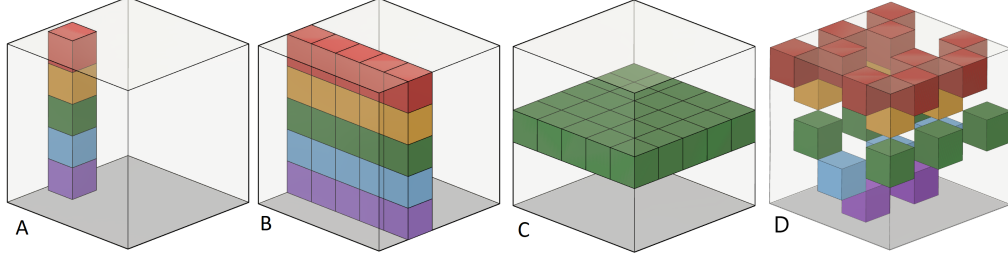


Figure 2.1: The main hyperspectral acquisition methods: (A) whiskbroom scanning; (B) pushbroom scanning; (C) spectral scanning; (D) snapshot imager. Adapted from 10.1016/j.ifset.2013.04.014.

2.1.1 Spatial Scanners

Spatial scanners use dispersing optics to split incident light into a continuous spectrum, which is then imaged onto a camera sensor. The key difference to a spectral scanner is that all wavelengths in the spectral range of the camera sensor are imaged simultaneously. Depending on the type of sensor used, these instruments can be split into 2 groups, whiskbroom and pushbroom.

Instruments using one dimensional detector arrays operate in the whiskbroom acquisition mode. Using a single row of pixels, the detector records a contiguous spectrum that corresponds to an area on the target of interest. This single sensor reading corresponds to a single spatial pixel in the final datacube. Scanning mirrors can be used to record a series of spectra across the desired track width, before the scanner is moved forward to record another line of spatial pixels, illustrated in figure 2.2(a). This type of hyperspectral imager was common in the early days of imaging spectrometry, as the smaller number of detector elements made manufacturing and calibration easier when electronic detectors were an immature technology. The disadvantage is that the design exchanges sensor/electronics complexity for mechanical complexity, requiring the use of tightly controlled, fast moving scanning mirrors to capture across track data. Errors in control of these mirrors will cause

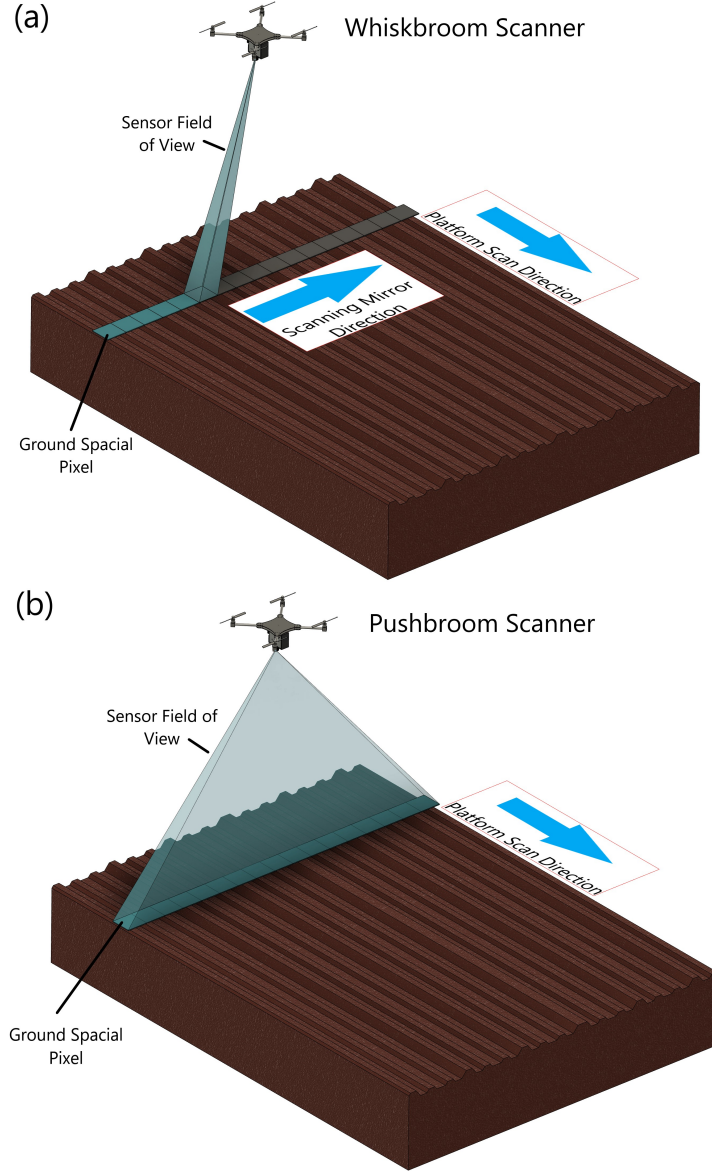


Figure 2.2: (a) Illustration of whiskbroom scanning method, with the scan area part way across full track width. With this design, the linear sensor array images each pixel on the ground sequentially, scanning across the full track width before the platform moves forwards one pixel. (b) Illustration of pushbroom scanning method. While each ground spatial pixel imaged on the ground is maintained at the same size, the 2D detector array enables imaging of the entire cross track width simultaneously.

image "jitter", which results in warped or incomplete images that can be difficult to correct with post processing.

Pushbroom instruments, on the other hand, use two dimensional detector arrays to capture spectral data along the entire cross track width simultaneously without moving parts, as shown in Figure 2.2(b). In the final image, this corresponds to an entire row of spatial pixels being recorded at once. This reduces the size and complexity required of the instrument fore-optics, enabling the development of compact systems suitable for use on UAVs. Pushbroom instruments can be categorised into two groups, based on their use of dispersive or dichroic optics.

Compact hyperspectral imagers for the NIR/SWIR range mostly use diffraction gratings as the primary dispersing component. Reflective gratings are most commonly used for the high end instruments due to their greater efficiency and wider operating wavelength range. Transmissive diffraction gratings are still used in a variety of instruments, with the reduced cost and lower alignment sensitivity compared to reflective gratings making them ideal for use in low cost 3D printed prototypes. [51]

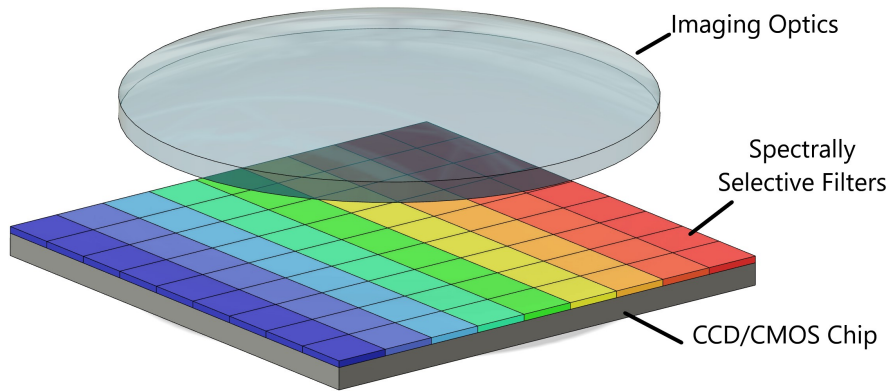


Figure 2.3: Pushbroom design using dichromatic filters. These integrated filter sensors enable extremely compact designs, requiring only imaging optics in front of the sensor.

Other systems use dichromatic filters to create very compact pushbroom instruments. Linear strips of interferometric Fabry-Perrot filters are placed onto the

detector at the wafer level, integrated into the CMOS pixels, to create hyperspectral sensors, as shown in Figure 2.3. [52] This greatly simplifies the optics required in front of the sensor, enabling this style of instrument to be extremely small and lightweight. As the filters are chosen during manufacturing, setting the spectral bandwidth and resolution of each channel, this style of hyperspectral imager lacks some of the adaptability of dispersive optical systems with adjustable slit widths.

2.1.2 Spectral Scanners

Spectral scanning hyperspectral imagers also use two dimensional detector arrays, with both dimensions recording spatial information. Instead of using dispersive optics, tunable filters such as an acousto-optic tunable filter (AOTF) or an adjustable Fabry-Perot etalon are used to sequentially sweep through a selected wavelength range. As each wavelength is imaged with independent camera exposures, different exposure times can be used for different wavelengths, which can be useful if a subject exhibits vastly different reflectance across its measured spectrum. AOTFs in particular can be compact, light weight, and can have extended wavelength coverage, resulting in their widespread use. Their main downside is their relatively low (30%) overall transmission and complex transmission curve. [53, 54]

As a sequential scanner can only record a set number of bands per second, recording a full spectrum datacube can be a relatively lengthy process. The Senop HSC-2 hyperspectral imager can scan its 1000 spectral bands at a maximum rate of 149 bands per second, requiring around 7 seconds to build a complete datacube, limiting full range measurements to static imaging. However, not all applications require the full spectral range of a hyperspectral imager, reducing the required scan time. In addition, the 2D spatial information recorded by each frame enables the use of orthomosaic stitching techniques for geo-registration of sets of datacubes.

2.1.3 Snapshot Imagers

Snapshot hyperspectral imagers record all spectral bands and 2D spatial information simultaneously in a single exposure. This gives snapshot imagers the advantage of having the highest temporal resolution of any hyperspectral imager design, with some models achieving video frame rates of up to 8 Hz. Snapshot instruments can be divided into two classes, depending on whether they use lossy filter designs, or more complex throughput division optics. [55]

The most compact snapshot imager designs for UAVs are based on the use of filter arrays. These can be split into division of aperture, or division of focal plane types, depending on the position of the filter array. Both styles are illustrated in Figure 2.4. Division of aperture systems made up some of the first snapshot systems, being a natural evolution from similar multispectral designs. These designs consist of an array of band-pass filters, with each filter focused onto a portion of the camera detector by a small lens, illustrated in Figure 2.4(b). [56] Simpler designs function similarly to an array of individual colour cameras, while others use designs similar to traditional light field/plenoptic cameras to extract limited depth information. [57]

Alternative placements for the filter array have also been developed. Division of focal plane array style imagers use filters placed directly onto the detector during manufacture, similar to the method described for the pushbroom instruments. [58] Instead of placing filters in linear rows, the filters are placed in mosaic patterns, analogous to the Bayer pattern in an RGB camera, shown in Figure 2.4(a). This creates very lightweight imaging systems, requiring only an objective lens for light collection and imaging. The technology was pioneered by Imec, and can be applied to both visible silicon sensors, and SWIR InGaAs detectors.

While these filter style systems offer significant advantages in size and weight compared to scanning systems, these come with some trade-offs. As the sensor is being used to encode both 3D data (2 spatial dimensions and 1 spectral dimension) onto a 2D surface, both spatial and spectral resolution are reduced in comparison to

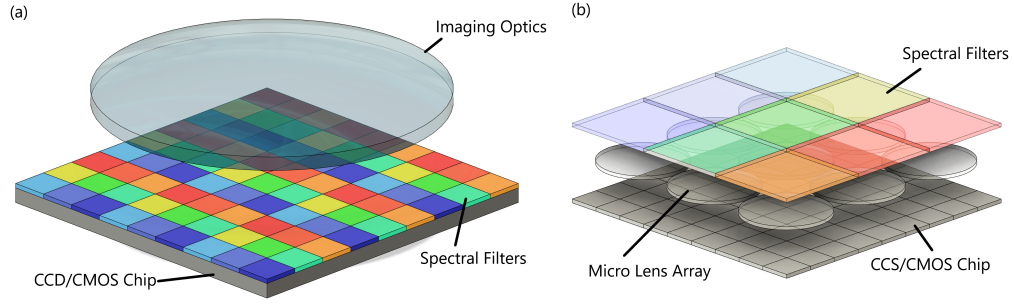


Figure 2.4: Snapshot imager comparison, adapted from [55]. Figure (a) is an example of a "division of focal plane" design, where filters are placed directly onto the detector pixels at the focal plane, resembling a Bayer style pattern. Figure (b) shows an example "division of aperture" design, where macro sized colour filters are used in conjunction with a micro lens array, in a configuration similar to a plenoptic camera. Depending on the design, imaging optics may be placed in front of the spectral filters.

other types of hyperspectral imager.

Filter based systems also fail to make full use of the additional light collection available to snapshot systems. To capture a scene made up of, for example, 100 spatial rows, a push broom instrument would need to capture 100 individual exposures. A snapshot imager capable of imaging the entire scene could use approximately 100 times the exposure time of the scanning system and maintain the same time resolution. However, narrow band filters reject all but the central transmission band of light they're designed for, reducing the throughput of the system by $1/N$ for a system with N spectral bands. This results in a majority of the incident light being rejected by the system. For the IMEC sensors, the full width half max bandwidth of each filter varies from 10-15 nm depending on the exact model.

In order to improve upon these lossy systems, many differing optical designs have been developed that can make full use of the incoming light. [55] One of the most commonly used designs is the integral field unit (IFU) spectrograph. IFUs work by dividing the focal plane into a set of sub apertures, either individual pixels or small slits, depending on the type of IFU. Each one of these sub apertures is then fed into a spectrograph, enabling the spectrum from each pixel to be recorded simultaneously. There are three main methods of dividing the focal plane, using

pure lenslet arrays, lenslets coupled into a fibre array, or image slicing mirrors. [59, 60, 61] A diagram visually explaining these different IFU types is shown in Figure 2.5. Each design comes with its own benefits and drawbacks. Lenslet IFUs can have simple, lightweight optics, but are inefficient in their use of detector pixels. Fibre IFUs leave much less unused area on the sensor, but can be susceptible to transmission losses and cross talk. Image slicer based IFUs provide higher spatial resolution than fibre systems, as the sampling pitch along each sub slit is effectively the pixel pitch of the sensor. However, image slicers are complex shapes, with a high number of facets that must be precisely machined. To manufacture these parts, ultra precise machining methods like ultra precise raster fly cutting (UPRFC) and single point diamond turning (SPDT) are commonly used. [62, 63] These production methods produce surfaces suitable for use in infrared optics directly after machining, but the resulting surface roughness limits their use in the visible/UV range without further precision polishing. Overall IFUs can achieve high optical throughputs along with high spectral resolution.

The main disadvantages of IFUs are their complex optics, and their requirement for large format detector arrays. The optics required to split the focal plane can be both large and relatively heavy, making incorporating these designs into small UAV compatible instruments challenging. Image slicer based systems may offer a compact solution, but the challenges in machining the large number of facets makes this technology expensive. The large format detectors have increased size, weight, power and cooling requirements compared to the more common smaller detectors used in current instruments, further increasing the difficulty of miniaturising these systems. While IFUs have been in use for earth observation on satellite platforms, to the author's knowledge there are no IFU based snapshot imagers currently in use onboard small commercial UAVs.

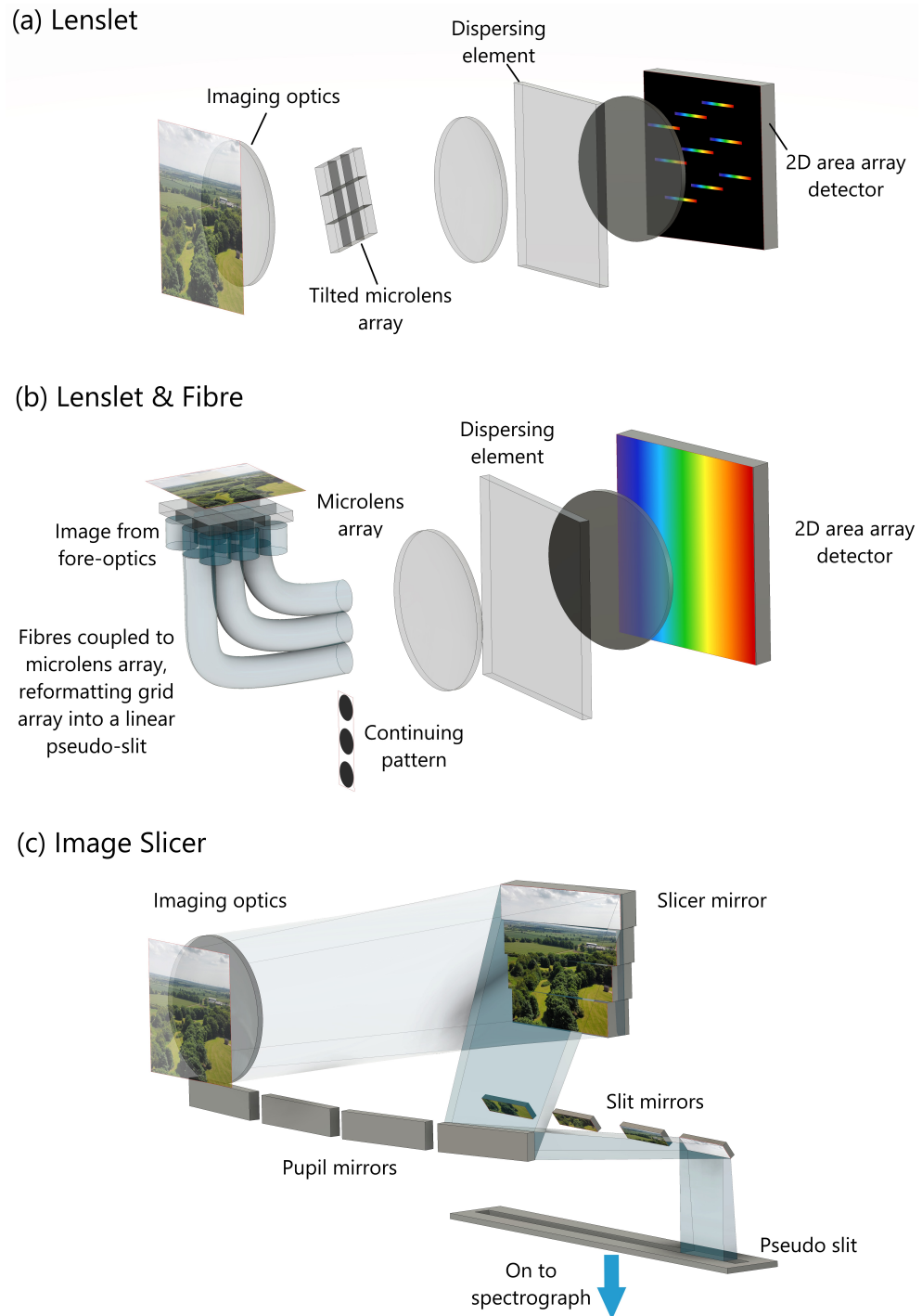


Figure 2.5: The three main types of integral field unit (IFU). These systems use (a) lenslet coupling, (b) lenslet-fibre coupling, or (c) image slicing mirrors.

2.2 Remote Soil Moisture Measurement

Given the importance of measuring soil moisture content to multiple industries, numerous experiments and methods have been developed to measure soil moisture content through remote spectroscopic measurements. These methods generally fall into two camps, either using spectral index measurements or more general spectral shape fitting methods

2.2.1 Spectral Indices

Spectral index methods are based on the absorption spectrum of water, the main features of which stem from the three fundamental vibrations of water molecules, O-H bending, symmetric O-H stretching and asymmetric O-H stretching. The combinations of various overtones of these fundamental vibrations result in the complex water absorption spectrum.

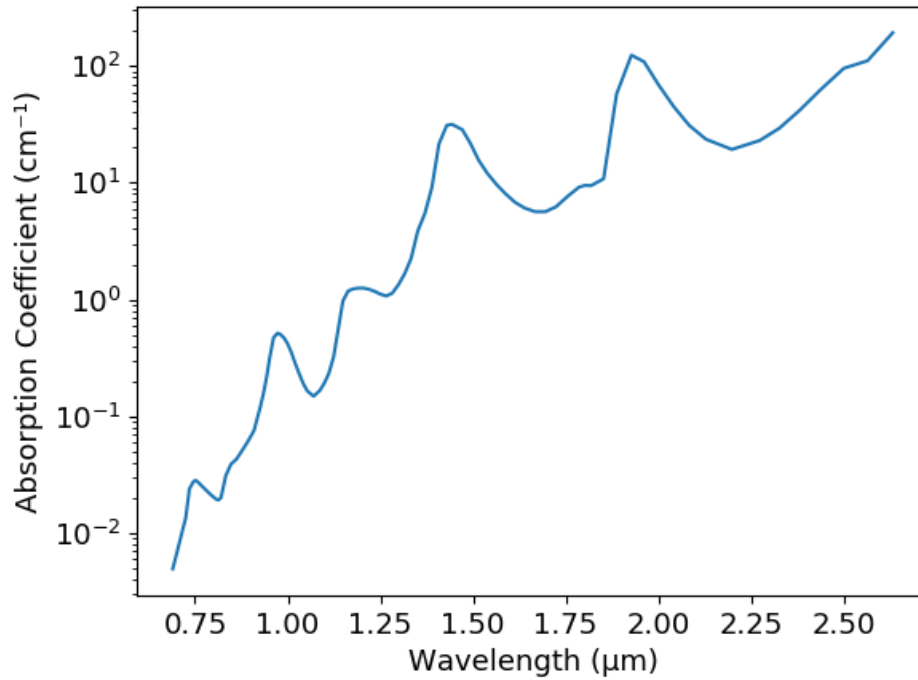


Figure 2.6: Liquid water absorption spectrum [64]

Index	Spectral Bands	Formula
NSMI	1.8 μm ; 2.119 μm	$\frac{R_{1.8}-R_{2.119}}{R_{1.8}+R_{2.119}}$
WISOIL	1.3 μm ; 1.45 μm	$\frac{R_{1.45}}{R_{1.30}}$
NINSOL	2.076 μm ; 2.23 μm	$\frac{R_{2.076}-R_{2.23}}{R_{2.076}+R_{2.23}}$
NINSON	2.122 μm ; 2.23 μm	$\frac{R_{2.122}-R_{2.23}}{R_{2.122}+R_{2.23}}$

Table 2.1: Examples of modern soil moisture indices [65, 66]

Table 2.1 shows examples of modern soil moisture indices focused on the shortwave infrared (SWIR) observing band. In this band, often defined at 1-2.4 μm , spectral water absorption peaks at 1.2 μm , 1.4 μm and 1.9 μm . While these bands are sensitive to moisture content under controlled lab illumination, they are also sensitive to absorption due to atmospheric water vapour. This makes indices using these wavelengths difficult to utilise without precise measurement and calibration of these atmospheric effects at the time of data recording. Water Index SOIL (WISOIL) is an example of such an index, centred on the strong 1.45 μm water absorption band. [65, 66]

Some published spectral indices, such as NINSOL and NINSON, have been developed with a focus on avoiding peak water absorption wavelengths, with the aim of increasing the usability of these indices under solar lighting conditions. [67] Using statistical correlation methods, the correlation between wavelength pairings and soil moisture content can be compared, enabling selection of optimal wavelengths for reflectance indices. Several statistical methods exist, with a more detailed discussion found in later chapters. While NINSOL and NINSON have been shown to be robust under solar conditions, they were developed using ASD Fieldspec Pro point spectrometers, using wavelengths above the 2.2 μm cut-off wavelength common to most commercially available InGaAs focal plane arrays. In order to use soil moisture spectral indices with compact hyperspectral imagers, new indices using appropriate wavelengths will have to be derived.

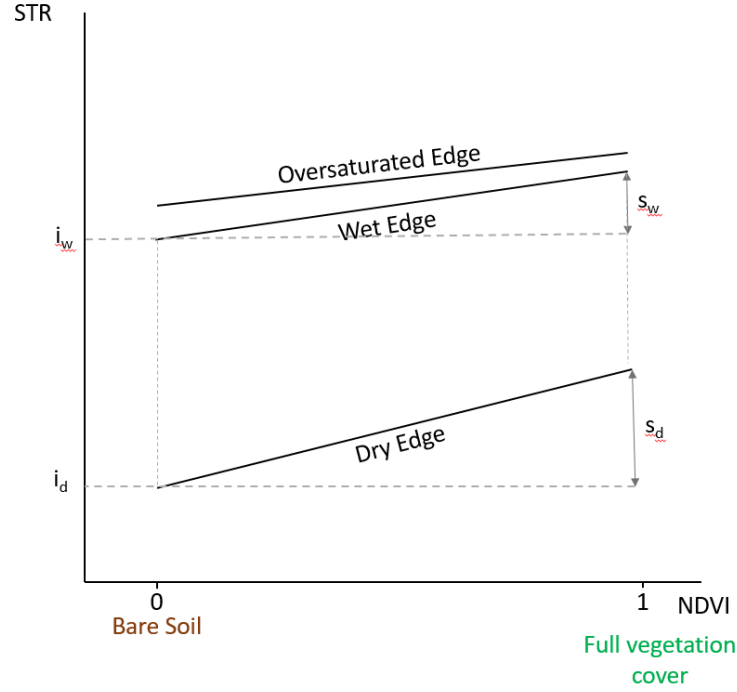


Figure 2.7: Example OPTRAM Model, adapted from [70]

2.2.2 Index Space Methods

Other groups have developed models that make use of more than one index. Models such as the LST-VI triangle and TOTRAM use the relationship between soil moisture, land surface temperature (LST) and normalised difference vegetation index (NDVI) to estimate soil moisture content. [68] The use of LST introduces difficulties in data processing, as the surface temperature is related to atmospheric properties such as air temperature, wind speed and humidity, which must be calibrated for each observation. To avoid the use of thermal infrared, the optical trapezoid model (OPTRAM) was developed. [69] The trapezoid name comes from the shape of the data bounding box, shown in Figure 2.7.

Instead of LST, a new parameter called the SWIR transformed reflectance (STR) is used:

$$STR = \frac{(1 - R_{SWIR})^2}{2R_{SWIR}} \quad (2.1)$$

where R_{SWIR} is the reflectance in a SWIR wavelength band, chosen as 1650 nm or 2210 nm to correspond with Landsat 8 bands. The normalized soil moisture content, W , is then calculated as:

$$W = \frac{\theta - \theta_d}{\theta_w - \theta_d} = \frac{STR - STR_d}{STR_w - STR_d} \quad (2.2)$$

where θ is the soil moisture content, with θ_w and θ_d being the local soil's maximum and minimum water content, with STR_w and STR_d being the corresponding STR values. These bounding STR values are calculated from the wet and dry edges of the trapezoid shown in Figure 2.7:

$$STR_w = i_w + s_w NDVI \quad (2.3)$$

$$STR_d = i_d + s_d NDVI \quad (2.4)$$

where i_w , s_w , i_d and s_d , are the intercepts and slopes of the wet and dry edges plotted in NDVI-STR space. To calculate NDVI, bands 4 and 5 of Landsat 8 were used, with band 4 covering 0.64-0.67 μm and band 5 covering 0.85-0.88 μm . NDVI values were then calculated as:

$$NDVI = \frac{\text{band 5} - \text{band 4}}{\text{band 5} + \text{band 4}} \quad (2.5)$$

Combining equations 2.2, 2.3 and 2.4, the normalised moisture content can be estimated as:

$$W = \frac{STR - i_d - s_d NDVI}{i_w - i_d + (s_w - s_d) NDVI} \quad (2.6)$$

The advantage of these methods that include NDVI is that they attempt to estimate soil moisture content for both bare and vegetated soils. This is done by assuming

that vegetation moisture content linearly relates to root zone soil moisture content. By making use of spectral bands already in use by multispectral satellites, the models can be applied to a large back catalogue of data to investigate trends over longer time scales.

The downside of these models is in their sensitivity to calibration, with the best results found when the wet and dry edges are determined manually from the graph. [69] This makes generalising the model to a wide variety of soils difficult. When calculating the edge slopes using numerical regression methods, the authors note "... its accuracy in predicting the absolute value of soil moisture needs to be viewed with caution". This difficulty in retrieving accurate soil moisture content has been shown using other instruments and locations. [70]

Still, the idea of developing spectral indices models capable of being used on both bare and fully vegetated soil is extremely important, especially for use in agriculture. During a growing season, both extremes of vegetation coverage will be seen, with accurate moisture content measurement required throughout. The extended wavelength coverage of hyperspectral imagers may enable more robust triangle/trapezoid methods to be developed.

2.2.3 Spectral Shape Fitting

As an alternative to more simple spectral indices, spectral shape fitting methods have been developed. They can take several forms, ranging from spectral envelope fitting to full radiative transfer models. The main advantage of these models is that they work outside of the strongest water absorption bands, potentially increasing their robustness under solar illumination.

In fact, the idea of using physically based radiative transfer models is not new. In 1925, Anders Ångström proposed the idea that wet surfaces can be modeled as dry surfaces covered by a thin layer of water. [71] In this model, the reduction in albedo of wet surfaces can then be attributed to internal reflections at the boundary

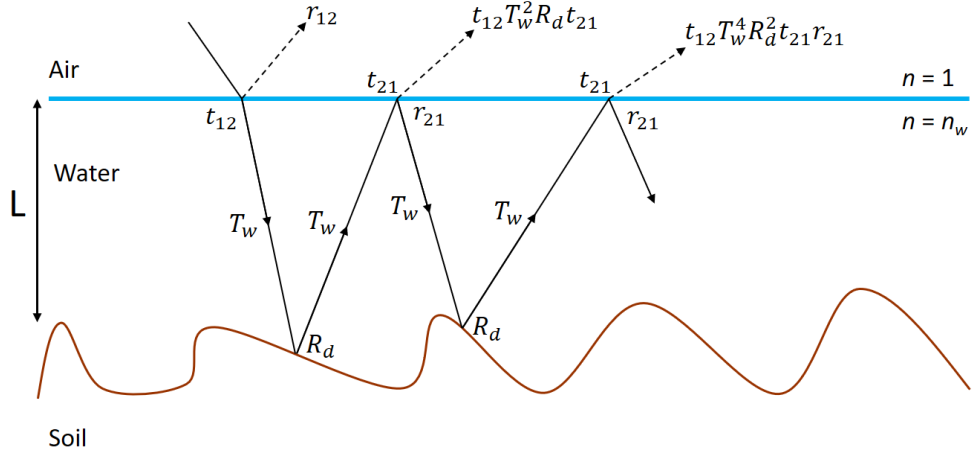


Figure 2.8: MARMIT model diagram adapted from [72]. Wet soil is modeled as dry soil covered in a thin liquid layer. T_w is the transmittance through the water, R_D the reflectance of dry soil, r_{xy} and t_{xy} are the Fresnel reflection and transmission coefficients at the water/air boundaries. n_w is the wavelength dependant refractive index of water.

between the water layer and the air based on Snell's law. Later iterations of this model by Lekner and Dorf in 1988 and Bach and Mauser in 1994 improved upon this concept by using Fresnel coefficients to calculate boundary reflections and introducing Beer's law to include light absorption in the water layer respectively. Most recently, Babelt et al further developed this model into the MARMIT model in 2020. [72] Here, the transmittance along the entire path of the light ray across multiple internal reflections is considered.

As a majority of soil radiative transfer models make use of the thin water film model, it is useful to understand the approach. A derivation of the MARMIT radiative transfer model is described here, with the accompanying diagram shown in Figure 2.8. The internal water/air boundary reflectance, r_{21} is calculated by considering diffuse reflectance integrated over a hemisphere: [73]

$$r_{12} = 1 - \frac{1}{n^2}(1 - r'_{12}) \quad (2.7)$$

where

$$r'_{12} = \frac{3n^2 + 2n + 1}{3(n+1)^2} - \frac{2n^3(n^2 + 2n - 1)}{(n^2 + 1)^2(n^2 - 1)} + \frac{n^2(n^2 + 1)}{(n^2 - 1)^2} \log n - \frac{n^2(n^2 - 1)^2}{(n^2 + 1)^3} \log \frac{n(n+1)}{n-1} \quad (2.8)$$

The transmission of light T_w through the absorbing water is given by the Beer-Lambert law $T_w = \exp(-\alpha_B L)$, where α_B is the absorption coefficient per unit length, and L is the thickness of the water layer.

As the soil surface may not be completely covered in water under low moisture content conditions, an efficiency term ε that marks the fraction of the total surface covered by water is introduced. The overall modelled reflectance is then given by:

$$R_{mod} = \varepsilon \times R_{ws} + (1 - \varepsilon) \times R_d \quad (2.9)$$

where R_{ws} and R_d are the reflectances of the wet and dry soil respectively. An ε value of 0 results from completely dry soil, while an ε value of 1 indicates "totally wetted" soil, where there is no completely dry surface soil remaining. This is distinct from saturated soil, which will have an ε at or close to 1, along with a high value of L .

As shown in Figure 2.8, R_{ws} is given by the sum of reflectances and transmissions at the air/water boundary:

$$R_{ws} = r_{12} + t_{12}T_w^2 R_d t_{21} + t_{12}T_w^4 R_d^2 t_{21} r_{21} + \dots \quad (2.10)$$

Equation 2.10 can be factorised to give:

$$R_{ws} = r_{12} + t_{12}T_w^2 R_d t_{21} (1 + T_w^2 R_d r_{21} + T_w^4 R_d^2 r_{21}^2 + \dots) \quad (2.11)$$

This is a geometric series $(a + ar + ar^2 + \dots)$, where $r = T_w^2 R_d r_{21}$, which converges to $\frac{1}{1-r}$ for $|r| < 1$.

This reduces equation 2.11 to:

$$R_{ws} = r_{12} + \frac{t_{12}t_{21}R_dT_w^2}{1 - r_{21}R_dT_w^2} \quad (2.12)$$

To recover soil moisture content, the model is then inverted as follows. The reflectance of the target wet soil is recorded, and then fitted to the spectrum of a similar dry soil sample using the two free parameters L and ε . The calculated values of L and ε are then multiplied together to produce a new variable $\varphi = L \times \varepsilon$, the mean water depth. This φ value can then be compared to a calibration curve of mean water depth against soil moisture content values to retrieve the soil moisture content.

One of the major downsides to these methods is their reliance on prior soil reflectance measurements. Soil spectral reflectance is sensitive to sampling conditions such as temperature, humidity, source-sample-instrument geometry. [74, 75, 76] The recorded spectra can also be affected by how the samples were prepared, such as if differing sieving, grinding or pulverization methods are followed. [77] This can make close fitting of spectra acquired through remote sensing to lab calibration data difficult.

In order to work around the difficulties of comparing spectra recorded in different environments over a broad spectral range, it is possible to invert and fit these radiative transfer models using only a single wavelength band. [78] When using this method, care must be taken to fully characterise the noise of the camera sensor under measurement conditions, as small fluctuations can have a significant impact on the model inversion. Additionally the complexity of the models can result in many local minima being found during the inversion process, necessitating the use of more robust and computationally expensive optimisers compared to index methods.

In practice, all of these methods can be difficult to apply with varying environmental conditions. Differing soil types, vegetation coverage, and land uses may all

suit different soil moisture recovery methods. A summary table is shown in Table 2.2. This highlights an advantage of hyperspectral imagery, as the high resolution and broad spectral coverage of hyperspectral data enables any of these methods to be applied. Further details on the use of these methods will be discussed in Chapter 5.

Method	For	Against	Use Case
Spectral Index	<ul style="list-style-type: none"> • Simple to apply • Can be less affected by sample preparation • Requires few spectral channels • Can use back catalogue of data from multispectral satellites 	<ul style="list-style-type: none"> • Can be sensitive to atmospheric water vapour • Some indices require wavelengths beyond standard 2D InGaAs sensor range • Soil dependant 	<ul style="list-style-type: none"> • Soil moisture measurement under varying weather conditions • Using back catalogue of satellite data to investigate long term trends
Index Space	<ul style="list-style-type: none"> • Aims to measure soil moisture under vegetation cover 	<ul style="list-style-type: none"> • Data processing requires manual intervention • Accuracy of current solutions can be poor 	<ul style="list-style-type: none"> • Soil moisture measurement in areas with patchy or complete vegetation coverage
Spectral Shape Fitting	<ul style="list-style-type: none"> • Often use physically based models • Use wide wavelength range, so less affected by narrow atmospheric absorption bands • May incorporate several radiative transfer models, including vegetation models 	<ul style="list-style-type: none"> • Affected by sample preparation methods • Require complex data processing techniques • Soil dependant • Requires data from modern high resolution hyperspectral imagers 	<ul style="list-style-type: none"> • Soil moisture measurement in clear sky conditions • May be used to retrieve vegetation properties

Table 2.2: Table comparing soil moisture reflectance measurements

Instrument Design

This chapter describes the design of the Freeform based hYperspectral imager for MOisture Sensing (FYMOS), the instrument which the majority of the following work is based on. This section is an expanded version of the Optics Express paper published in 2021, and supported by a UKRI- EPSRC Innovation fellowship “A compact novel hyperspectral imager for more reliable and precise agriculture”. UKRI- EPSRC Grant Reference : EP/S001727/1. [79]

3.1 Freeform Optics

FYMOS is a hyperspectral imager designed for remote sensing of soil moisture content. The key design element in the FYMOS instrument is the freeform diffraction grating, with part of this project aiming to develop the technology and methods to machine these gratings in house. Freeform optics are optics with highly non-spherical shapes, and in principle can be defined as having no rotational or translational axis of symmetry. These complex shapes open up new degrees of freedom in optical designs for correcting distortions, especially important in compact systems utilising off-axis configurations.

Commercial development of freeform optics has been ongoing for 50 over years, with the first commercial product being the Polaroid SX-70 Land camera. [80] The fold-

ing design of the camera necessitated a very tilted view finder. The use of spherical optics would have resulted in significant keystone distortion and field tilt. Instead, an aspheric mirror, freeform eye lens and freeform corrector plate were used, each of which had no rotational symmetry. While expensive and difficult to manufacture, this design demonstrated the benefit of using freeform surface to correct distortions inherently resulting from folded and compact optical configuration.

With the advancement of computer controlled design and fabrication processes, the manufacturing cost of freeform optics is no longer so prohibitive, with freeform optics becoming an increasingly important option in optical design. [81] Freeforms are now found in all fields of optics, in the most advanced optical transmission devices [82, 83], unobscured telescope designs for astronomical applications [84], free space communication using orbital angular momentum [85] and adjustable focus lenses based on Alvarez surfaces [86]. Their added value and high potential have also been demonstrated in mobile camera technologies [87].

In optical systems designed for airborne and space applications, aluminium mirrors have become the more ubiquitous choice over glass optics. Aluminium optics are lightweight, robust and easy to machine. One major advantage of aluminium optics is the ability to make both the mirrors and mirror mounts out of the same material, ensuring matching rates of thermal expansion. [88] The much higher thermal conductivity of aluminium also enables a metal optical system to return to thermal equilibrium faster than an equivalent glass system.

While conventional aluminium alloys such as 6061 have been used to produce mirrors for infrared systems, the granular crystal structure of these alloys limits the achievable surface finish. [89] The recent development of rapidly solidified aluminium alloys has provided new opportunities for metal optics. While these rapidly solidified aluminium (RSA) alloys were initially created for their increased strength, fatigue resistance and low thermal expansion, the ultrafine grain structure of these alloys also enables significant reductions in surface roughness after diamond turning. [90, 91] These alloys, combined with progress in the field of dir-

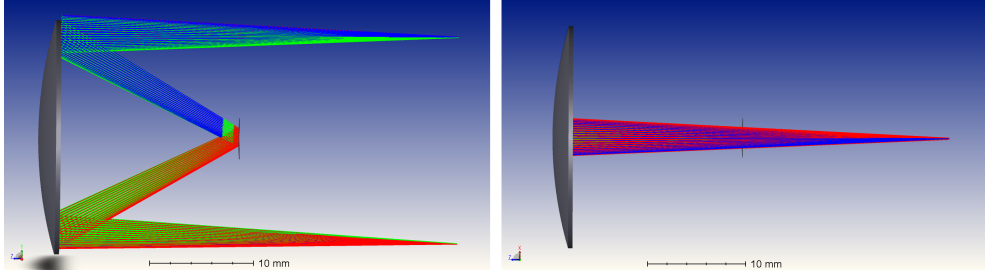


Figure 3.1: Classic symmetrical all spherical Offner Relay

ectly machined freeform surfaces, have enabled the development of cost-effective diamond machined freeform reflective diffraction gratings. These freeform gratings can be potentially used in compacting optical designs, making them promising components for space and UAV based hyperspectral imagers. Freeform gratings have so far been used in systems with low to medium spectral resolution. ($R < 200$) [92, 93]

3.2 Design Overview

One of the most common designs of spectrometer for hyperspectral imaging is the Offner type spectrograph. This design is based on the Offner unit magnification relay, which was patented by Offner in 1973. The relay comprises of three spherical mirrors with a common centre of curvature, with the object and image lying in the same plane as the centre of curvature. An example of an all spherical relay is shown in Figure 3.1.

The main advantage of the Offner relay system is the excellent third order Gauss Seidel aberration correction due to the symmetry of the design. These aberrations are shown in Figure 3.2. As the design is symmetrical about the aperture stop on the secondary mirror, the odd aberrations of distortion and coma are cancelled. The Petzval sum of the system is zero, as the primary and tertiary mirrors have double the radius and opposite sign to the secondary, resulting in zero field curvature. As the object and image are located at the centre of curvature of the mirrors, the angle

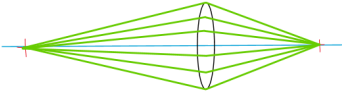

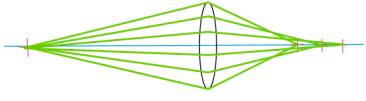
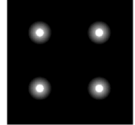
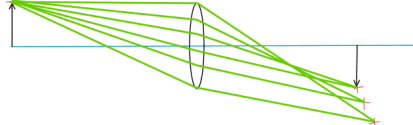
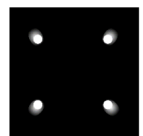
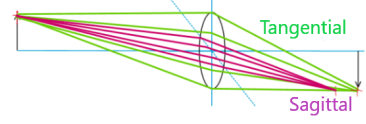
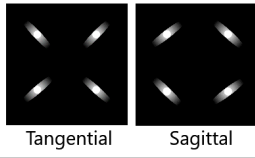
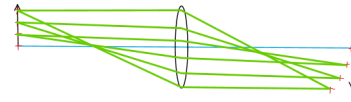
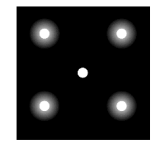
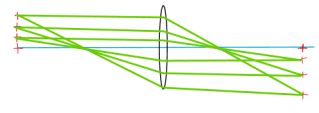
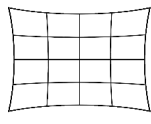
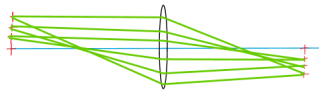
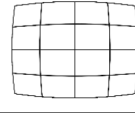
Aberration	Ray Diagram	Image
No Aberration		
Spherical Aberration		
Coma		
Astigmatism		
Field Curvature		
Positive Distortion (Pincushion)		
Negative Distortion (Barrel)		

Figure 3.2: Seidel third order aberrations

of incidence of the marginal rays onto the mirrors $i = 0$. This results in spherical aberration, defined as:

$$W_{040} = - \sum_{all\ surfaces} \frac{1}{8} \left(-(ni)^2 h \left(\frac{\alpha'}{n'} - \frac{\alpha}{n} \right) \right) \quad (3.1)$$

and coma, defined as:

$$W_{131} = - \sum_{all\ surfaces} \frac{1}{2} \left(-(ni)(nj) h \left(\frac{\alpha'}{n'} - \frac{\alpha}{n} \right) \right) \quad (3.2)$$

both being equal to 0, where $n = 1$ and $n' = -1$, α and α' are the marginal ray angle at each mirror, and h is the height of the chief ray at each mirror. As listed, these equations are for an all spherical system. [94]

Astigmatism, defined as:

$$W_{222} = - \sum_{all\ surfaces} \frac{1}{2} \left(-(nj)^2 h \left(\frac{\alpha'}{n'} - \frac{\alpha}{n} \right) \right) + \frac{(n' - n)}{4} \varepsilon \frac{h^2 k^2}{R^3} \quad (3.3)$$

is corrected in a similar manner to field curvature, where the contributions from the M1 and M3 mirror combined are equal and opposite to the contribution from the M2 mirror. Again considering an all spherical system, Equation 3.3 becomes:

$$W_{222} = -\frac{1}{2} \left(-(nj_1)^2 h_1 (2\alpha_1) \right) - \frac{1}{2} \left(-(nj_2)^2 h_2 (2\alpha_2) \right) - \frac{1}{2} \left(-(nj_3)^2 h_3 (2\alpha_3) \right) \quad (3.4)$$

With $j_1 = j_3 = -\alpha_1$, $j_2 = -2\alpha_2$, $\alpha_1 = \alpha_2$ and $h_1 = h_3 = -2h_2$, and $n = 1$ this becomes:

$$W_{222} = \frac{1}{2} \left(-\alpha_1^2 2h_2 (2\alpha_1) \right) - \frac{1}{2} \left(-4\alpha_1^2 h_2 (2\alpha_1) \right) + \frac{1}{2} \left(-\alpha_1^2 2h_2 (2\alpha_1) \right) \quad (3.5)$$

Multiplying out the brackets, this simplifies to:

$$W_{222} = -\alpha_1^2 h_2 (2\alpha_1) + 2\alpha_1^2 h_2 (2\alpha_1) - \alpha_1^2 h_2 (2\alpha_1) = 0 \quad (3.6)$$

This means the design is free from all 5 primary third order optical aberrations. In reality, as the secondary mirror obscures fields close to the optical axis, the relay must be used with off axis fields, introducing higher order astigmatism.

Soon after the introduction of the Offner relay, Thevenon suggested replacing the convex secondary mirror with a diffraction grating, creating the Offner spectrometer. Since then, Offner spectrograph designs have been studied in detail, and can be classified in three main configurations: All spherical systems, with identical M1

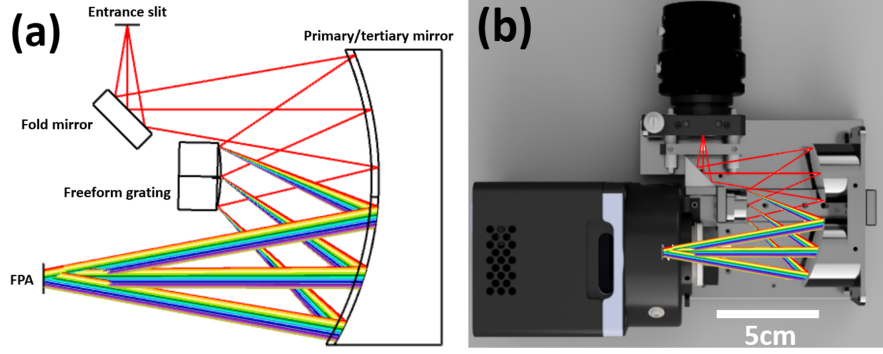


Figure 3.3: (a) Optical Diagram of the FYMOS spectrograph, (b) render of mechanical design inset

and M3 spherical mirrors concentric with the spherical grating, Spherical Offner-Chrisp designs, where the primary and tertiary mirrors have different radii of curvature but remain spherical and near concentric to the grating, and Freeform Offner-Chrisp designs, introducing freeform surfaces to the mirrors and grating.

By adding a grating to the Offner relay, the symmetry of the system is broken, leading to the introduction of optical aberrations. In the standard Offner spectrometer design, field aberrations are controlled by increasing the size of the spectrometer until the aberrations are reduced to an acceptable level. For a given slit size, increasing the spectrometer size will decrease the field angle through the spectrometer, reducing aberrations such as astigmatism. The change in geometry in the Offner-Chrisp system was developed with the idea of countering the broken symmetry caused by the diffraction grating. Correcting the resulting astigmatism by tilting the diffraction grating results in the introduction of coma into the image. By splitting the primary and tertiary mirrors and individually optimising their curvature and placement, field aberrations can be reduced without increasing the volume of the instrument.

The FYMOS design (shown in Figure 3.3) is a variant of the Offner spectrograph, with the primary and tertiary mirrors using the same spherical surface, but with the grating being optimised as a freeform. This design simplifies the manufacturing of the primary and tertiary mirrors, while enabling aberration correction through

optimisation of the grating's freeform surface. The design was driven by two constraints: (i) the grating period that can be comfortably machined by 4 axis ruling using a diamond V-shape tool (10 microns), (ii) the requirement to cover at least a 6 x 4 mm sensor area of an InGaAs sensor. The initial InGaAs sensor chosen for the instrument was a sensor from Raptor Photonics, featuring a thinned InP substrate to increase spectral sensitivity in the 700 - 1000 nm spectral range. To cover the full spectral range of the sensor within it's physical dimensions, the spectral linear dispersion at the image plane, ζ , was set at 250 nm/mm. The grating density l was set at 100 mm⁻¹ by the manufacturing constraints mentioned above. The radius of curvature R_g of the convex grating is given by: [95]

$$R_g = \frac{1}{ml\zeta}$$

and calculated to be 40 mm for diffraction order $m = 1$.

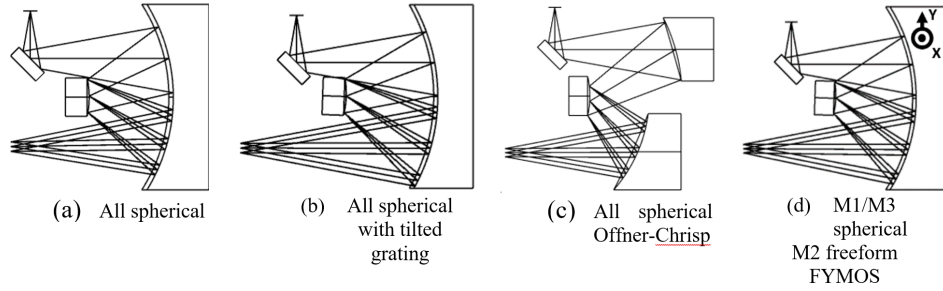


Figure 3.4: Comparison of 4 optimization cases. (a) is an all-spherical design, which is, in essence, an Offner relay with a spherical grating. (b) is similar to (a) but with a tilted spherical grating. (c) is an Offner-Chrisp design the primary and Tertiary mirrors have different radii of curvature. (d) is the design use for FYMOS, which is similar to (b) but with a X0Y1 X2Y1 term polynomial added to the spherical grating. The grating lines are along the Y axis.

The optimisation of the freeform grating was done by adding two XY polynomial terms to the base 40mm radius spherical shape. The first was X0Y1, a tilt term about the axis normal to figure 3.4. The second was X2Y1, an astigmatic term with a quadratic profile along the axis normal to the plane of figure 3.4. In Zemax, only the XY polynomial terms are available for grating optimization. The two chosen polynomials are not orthogonal, so their contributions cannot be summed

independently. The optimisation was performed using 9 spatial field points (-3, 0, 3 mm) in XY, and 3 spectral points (700, 1200, 1700 nm) at equal optimization weights, with the optimization function set to minimize RMS wavefront error. To highlight the performance gains of the FYMOS design compared to other types of Offner Spectrometers, 4 different cases were modeled, as shown in Figure 3.4.

- a). An all-spherical design, where the primary/tertiary have the same radius of curvature and are concentric with secondary (spherical grating).
- b). A similar design to item (a), but whose RMS spot sizes were optimized by tilting the grating around the x axis.
- c). An all spherical Offner-Chrisp design, with a primary and tertiary mirror with different radii of curvature but which remain concentric.
- d). A similar design to items a and b but optimized with a freeform grating.

A comparison of the performance of these designs is shown in Figure 3.5. The RMS wavefront error is averaged over the spatial and spectral fields, with the all-spherical conventional design being used as a baseline to compare the other three configurations. For this design, astigmatism is the largest contributor to wavefront error. By tilting the grating during the optimisation, a transfer in aberration from astigmatism to Trefoil is noticed, leading to an improvement of about 30% in the wavefront error. Moving to an all spherical Offner-Chrisp system offers the same level of reduction in astigmatism, but with $1/3^{\text{rd}}$ the level of Trefoil, resulting in a further 30% reduction in WFE. In comparison to the Offner-Chrisp design, the freeform FYMOS design balances a further reduction in astigmatism with a slight increase in Trefoil and spherical aberration, resulting in a threefold improvement in wavefront error over the conventional all spherical Offner spectrograph.

The theoretical RMS spot size across the full spatial and spectral fields was then assessed and is shown in Figure 3.6-a. Figure 3.6-b shows the modeled keystone and smile of the instrument, two very important imaging distortions present in

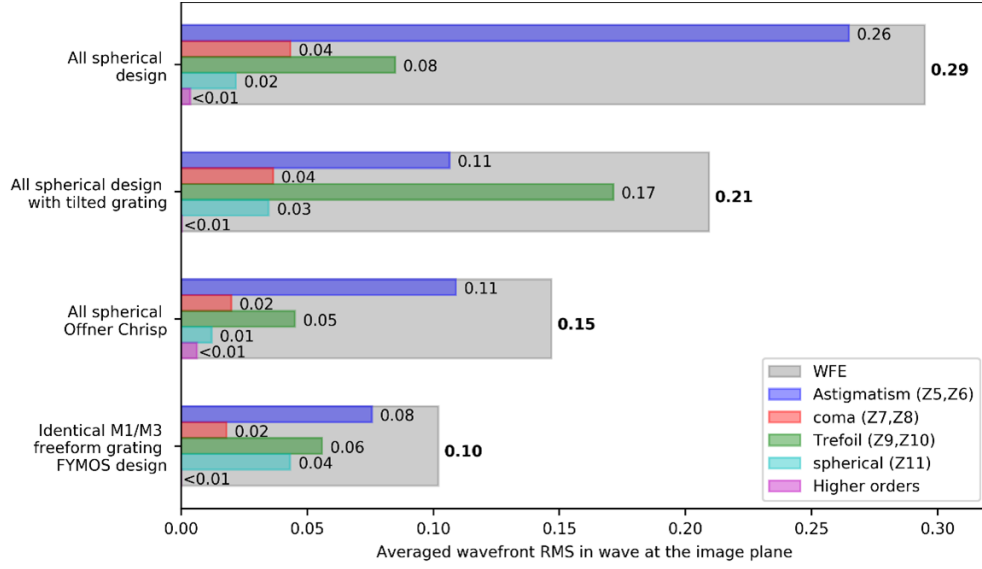


Figure 3.5: Bar chart showing the average wavefront RMS figure in the spatial and spectral fields (grey bars), with a breakdown of the first 11 standard Zernike terms, plus the higher orders (magenta). The Zernike terms add up in RMS to produce the average wavefront RMS.

imaging spectrometers. Keystone distortion results in an image which has varying magnification with wavelength, while smile results in curved lines of constant wavelength. The computed smile distortion for this design is under 10 microns, less than the 15 micron pixel pitch of the chosen detector. The mapped freeform shape with the best fit sphere removed is shown in Figure 3.6-c.

The groove profile of the grating was optimised for a blaze wavelength of 1 micron, (corresponding to a blaze angle of 2.8°), diffraction order 1, a line density of 100 lines/mm and an incidence angle of 25.5° . The grating delivers maximal optical performance in the 0.7-1.7 microns range. The diffraction efficiency, shown in Figure 4-d, was computed and optimized using NIST Rigorous Coupled Wave Analysis python package (pySCATMECH*) based on an aluminum substrate with refractive index and extinction coefficient[†] taken from McPeak et al. 2015.

*<https://pages.nist.gov/pySCATMECH/>

[†]<https://refractiveindex.info/>

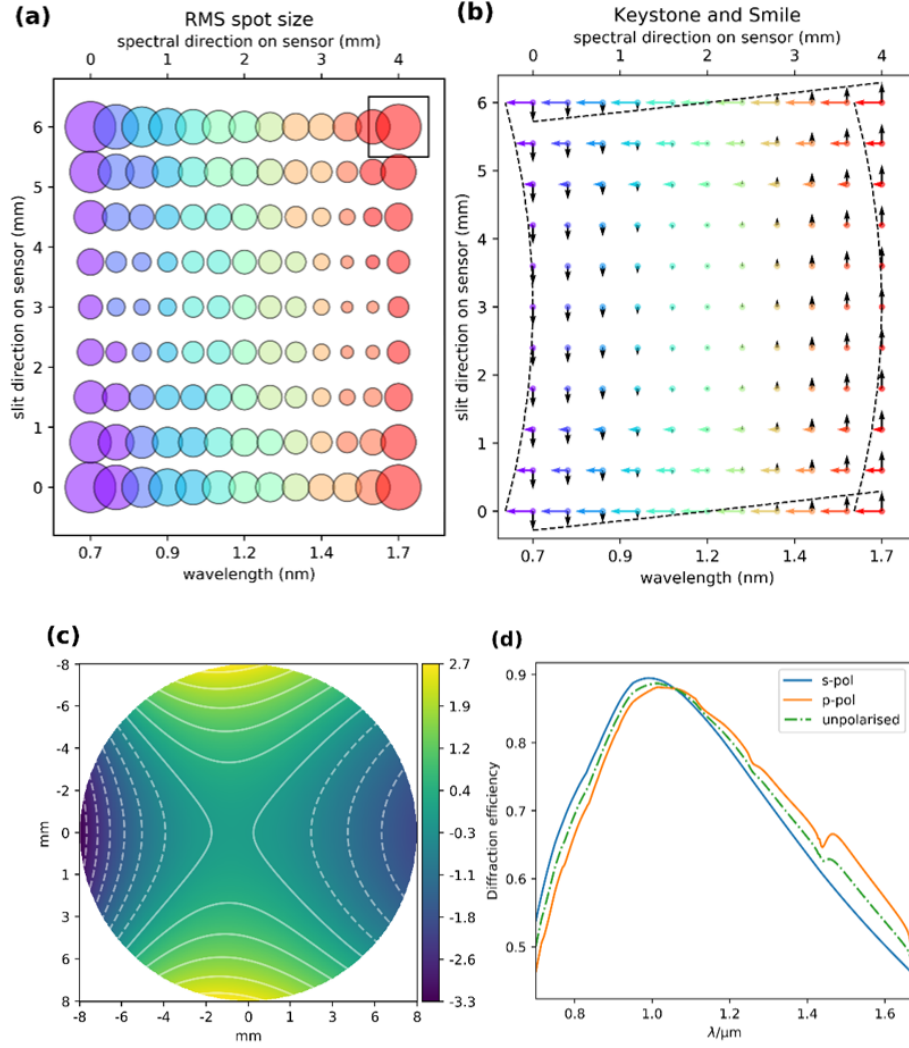


Figure 3.6: (a) Spot size RMS in the field. The square is of size 10 x 10 microns for comparison. (b), the distortion (Smile and Keystone) is computed to be respectively less than 10 microns and 1 micron (c) surface Sag at the best fit sphere (40mm) showing the amplitude of the freeform correction needed. The colorbar is in microns. (d) diffraction efficiency computed with the NIST pySCATMECH, computed for the S polarization in blue, the P polarization in Orange, and an unpolarized incident beam (green dashed line).

3.3 Spectral Calibration and Throughput Testing

The spectral calibration of the instrument was carried out using a computer-controlled Omni-lambda 300 monochromator, using a temperature regulated tungsten halogen lamp (Thorlabs SLS201/M) as the illumination source. The mono-

chromator was scanned from 1000 nm to 1700 nm, with the location of the center of the peak recorded every 20 nm. These values were used to generate a look up table of sensor pixel number to wavelength. From this, the mean dispersion per spectral pixel was found to be 4 nm. A set of infrared bandpass filters were then used to verify the calibration, with the measured peaks of the filters matching the expected wavelength value within 4nm, or 1 spectral pixel.

A simple computer model was created to calculate the effective sensitivity of the system across the usable wavelength range. This model includes (i) the wavelength dependent effects of lens transmission, (ii) the diffraction grating efficiency as shown in Figure 3.6(d), (iii) the detector quantum efficiency as per the sensor manufacturer's data-sheet and (iiii), the spectral power distribution of the tungsten halogen lamp as provided by the manufacturer. A comparison between the model and the real instrument is shown in Figure 3.7. The data for the model has been interpolated from mean manufacturer's data for each component. The error fill area for the model and the error bars on the filters were calculated by considering the errors introduced by the stated manufacturing tolerances of the lens, optical filters, lamp and sensor quantum efficiency, and propagating them through the model. The overall shape of the modelled spectrum matches well with the measured lamp spectrum, providing confidence that the system is functioning as intended.

3.4 Camera Selection

Selecting a camera system for use in UAV instrumentation involves balancing a variety of factors. Sensor type, size, resolution, read out speed, sensitivity, connection type and more are all details that must be considered. Silicon camera sensors used in standard VIS/NIR applications become transparent at 1.1 μm , and so alternative detector materials must be used. For use in the SWIR wavelength range, indium gallium arsenide (InGaAs) and mercury cadmium telluride (MCT) are the two most common detector materials. Of the two, MCT sensors provide the largest

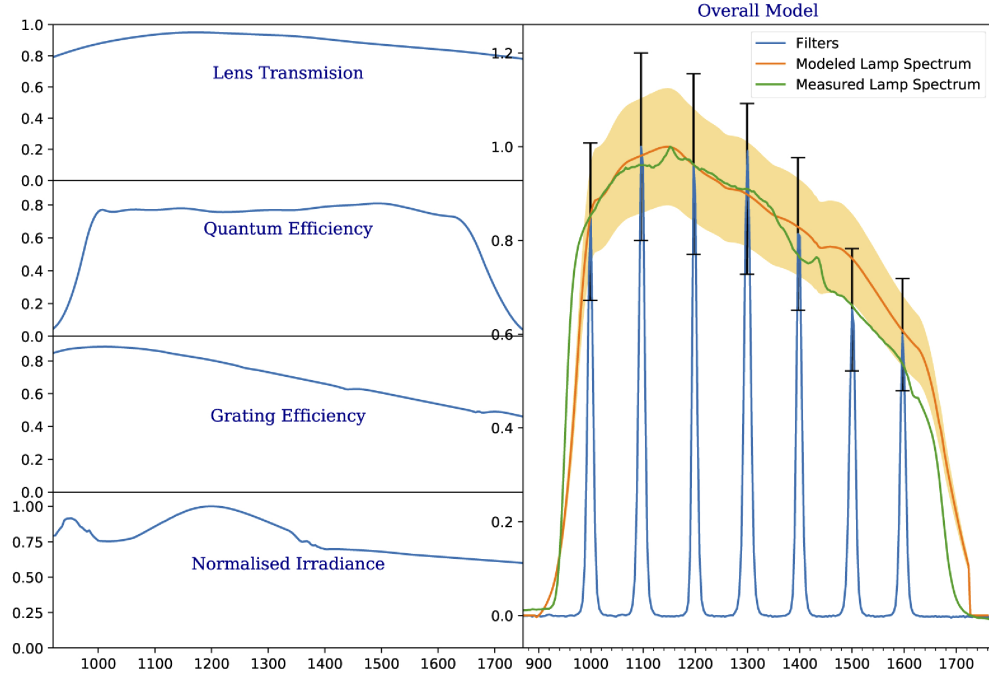


Figure 3.7: Modeled optical throughput of the system, compared against experimental measurements. The model is based on manufacturer’s data for the lens transmission, quantum efficiency of the InGaAs sensor, the diffraction grating efficiency modelled with scalar diffraction theory, and the tungsten filament lamp irradiance at 2796 K. The errors were calculated using the manufacturer’s stated uncertainties.

spectral range, able to cover 380 to 2510 nm on a single focal plane array, while most InGaAs sensors cover a spectral range of 900 to 1700 μm . This has led to MCT being the sensor of choice for large instruments such as AVIRIS-NG. [96, 15] However, MCT sensors require much lower operating temperatures, with the Teledyne CHROMA sensor in AVIRIS-NG being kept at $-40\text{ }^{\circ}\text{C}$. These lower operating temperatures require larger, heavier cooling systems, restricting the use of these sensors to larger aircraft. Cooled InGaAs detectors often have a target temperature of $20\text{ }^{\circ}\text{C}$, achievable using small thermoelectric coolers.

Initially, this system was designed for the Raptor Photonics Owl 640 Mini InGaAs, as mentioned in section 3.3. This camera has a number of selling points, with the main advantage being the special InGaAs sensor with a thinned InP substrate, which extends the lower end of the spectral range of the camera down from 900 nm to around 550 nm. This would enable SWIR moisture sensing and red-edge plant

Camera	For	Against	Use Case
Silicon	<ul style="list-style-type: none"> • Compact • Lightweight • Low pixel pitch, enabling high resolution and wide FOV 	<ul style="list-style-type: none"> • Maximum wavelength cut-off of 1000 nm 	<ul style="list-style-type: none"> • Imaging in visible wavelengths
InGaAs	<ul style="list-style-type: none"> • Operating temperature of 20 °C • Require less cooling than MCT • New back-thinned sensors extend lower wavelength cut-off towards visible • Useful for SWIR wavelengths (900-1700 nm) 	<ul style="list-style-type: none"> • Cooling systems larger and heavier than Silicon cameras • Reduced wavelength range compared to MCT 	<ul style="list-style-type: none"> • Suited for NIR/SWIR imaging onboard small UAVs
MCT	<ul style="list-style-type: none"> • High spectral range (380-2500 nm) 	<ul style="list-style-type: none"> • Require low operating temperatures • Need large, heavy, powerful coolers 	<ul style="list-style-type: none"> • Used in satellite and larger airborne platforms, such as AVIRIS-NG

Table 3.1: Table comparing sensor technologies for hyperspectral imaging cameras

imaging on a single sensor. The camera itself is very compact and lightweight, partly due to the lack of an in built thermoelectric cooler. However, this lack of cooler severely limits the signal to noise ratio of the camera, and introduces instabilities in measured intensities when used over long time periods.

The camera also uses a Camera Link connector, requiring a bulky Camera Link to USB3 capture card in order to be used with laptops or other compact computers. While this could be used on larger UAVs, the added bulk of the external capture card and its subsequent power supply made this camera impractical for use onboard a small UAV.

The final InGaAs camera chosen for the FYMOS instrument was the Photonic Science PSEL VGA. While this camera is much bulkier than the Raptor Photonics camera, the in built thermoelectric cooler provides a significantly better signal to noise ratio and thermal stability. The camera features a GigE connection, meaning no external capture cards are needed to interface with most laptops or compact PCs. The main disadvantage of this camera is the reduced spectral range, with the quantum efficiency rapidly dropping off below 1000 nm. This resulted in the dual channel VIS/SWIR design described in section 3.5. More recently Photonic Science have released an extended range InGaAs sensor, similar to the Raptor Photonics camera. In future, more manufacturers will be offering these sensors in a variety of hardware packages.

3.5 Dual Channel Variant (to be finalised)

While FYMOS was designed primarily for soil moisture sensing, one of the primary advantages of a hyperspectral imager is the versatility of the data. The SWIR wavelength range of the main InGaAs camera is ideal for investigating spectral features due to water, but for other agricultural related processes extending the spectral range into the visible could provide useful information. For example, many crop yield estimation and vegetation cover indices use comparisons between

Camera	For	Against	Use Case
Raptor Photonics	<ul style="list-style-type: none"> • Compact • Lightweight • Extended Spectral Range 	<ul style="list-style-type: none"> • Uncooled • Low signal to noise ratio under low flux • Poor thermal stability • Requires bulky external capture card, or specialised PCIe card 	<ul style="list-style-type: none"> • Imaging using wide bandpass filters
Photonic Science	<ul style="list-style-type: none"> • Cooled sensor in compact package • Uses GigE connection, wide compatibility 	<ul style="list-style-type: none"> • Larger and heavier than uncooled camera • Reduced wavelength range 	<ul style="list-style-type: none"> • Well suited to hyperspectral imaging
FLIR Blackfly	<ul style="list-style-type: none"> • High resolution sensors • Extremely compact • High sensitivity 	<ul style="list-style-type: none"> • Not sensitive to SWIR 	<ul style="list-style-type: none"> • Well suited to hyperspectral imaging

Table 3.2: Table comparing camera models used in this project

reflectance in the visible and near-infrared regions to determine plant coverage and health. [97]

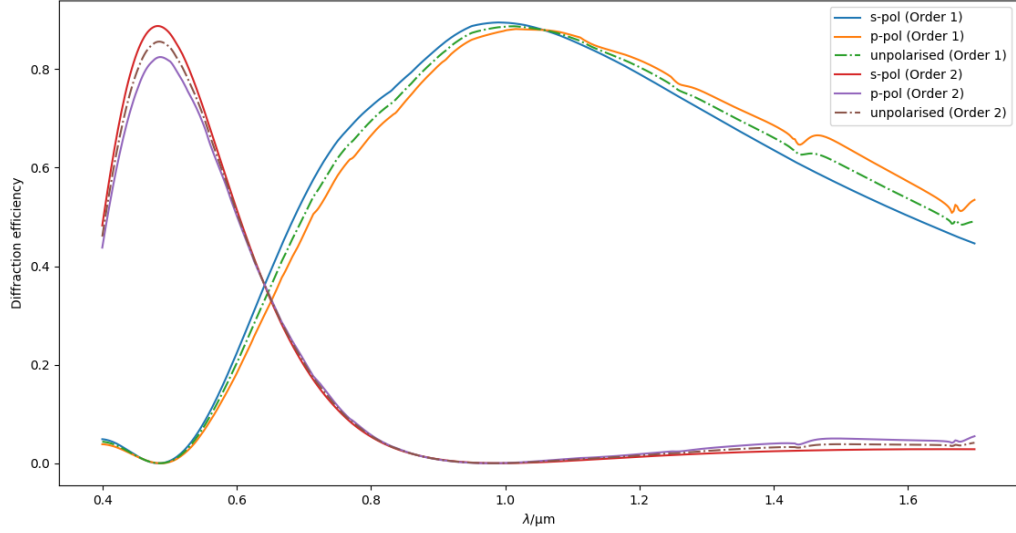


Figure 3.8: Grating diffraction efficiency for first and second order

As shown in Figure 3.6(d), the grating blaze angle was chosen to maximise the first order diffraction efficiency of the grating over the InGaAs sensor wavelength range. This limits the first order diffraction efficiency in the visible wavelength range. However, the second order diffraction efficiency is maximised at 500 nm, as shown in the full grating efficiency plot shown in Figure 3.8.

To take advantage of this, a compact visible camera was added, positioned so the sensor was centred on the second diffraction order, shown in Figure 3.9. A 1000 nm long pass dichroic mirror was used to separate the VIS and SWIR cameras, with custom camera and mirror mounts machined to accommodate the tight packing requirements. A rendering of this configuration is shown in Figure 3.10. The visible camera, combined with the dichroic fold mirror and attachment hardware, adds approximately 80 grams to the weight of the instrument. With a low profile right-angle USB connector attached, the secondary channel adds 30 mm in height to the profile of the camera system.

Although the silicon camera sensor was positioned to capture the second diffraction order, the large size of the sensor enables imaging of the entirety of the first and

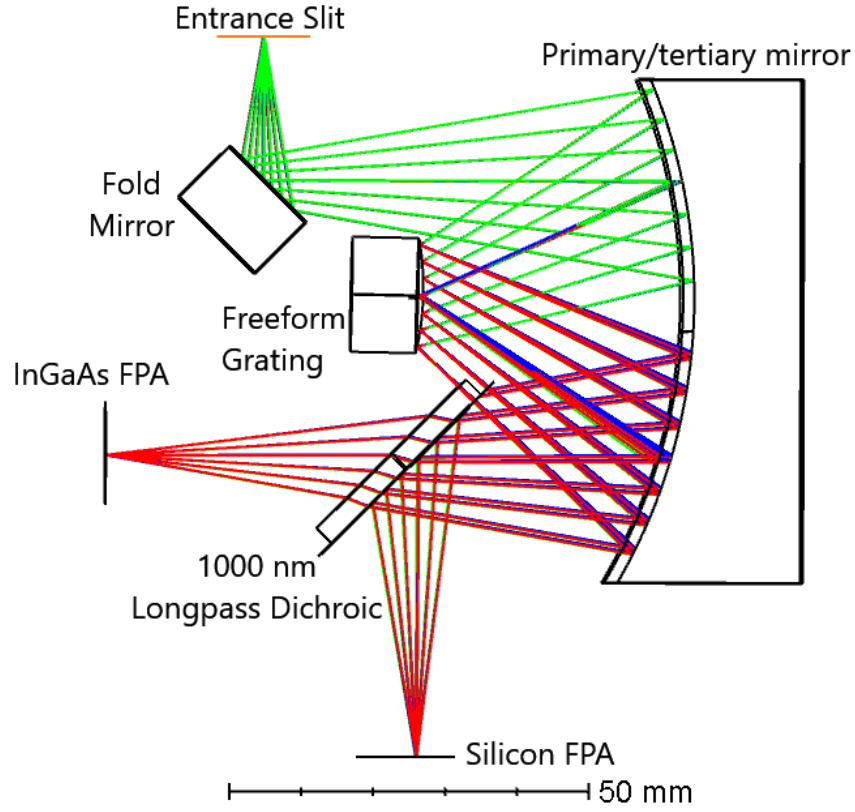


Figure 3.9: Optical layout of dual channel camera system

second orders simultaneously. Due to this, an overlap occurs between the 800-1000 nm range of the first order and the 400-500 nm range of the second order. The resulting spectral mixing prevents the use of either of these spectral ranges without the use of a cut-off filter. To solve the problem, either a 500 nm long pass or 800 nm short pass filter can be used. A 500 nm long pass filter results in the first order being used, with a spectral range of 500-1000 nm and a dispersion of 4.4 nm per spectral pixel. An 800 nm short pass filter can also be used, this time targeting the second diffraction order, resulting in a spectral coverage of 400-800 nm and a dispersion per pixel of 2.2 nm.

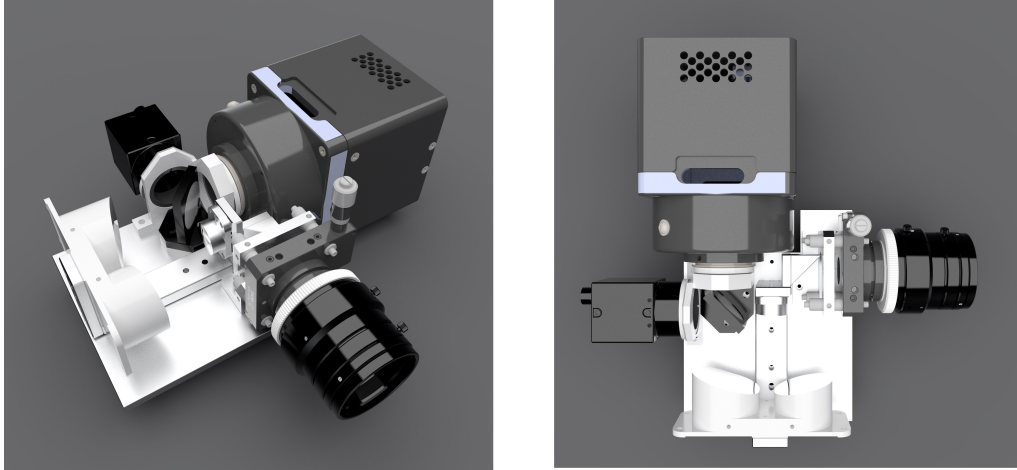


Figure 3.10: Rendering of the dual camera instrument

3.6 Enclosure

The enclosure of FYMOS was also a key design component, acting both as a light proof cover and as structural support for the instrument. With the Photonic Science AK104 camera comprising almost half the weight of the instrument, the case acts as a support to hold the camera rigidly in alignment with the rest of the optical system. The case also provides the mounting point necessary to attach the instrument to motion platforms.

While the initial case prototypes were produced by fused deposition modelling (FDM) 3D printing, it was found that enclosures made with both PLA and ABS filaments were not totally opaque in SWIR wavelengths, leading to poor S/N ratios as stray light bled through the enclosure. As many parts of the casing are under 3mm thick, the 3D printed parts were mostly solid, resulting in a relatively heavy case weight of 370g. Due to the layering process by which FDM parts are manufactured, they inherently have one direction of reduced strength. When operating on very hot summer days, some layers can start to peel away, weakening the part. An example of a 3D printed casing is shown in Figure 3.11(a).

To overcome these problems, other methods of case manufacturing were investigated. One of the most promising candidates for a suitable material was carbon

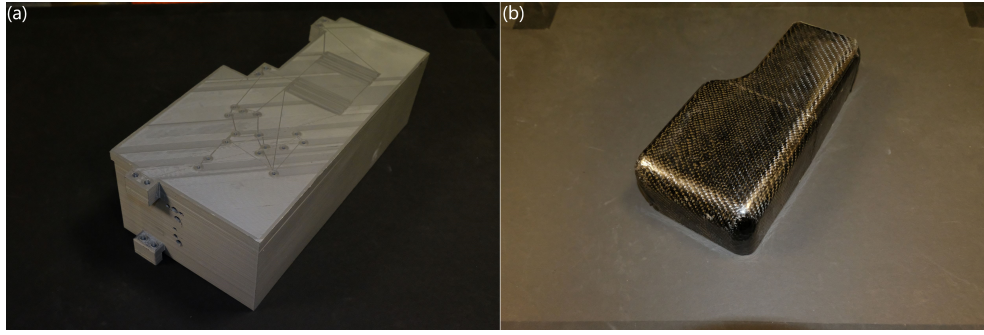


Figure 3.11: (a) 3D printed casing in PLA, (b) Prototype single piece carbon fibre case

fibre. By hand laminating sheets of carbon fibre into a 3D printed mould, a very thin, lightweight, and strong casing could be formed. The main challenge with using carbon fibre is the lay-up process, with right angle corners in particular creating opportunities for kinks and folds to form in the carbon fabric. To test what was possible to manufacture, a prototype case featuring a range of curvature radii was created, shown in Figure 3.11(b). From this, it was found that a 17 mm radius could be reliably produced.

The main advantage of the carbon fibre part over the 3D printed one is the weight. The current weight of the single channel FYMOS imager, including the fibre optic system described in Chapter 4, is 1349 grams. The prototype carbon fibre casing is approximately one third the weight of the 3D printed variant. Even including the additional mounting brackets, the carbon fibre case offsets as much weight as the small visible channel camera and dichroic, enabling the extended range dual camera system to be made without a weight penalty.

Due to the time constraints placed by COVID-19 on the project, the final carbon fibre case has not yet been manufactured.

Fibre Optic Downwelling Irradiance Sensor

This section is based on a paper published in Optics Express[98]. It covers one of the main challenges found when first setting up the system for use outdoors, namely dealing with fast moving intermittent cloud cover and its effects on accurately recovering remote sensing reflectance data. A review of common techniques from literature is provided, followed by details on the optical design and results from from a solution which is presented in this thesis. The solution is based on a Fibre Optic Downwelling Irradiance Sensor and is called FODIS in the following sections. The results section features slices of datacubes recorded by the instrument. For more details on how these are created, see Chapter 5.

4.1 Fibre Calibration Channel

One of the key challenges to achieve true and accurate reflectance data in passive aerial remote sensing is the solar irradiance calibration. The accuracy of the data is affected by illumination variation during the acquisition particularly during cloud cover, with observations ranging annual cloud cover between 66-70%. [99] This heavily impacts traditional high altitude or satellite SWIR instruments, as

these wavelengths do not penetrate cloud cover. Using small UAV platforms that can fly at altitudes far below the cloud ceiling, compact hyperspectral imagers can be guaranteed direct line of sight with the ground even on heavily overcast days.

Operating beneath the cloud ceiling presents its own set of challenges. If the cloud layer is thin or patchy, the downwelling irradiation incident on the ground surface can significantly vary over short timescales. These variations are spectrally dependant, as the water in the clouds strongly absorb light in the same wavelength bands used to measure soil moisture. Accurate measurements of the ground's reflectance are key to measuring accurate soil moisture levels, meaning these variations in incident light level must be measured and accounted for. [100]

This can be done in several ways. The simplest method is to place reflectance standards at set ground control points, which are then overflown by the drone. [101] If several identical panels are placed down and measured, changes in incident light intensity can be calculated and interpolated between the panels. This method can work if lighting conditions in the field are relatively stable, but will struggle to completely account for conditions with fast moving cloud cover, often seen in temperate regions. These panels also need to be physically placed in suitable locations in the field before the start of each measurement campaign, and removed again at the end. For large areas, this can result in impractical set-up and tear down times.

Another commonly used method for small area UAS surveys is to set up a dedicated ground based spectrometer to continuously measure downwelling irradiance data. [102] This solution provides much higher temporal resolution than reflectance panels, but can be difficult to apply for large survey areas. In sparse cloud cover conditions, the area on the ground affected by a passing cloud can be smaller than the survey area, leading to the UAS and the ground system receiving different illumination levels. This is demonstrated in Figure 4.1, which shows the shadows of a passing cloud moving over a field.

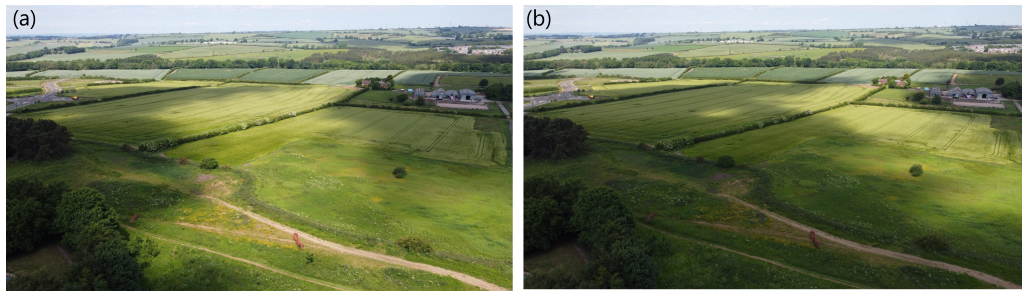


Figure 4.1: Example of the non-uniform lighting conditions caused by intermittent cloud cover. Two images recorded 6 seconds apart, using a DJI Mavic Mini.

This problem can be solved by moving the downwelling irradiance sensor from the ground onto the drone. [103] Generally this is done using a second compact USB spectrometer mounted to the top of the UAS, fitted with a skyward facing optical diffuser to couple in light from a wide acceptance angle. This enables measurement of downwelling irradiance at the drone position to be monitored continuously. This method does have some trade-offs compared to ground based incident light sensors. Adding a secondary spectrometer to the UAS adds weight, power, and packaging complexity. Increasing the weight and power requirements of the sensor payload decreases the possible flight time of the aerial platform, and places a lower limit on the size of the platform necessary to fly with the instrument. The additional spectrometer also increases the computational load on the low power single board computer used to run and log data from the instruments and the UAS flight computer.

One possible solution to this problem is to use a passive fibre optic system to sample incident light onto the main camera sensor, removing the need for an additional spectrometer. While this method has been used with some full size instruments like the original AISA Eagle, the compact optics necessary for small UAV based instruments have made this more challenging to implement. The following describes an energy budget estimate to determine the requirements for the collection and throughput of solar irradiance to enable simultaneous measurement of both downwelling irradiance and science data on the science camera, with a single common exposure time.

4.2 Throughput Analysis

The choice to use a single camera sensor to record both the science and calibration data introduces a challenge in optimising correct exposure between the two signals. As the sensor has a set exposure time across the entire array, this requires the energy throughput of the calibration channel to be similar to that of the main objective lens. This requirement is complicated by the two optical paths being very different in terms of both optical elements and incident light intensities.

To simplify the estimation for the energy throughput of the lens, the soil target is assumed to behave as a Lambertian surface. The energy collected by one spatial channel on the sensor will depend on three factors: the solar irradiance incident on the soil, the area on the ground "seen" by one spatial pixel, and the ratio of the solid angle subtended by the lens from the ground to the hemisphere over which it is dispersed.

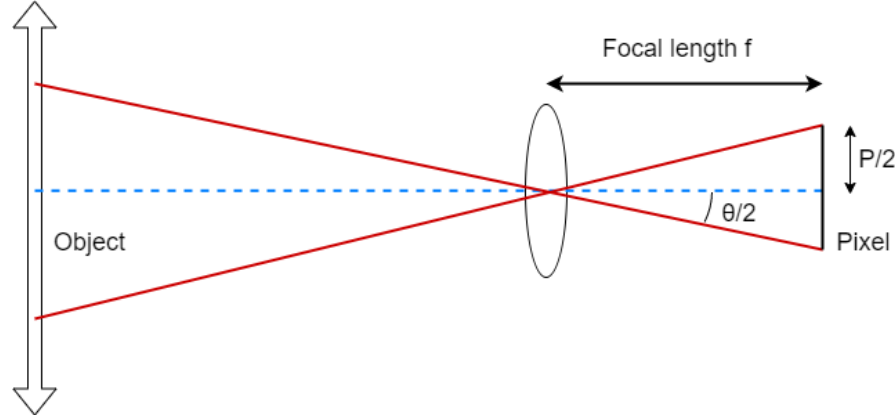


Figure 4.2: Geometry used for calculating the instantaneous field of view (IFOV) of a single pixel in a focal plane array.

To calculate the spatial coverage of each pixel, the instrument's field of view (FOV) must be calculated. The FOV of an optical system describes the solid angle over which the detector sensitive area can be projected onto the observed scene. When a detector array is placed at the focal plane of the optical system, the solid angle subtended by each pixel on the detector through the optical system is called the

instantaneous field of view (IFOV). Figure 4.2 shows a diagram for calculating this IFOV. Using the IFOV, the spatial resolution of the instrument can be calculated for known distances. Considering an optical system with focal length f with a pixel size of P , the IFOV θ can be calculated as:

$$\tan\left(\frac{\theta}{2}\right) = \frac{P}{2f}$$

$$\theta = 2 \tan^{-1}\left(\frac{P}{2f}\right)$$

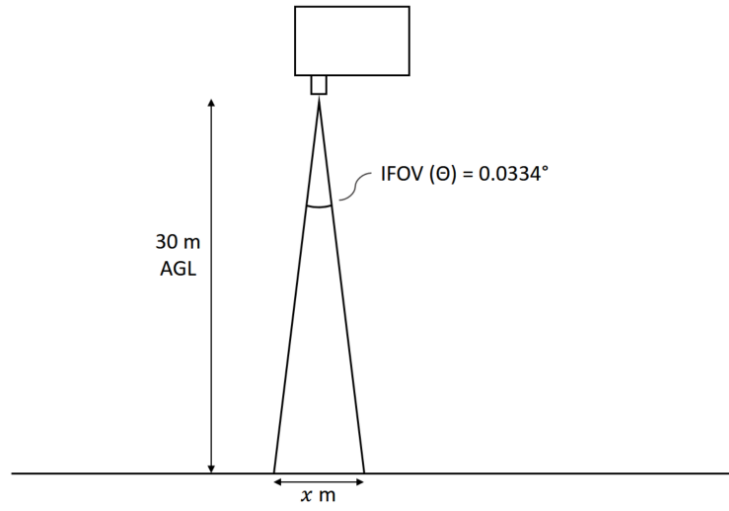


Figure 4.3: Calculating area observed on ground at an operating altitude of 30 m above ground level (AGL) using a 25 mm focal length lens and a 15 μm pixel size.

The IFOV was calculated to be 0.0344°, based on the 25 mm focal length of the lens and the 15 μm pixel pitch on the sensor of the FYMOS instrument.

$$\tan\left(\frac{\theta}{2}\right) = \frac{x}{2 * 30}$$

$$x = 60 \tan\left(\frac{\theta}{2}\right)$$

$$x = 0.018 \text{ m}$$

Assuming the pixels are square, the area on the ground observed by one spatial pixel will be $3.24 * 10^{-4} \text{ m}^2$.

The solid angle of a small object at a distance can be approximated as the ratio of its area to the square of its distance:

$$\Omega = \frac{A}{r^2}$$

Estimating the operating altitude for the drone as 30 m above ground level, and using the lens front element aperture half diameter of 10.6 mm:

$$\Omega_{lens} = \frac{\pi * (10.6 * 10^{-3})^2}{30^2}$$

$$\Omega_{lens} = 1.25 * 10^{-7} \pi \text{ sr}$$

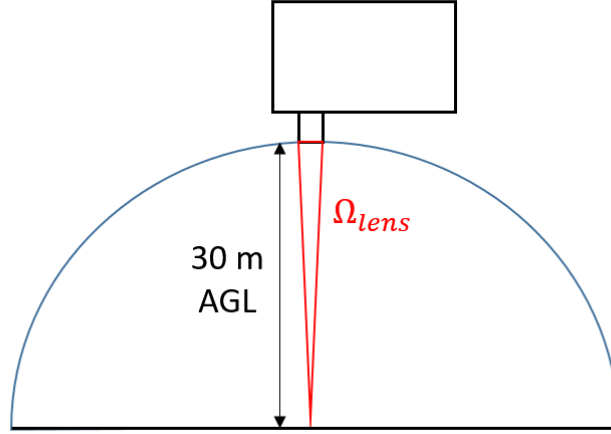


Figure 4.4: Calculating reflected energy from the ground collected by the lens using solid angles.

Assuming the irradiance at the Earth's surface to be E (W/m^2), the energy flux F collected by the lens will be:

$$F = E * R * A_{pixel} * \frac{\Omega_{lens}}{2\pi}$$

$$F = E * R * (3.24 * 10^{-4}) * \frac{1.25 * 10^{-7} \pi}{2\pi}$$

$$F = 2.02 * 10^{-11} E * R$$

Where R is the surface reflectance. If the soil has a reflectance of 0.2, then the rough estimate of reflected power to the lens will be $4 * 10^{-12} E$ [W].

The energy into the cosine corrector is simpler to estimate. The corrector is made up of an optical diffuser to collect incident light with a 180° acceptance angle, with an attached SMA connector to attach a fibre. While the incident light intensity into the diffuser will be affected by the angle between the sun and the surface normal of the cosine corrector, for this estimate the cosine corrector is assumed to be pointing directly at the sun. The energy incident on the cosine corrector is the product of solar irradiance and the area of the cosine corrector. The cosine corrector used in this instrument has an active area with a diameter of 8 mm.

$$F = E * T * \pi(r)^2$$

$$F = E * T * \pi(4 * 10^{-3})^2$$

$$F = 5 * 10^{-5} ET$$

This is the total energy flux incident onto the cosine corrector, with T being the transmission of the cosine corrector and fibre optic assembly, and r being the radius of the cosine corrector's active area. This energy will be carried by a fibre of core size $100 \mu\text{m}$, dividing the total flux across 7 spatial pixels on the sensor. This would result in an energy per channel of $7 * 10^{-6} ET$.

Comparing the two energies, a rough estimate of the combined transmission of cosine corrector and fibre system required to match the objective lens can be found.

$$E_{\text{ground}} = E_{\text{CosineCorrector}}$$

$$4 * 10^{-12} E = 7 * 10^{-6} ET$$

$$T = \frac{4 * 10^{-12} E}{7 * 10^{-6} E}$$

$$T = 5.7 * 10^{-7}$$

This is much lower than the transmission that Thor Labs states for their small cosine correctors, which are listed at around 0.1-0.4%. This suggests that the transmitted beam from the cosine corrector will be much higher than the transmitted intensity from the lens. This means it should be possible to attenuate the

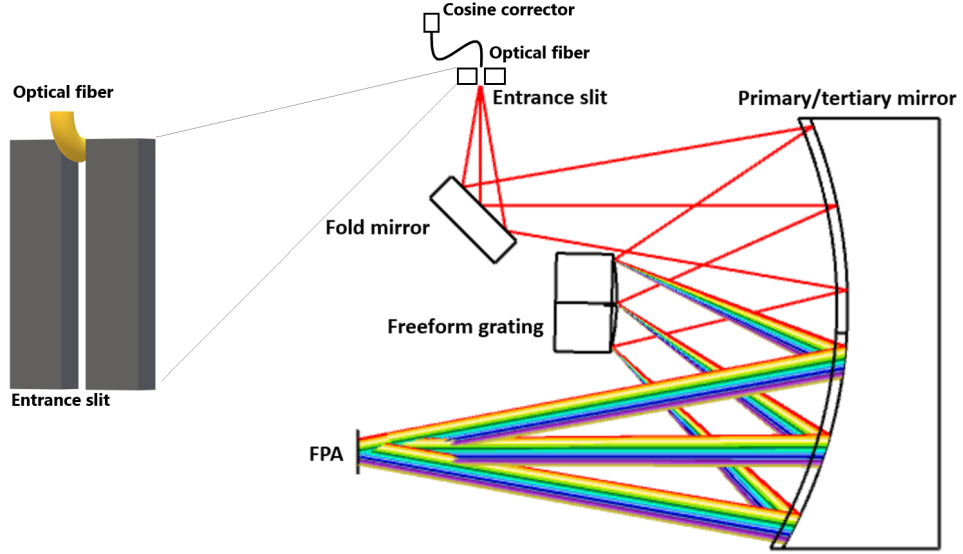


Figure 4.5: Schematic overview of the fibre calibration system. The output end of the fibre is positioned at the top edge of the slit, minimising occlusion of the slit.

cosine corrector channel to match the intensity of the science data. This is the ideal configuration, enabling full un-attenuated use of the science channel while operating the correction channel.

4.3 Optical Design

The optical path for this system begins with a cosine corrector, an optical diffuser designed to couple light into a fibre optic cable from an almost 180° hemisphere. This is used to ease coupling of light into the fibre, especially when the angle between the surface normal of the fibre and the Sun is high. The light is then coupled into an ultra low -OH fibre manufactured by Polymicro, chosen for its low absorption in the short wave infrared (SWIR) wavelength range. The fibre used has a core diameter of $100\ \mu\text{m}$, and a numerical aperture of 0.22. The other end of the fibre is positioned at the upper edge of the spectrometer entrance slit. The positioning is set so as to replace the very outermost spatial channels of the camera sensor, which would otherwise image the target through the objective lens, with the light transmitted by the fibre optic. The slit end of the fibre was just simply

cleaved, and a small diameter fibre was chosen to limit the number of spatial channels blocked. The field of view loss is approximately 3%, although this could be reduced by further revisions of mounting hardware. A schematic view of the optical system is shown in Figure 4.5.

FYMOs uses transmissive imaging fore-optics for compactness, with the two main lenses having focal lengths of 16 mm and 25 mm. The use of these compact lenses results in there being very limited space between the back of the lens assembly and the front of the entrance slit. To secure the fibre into position, a 26 gauge hypodermic needle was cut and shaped, then positioned using a small 3D printed guide. This assembly fits inside the small adapter plate necessary to attach the C-Mount lenses to the slit. The fibre was threaded through the needle, and secured using a UV cure glue. In total, the entire assembly weighs under 10 grams. Renderings of the system are shown in Figure 4.6.

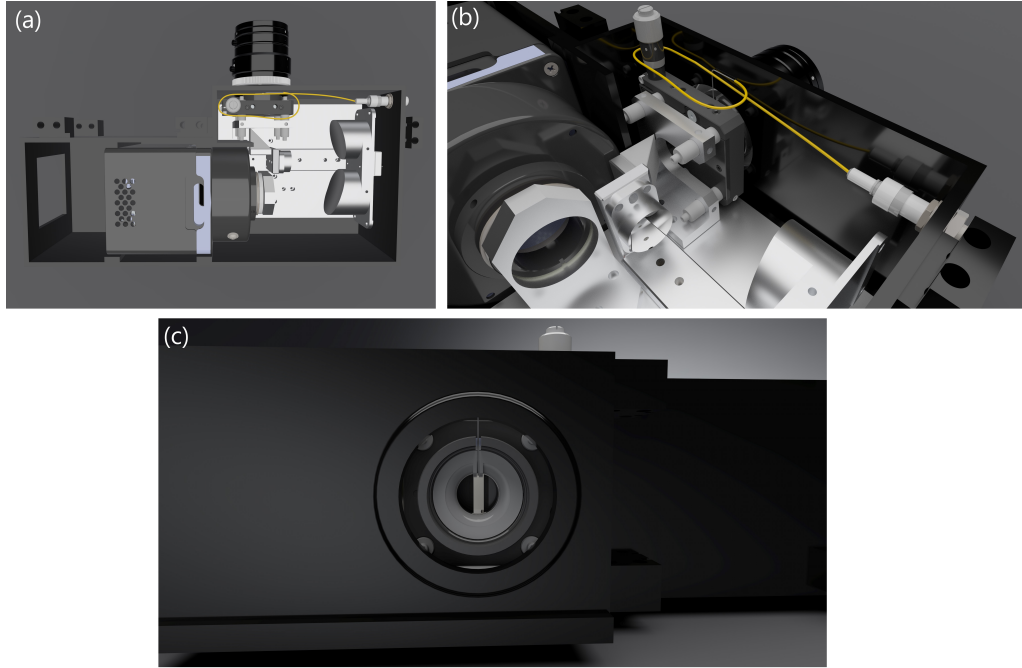


Figure 4.6: Rendering of fibre system, showing (a) a wide angle view of the system, (b), a close up of the fibre/needle assembly, and (c), a close up of the needle and mounting plate.

To increase the physical robustness of the setup, crucial for field use with UAVs, a

quick disconnect fitting was added. An SMA to SMA mating sleeve was inserted into the instrument casing, providing a way to quickly connect to SMA 905 terminated fibres together with minimal coupling loss. The addition of the fibre port means that any stresses or strains caused by snagging of the external fibre do not damage or affect the precise positioning of the internal fibre. The port also enables the external patch cable to be changed out for different lengths depending on the instrument platform being used.

4.4 Calibration Method

In order to use the hyperspectral imager and calibration channel to record calibrated reflectance measurements, the digital number ($D\#$) recorded at the camera must be correlated to the real reflectance value on the ground. This was done using a two step calibration method. Firstly the an image of the calibration panel is recorded, with the mean reflectance spectrum of the panel being calculated, measured in digital number units ($D\#_{Panel}$). The ratio between the recorded spectrum of the calibration channel ($D\#_{CC}$) and the mean panel reflectance is then calculated, enabling measurements of the calibration channel to be correlated to a true calibrated reflectance. This flow is summarised in equation 4.1. A scaling factor (SF) is added to account for the reflectance of the panel, which may be changed depending on illumination conditions and test soil sample reflectance. A 50% reflectance panel was found to have a close match to the reflectance of dry soils, enabling both the panel and the soil to be correctly exposed at one exposure setting.

Before each measurement campaign, a series of dark frames are recorded and averaged, and subtracted from each science image before reflectance processing. White flat frames were recorded in the laboratory for each F-stop of the objective lens, enabling flat field correction to be applied.

$$Reflectance = \frac{D\#_{sample}}{D\#_{CC}} \times \frac{D\#_{CC}}{SF \times D\#_{Panel}} \quad (4.1)$$

The main sources of uncertainty in the reflectance calculation are the spectral reflectance of the calibration panel, and the read noise of the camera sensor. Across the wavelengths used, the 50% reflectance panel had a reflectance of 50.9 ± 0.8 %. The signal to noise ratio (SNR) of the Photonic Science camera can vary with gain settings and exposure time, corresponding to changes in available illumination. In laboratory conditions, a typical SNR value of 100 was common, with digital number noise contributing around a 1% error for single pixels reflectance values. This results in reflectance values generated from single pixels having uncertainties of the order ± 1.8 %. By averaging over a small number of spatial pixels (such as a moving 5×5 pixel square), the SNR can be increased to 360, reducing the uncertainty contribution of the camera digital noise to 0.27%. This can decrease the overall uncertainty of reflectance measurements to 1.07%, at the cost of a slight reduction to spatial resolution.

4.5 Demonstration

To demonstrate the use of the fibre calibration channel, the system was set up outside on a tripod, using a computer controlled rotation stage to provide scanning movement for the hyperspectral imager. This set-up can be used with the camera in two orientations, either facing horizontally outwards or vertically downwards, depending on the desired scene.

With the camera placed in the horizontal position, a scene was recorded looking out over the field behind the NETPark Orbit building workshop. The image was recorded on a day with patchy cloud, as evidenced by the resulting raw image data shown in Figure 4.7(a). The image was recorded with the scan drive moving from right to left, with the image being captured over approximately 10 seconds. The bright and dark stripes on the image are due to the effects of a cloud moving past during the exposure. The recorded spectral signal from two patches of identical grass is shown in Figure 4.7(c), with a five fold peak decrease in signal occurring

at some wavelengths. Without measurement of the incident illumination levels, determining whether this effect was due to "darker" grass or reduced incident light intensity would be difficult, and estimating the magnitude of any correction harder still. For reference, an RGB image taken from a Google Pixel 4a is shown in Figure 4.7(e).

Using the data collected by the calibration channel, much of the error in measured reflectance can be corrected for, as demonstrated in Figures 4.7(b) and 4.7(d). While the overall correction quality of the scene is good, these figures highlight some of the limitations of this technique. Firstly, both figures show more noise in the areas captured while shadowed by cloud. As the raw signal goes down due to the overcasting, the signal to noise ratio of the camera drops. When these regions are boosted back up during correction post-processing, the result is noisier images and spectra. This could be corrected for using an auto exposure algorithm, using the measured intensity from the calibration channel as a light meter.

The other main factor limiting the technique is the viewing geometry. In the horizontal configuration, the camera is looking over a relatively large distance, meaning that the cloud cover is not uniform over the whole scene. This results in some of the curved banding shown in Figure 4.7(a), with the motion of the cloud into the plane of the picture combining with the line scan capture method to create this effect with depth. This curved banding would be difficult to correct for without estimating cloud velocities. The effect is reduced by decreasing the horizontal coverage of the camera, such as when it is facing downwards in the vertical position.

With the camera positioned in the vertical orientation, hyperspectral images of a tray of dry soil were recorded. The soil was prepared by oven drying a local soil sample to ensure uniformity in its moisture content. The tray was imaged under both blue sky and cloudy conditions. A hyperspectral image of a 50% reflectance reference panel was also captured. This can be used to correlate the signal from the fibre channel to a reference standard, enabling the data to be used to calculate

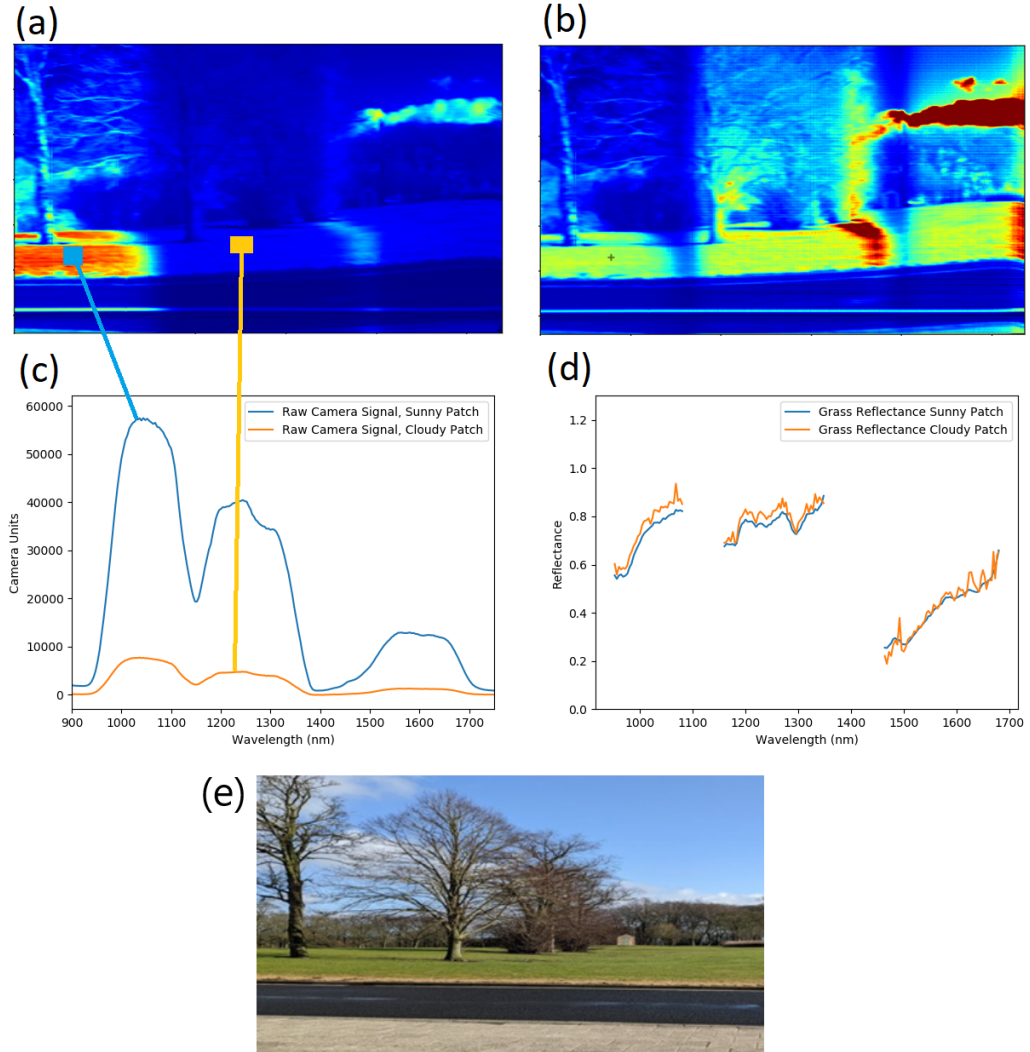


Figure 4.7: (a) Raw camera image at 1100 nm as cloud passes overhead, (b) Corrected for decrease in downwelling irradiance using cosine corrector channel, (c) Raw spectral signal measured under clear and overcast skies, (d) Corrected reflectance calculated using integrated calibration channel, (e) RGB image of scene taken from a Pixel 4a. See Visualisations for demonstration <https://sites.google.com/view/hyperspec-imager/fibre-calibration-system>

reflectance. It also enables the fibre correction method to be compared to the standard panel measurement method.

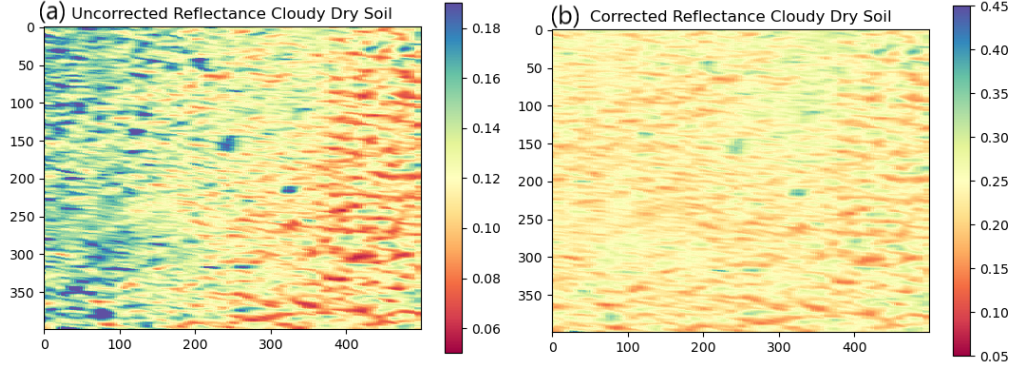


Figure 4.8: (a) Uncorrected reflectance measurement of uniform dry soil as cloud passes by. Note the measured reflectance values for the left of the image vary significantly from the right. (b) Reflectance measurements corrected for changing illumination using FODIS. With this setup, each pixel covers a square of side 0.4 mm

Measurements of the dry soil under cloudy conditions are shown in Figure 4.8. Figure 4.8(a) shows the measured reflectance map at 1220 nm, calculated using an earlier measurement of a reflectance standard panel as a reference. As the image of the dry soil was taken under changing illumination conditions, the soil at the right of the image is calculated as having significantly lower reflectance than the soil at the left of the image, despite the soil being of uniform moisture content. Without knowledge of incident light intensity, it is impossible to distinguish between reduced incident light levels and a truly darker material. Figure 4.8(b) shows a reflectance map of the same soil sample, this time corrected for varying illumination using the fibre optic calibration channel. Note that the resulting reflectance map is much more uniform in appearance. Subtracting the corrected reflectance map from the reflectance map recorded without clouds, the root mean square error was found to be 10%, with an example residual map plotted in Figure 4.9. The highest residuals were found in the areas covered by the darkest areas of cloud.

The dynamic range and signal to noise of the camera system limit the range of light intensities that can be corrected for. If the incident light intensity drops too low for

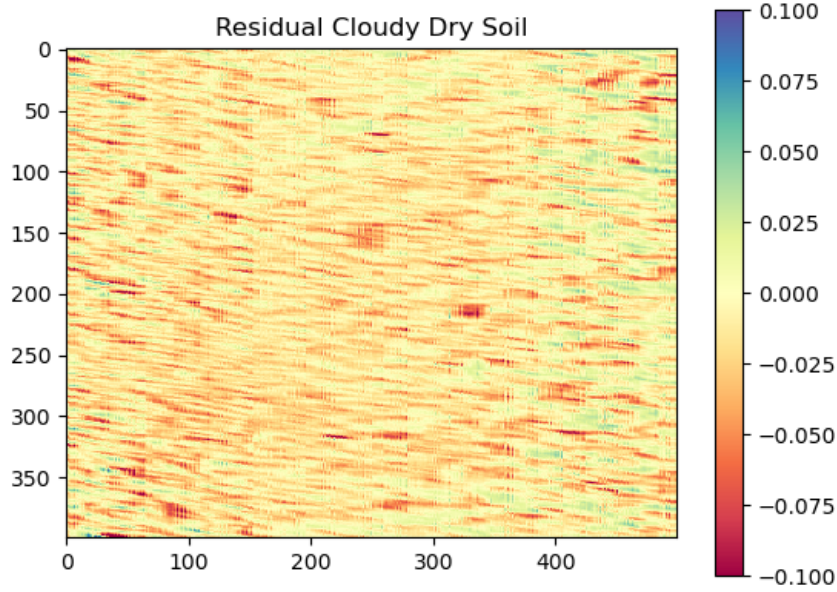


Figure 4.9: Residuals in measured reflectance after correction. Calculated by comparing measurements of the same sample taken under cloudy and blue sky conditions.

the camera's settings, noise will dominate the measured signal from both the main lens and the fibre channel. Under these conditions, better results could be obtained by using the FODIS as a light meter to guide an auto-exposure system, increasing or decreasing exposure to compensate for changing levels of illumination. At present, this functionality is limited by the eBUS SDK used to control the cameras, which only allows the exposure time to be updated once every 15 seconds. Due to the pushbroom scanning method used by this instrument, exposure time and scanning speed are linked in producing correctly shaped pixels on the ground. Significantly increasing the exposure time would require a decrease in scanning speed to prevent spatial pixels from becoming elongated in the scanning direction. While this is easy to implement using rotation and translation stages, constantly adjusting the speed of the UAV in real time during scans may be more challenging.

The data from the calibration fibre also demonstrates the need for spectrally re-

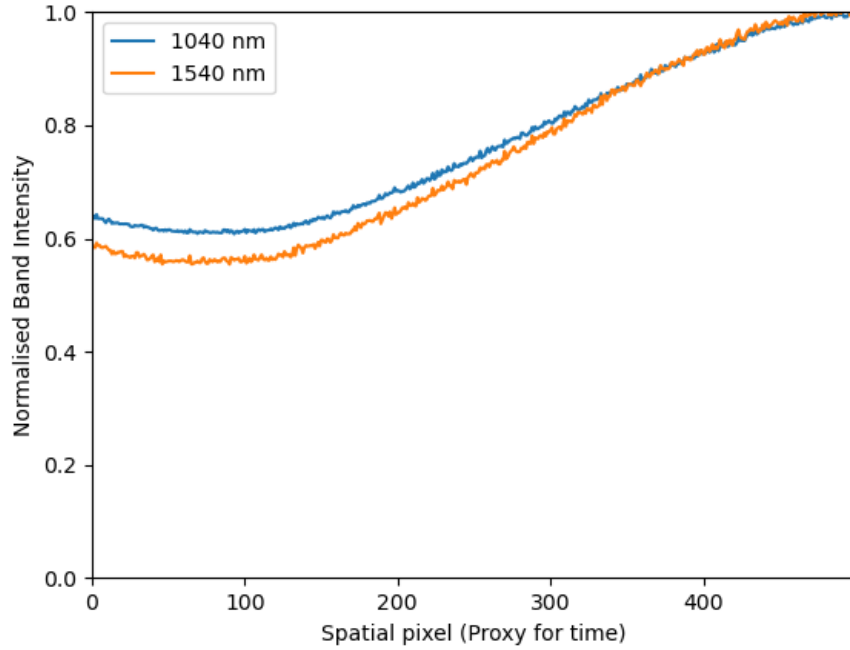


Figure 4.10: Normalised incident light intensity as measured using the FODIS for two wavelengths as cloud passes through.

solved calibration methods. Figure 4.10 shows the normalised intensity from two spectral bands plotted with time as a cloud passes. Light at 1040 nm wavelength is further from a water absorption band than that at 1540 nm wavelength, and so is less absorbed by passing cloud cover. Light metering methods based on averaging over larger wavelength ranges could under estimate reflectance at some wavelengths by 10%.

4.6 Conclusion

In summary, this chapter has presented the design and demonstration of an integrated fibre optic downwelling irradiance calibration channel for compact pushbroom hyperspectral imagers. The system uses an optical fibre assembly to directly measure incident illumination levels using the main camera sensor, enabling simultaneous measurement of downwelling and upwelling irradiance. This can be used

to calculate true target reflectance factors under solar illumination, even under changeable cloud cover. With the spatially inhomogeneous nature of cloud cover, this system can provide more accurate corrections over large areas in comparison to stationary ground station downwelling spectrometers. By making use of the main camera sensor, rather than an additional standalone spectrometer affixed to the top of the drone, the weight of the calibration system can be kept to approximate 10 grams. The performance of the system was demonstrated using a local soil sample, with reflectance measurements taken under both clear sky and intermittent cloud cover. Without correction, reflectance measurements of soil samples produced moisture content estimates 60% above the true gravimetric value. By correcting the reflectance data using the calibration channel, this can be brought down to an over estimate of around 10%. This could be improved further by adding an auto-exposure system guided by the calibration data, improving signal to noise ratio under changing cloud cover.

Data Collection & Data Processing

This chapter provides an overview of the data collection methods employed during lab and ground based use of the FYMOS hyperspectral imager. The process of forming 3D data cubes from raw sensor output is described, along with the conversion of these raw datacubes into more useful reflectance measurements. This process differs depending on the illumination conditions used during measurement. Two of the main methods for converting reflectance measurements into soil moisture contents are also detailed.

5.1 Overview

As the FYMOS hyperspectral imager is a pushbroom type imager, the methods for both capturing and displaying an image differ significantly from a standard 2D camera. The sensor captures information in 1 spectral dimension and 1 spatial dimension, meaning the system must be physically scanned along the second spatial direction perpendicular to that captured on the sensor. Each frame captured by the scan can then be "stacked" up into a 3D datacube. This datacube can then be sliced in different directions depending on the required data. Taking a slice in the

spectral direction will result in a 2D image at the chosen wavelength, while taking a "core sample" at any spatial location will return the full recorded spectrum at that pixel. A visualisation of the stacking process is shown in Figure 5.1. The process for capturing and processing datacubes is different depending on whether the instrument is being used in a laboratory under controlled illumination or used outdoors with passive solar illumination. The two methods are described in the following sections.

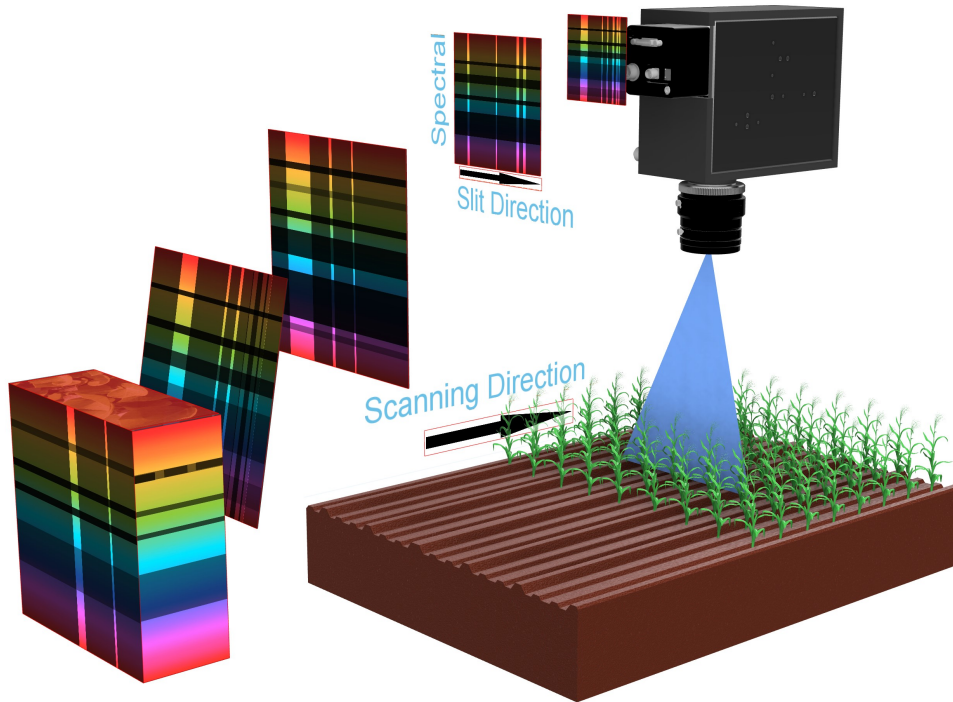


Figure 5.1: Illustration of data cube formation from individual sensor readings of a pushbroom hyperspectral imager.

5.2 Lab & Ground Based Processing

Pushbroom hyperspectral imagers rely on physical motion to build up 2D images. In the lab, this can be achieved by using linear translation stages, rotation stages, or by using scanning mirrors. Scanning mirrors were discounted due to their complexity and limited field of view, while linear stages proved impractical due to the long travel distances required to image large areas. To enable scanning over large

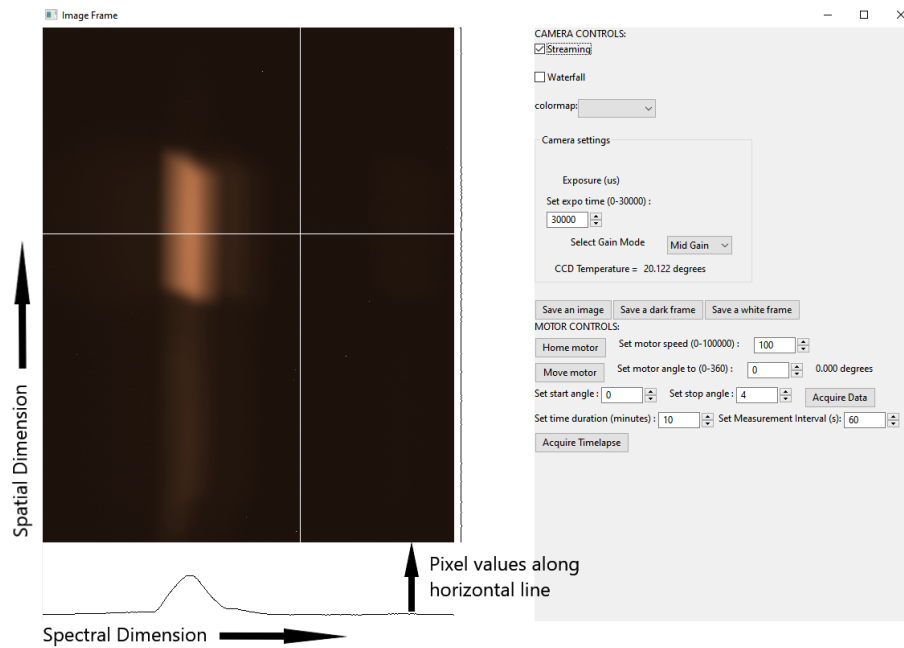


Figure 5.2: Example of the Python GUI used to control the camera and motor assembly on the ground. The GUI provides a live view of the sensor readout, enabling exposure controls and focus to be set quickly.

areas using a compact set-up, a rotation stage (Standa Ltd) was used. This computer controlled stage can be programmed to move at constant speeds. For ease of use, a Python graphical user interface (GUI) was created to control the camera and motor controller. The GUI, shown in Figure 5.2, provides a live view of the sensor readout, enabling accurate focus and exposure to be set easily. As none of the cameras used in the project have pre-built Python libraries, a Python wrapper for the C++ functions in the Pleora eBUS SDK was written. A major strength of the Pleora SDK is its support for GigE Vision, USB3 Vision and GenICam standards, across both Windows and Linux. This allows one SDK to be used to control multiple cameras across different manufacturers, significantly reducing incompatibility issues caused by running multiple sets of camera drivers.

The system has a working focal number of 2.87, and exhibits strong vignetting when the front lens aperture is set above this focal number. To calibrate for this, a series of hyperspectral images were taken of a uniformly lit spectralon panel at each aperture setting. These images are then averaged and normalised, creating a

calibration map for each full f-stop of the lens. Further images taken at a matching aperture setting can then be divided by these reference images to correct these vignetting effects, a process known as flat field correction.

Following flat-field correction, the process for completing the data calibration varies depending on the illumination source used. For indoor "table-top" experiments, small halogen sources such as the ASD Illuminator (Malvern Panalytical) and the ThorLabs SLS201L/M are used. These sources have narrow beam angles, 12° in the case of the ASD Illuminator, resulting in a noticeable fall-off in intensity over extended samples. A datacube of a Lambertian reference panel is recorded, so when dividing the flat field corrected datacube by this reference cube, a true reflectance datacube is obtained. When using this method, it is important the illumination source is not moved or changed between recording the reference panel and the science data. This requires the use of thermally stabilised light sources to prevent spectral changes in illumination due to warming of the bulb.

For outdoor experiments, it is not possible to control the illumination conditions. Clouds passing by during a scan can cause variations in incident light intensity, generating a banding effect orientated along the spatial scanning direction. This banding induces errors in the recovery of spectral reflectance, increasing the uncertainty in moisture measurements. The hardware required to correct for this is discussed in Chapter 4. Once the camera settings are decided upon, a datacube of a reference panel is recorded. This data is used to later correlate the calibration signal recorded from the fibre optic downwelling irradiance sensor (Chapter 4) to the reflectance panel used in the lab. Taking the flat-field corrected datacube, each row of spatial pixels is then divided by the corresponding irradiance measured with the fibre optic system, before being multiplied by a correction factor accounting for the intensity difference between the two paths - one going through the fibre optic downwelling irradiance sensor and the other through hyperspectral camera optics.

While raw hyperspectral datacubes tend to be very large in terms of data size, the operations required to process ground based recordings into true reflectance

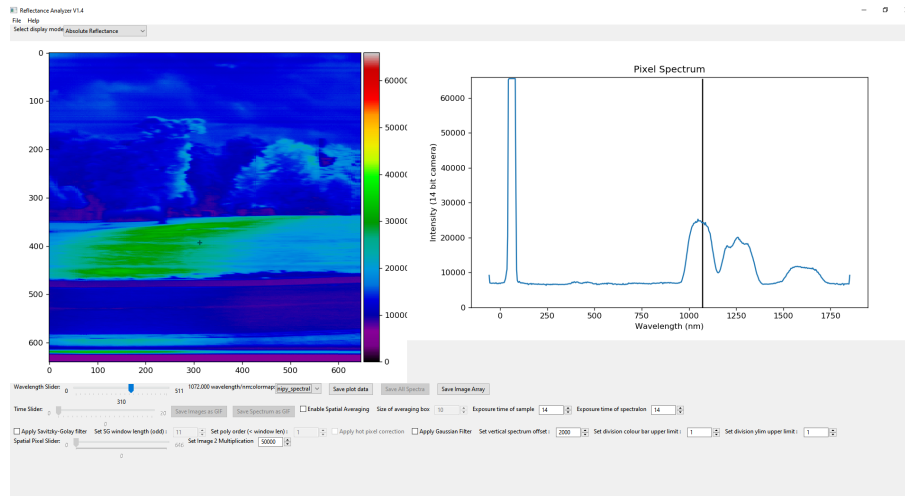


Figure 5.3: Example screenshot of the Python data analysis GUI, used to quickly check data quality in the field

datacubes are very simple, mostly straight multiplication or division between arrays. Using the Numpy Python package gives acceptable speeds when performing these calculations, enabling Python to be used for all of the processing pipeline.

A second Python GUI was written to extract the raw data and interactively display the datacube, shown in Figure 5.3. This GUI supports basic features, such as converting data cubes from camera noise to reflectance, and parsing 4 dimensional time-lapse datacubes into a series of images. The idea behind this GUI is to enable checking of data quality at the time of acquisition, ensuring correct exposure time, rotation speed, scan movement range, etc. are set correctly before large amounts of data are recorded.

5.3 Index Selection Method

Once the corrected datacube has been formed, it must be processed in order to extract information about the target sample. One of the simpler methods of working with hyperspectral data is to use spectral indices, as mentioned in Chapter 2. The idea is to select a ratio of wavelengths that, when applied to a datacube containing both wet and dry soil, the resulting histogram would be clearly bimodal.

This is demonstrated in Figure 5.4. Figure 5.4(a) shows the per pixel ratio of the measured reflectance at 1602/1516 nm of a local soil sample, prepared with specific wet and dry areas. A histogram comparing the per pixel ratios between the wet soil in the cross and dry soil in the shield of the Durham University logo is shown in Figure 5.4(b), with a clear separation shown between the different moisture levels.

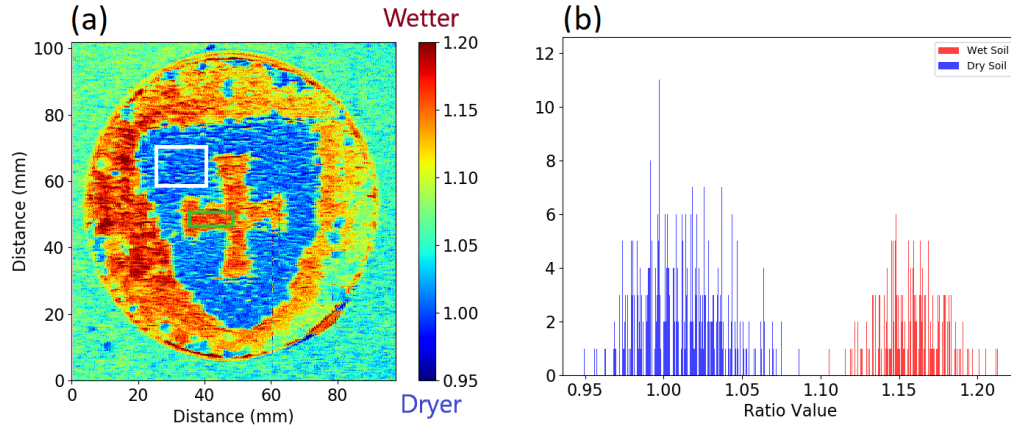


Figure 5.4: (a) Ratio map of a local soil, wetted in the shape of the Durham University Shield, with the central cross and exterior (red end of the colour bar) being saturated. Regions of interest (ROI) for wet and dry soil used in the histogram are shown, marked in green and white respectively (b) Histogram of per pixel ratio values within the marked ROIs

The problem of selecting suitable wavelengths and ratios has been tackled using many different methods. This section describes the hyperspectral image analysis method (HIAM) published in [98], itself inspired by [104]. The main goal of this work was to create a method for automatically searching for suitable wavelengths to use in calculating soil moisture content from soil reflectance data, with the aim to find the ratio with the strongest contrast between dry and wet soils. To do this, an automated method based on histogram and contrast space analysis was devised to search through a user selectable wavelength range to find a suitable ratio providing high contrast between wet and dry soils.

In order to determine the best wavelengths and ratio type (see Table 5.1) to produce the highest contrast between wet and dry soil, the metrics describing a high contrast histogram had to be identified. The two main criteria chosen were the

Contrast Ratio	Formula
Simple	$\frac{Reflectance_{\lambda_1}}{Reflectance_{\lambda_2}}$
Weber	$\frac{Reflectance_{\lambda_1} - Reflectance_{\lambda_2}}{Reflectance_{\lambda_2}}$
Michelson	$\frac{Reflectance_{\lambda_1} - Reflectance_{\lambda_2}}{Reflectance_{\lambda_1} + Reflectance_{\lambda_2}}$

Table 5.1: Contrast ratios considered in this analysis

separation of the histogram means, and the standard deviations of the histograms. If the separation between the wet and dry histograms is too low, differentiation between soils at different humidity levels becomes less accurate. Similarly, ratios that produce histograms with high standard deviations could mask small changes in moisture content. This method offers a different and simpler approach to more commonly used statistical distance methods with the view to reduce the post processing required after the selection analysis. As statistical distance methods, such as the Bhattacharyya distance, could potentially output the same distance for a variety of histograms, some groups have resorted to manual sorting of results post-selection. [104]

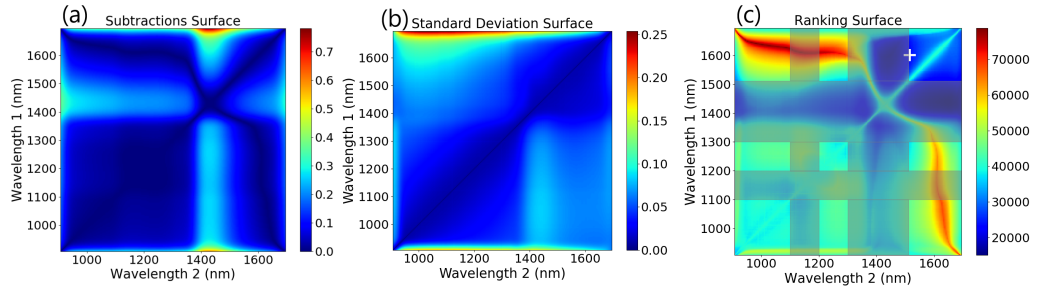


Figure 5.5: (a) Surface plot of the difference between reflectance ratios calculated for wet and dry soil (metric 1) (b) Standard deviation of per pixel reflectance ratio calculated for wet soil sample (metric 2) (c) Overall ranking surface, with darker blue colours best suited for differentiating wet and dry soil. The ratio picked for this analysis is marked with a white cross, chosen after atmospheric absorption bands were discarded (shown as greyed out).

To automate the process of choosing a suitable wavelength ratio, surface plots of the mean separation and standard deviation over a wavelength space were created. The mean contrast ratio separation is obtained by calculating the Euclidean

distance between the mean contrast ratio of the dry soil and the mean contrast ratio of the wet soil, with the result plotted as a surface plot in Figure 5.5(a). For each wavelength combination covering the InGaAs sensitivity range of the FYMOS instrument used for this experiment, the following processing was performed:

$$metric_1 = \left\| \sum_{i=1}^{N_1=ROI_{Wet} \text{ pixels}} \frac{\left(\frac{Reflectance_{Wet}(i, \lambda_1)}{Reflectance_{Wet}(i, \lambda_2)} \right)}{N_1} - \sum_{i=1}^{N_2=ROI_{Dry} \text{ pixels}} \frac{\left(\frac{Reflectance_{Dry}(i, \lambda_1)}{Reflectance_{Dry}(i, \lambda_2)} \right)}{N_2} \right\| \quad (5.1)$$

To visualise how the standard deviation of the contrast ratio varies across the wavelength range, the standard deviation of the contrast ratio for each wavelength combination in the wet soil image was calculated and plotted in a similar way, shown in Figure 5.5(b). The following processing was performed:

$$metric_2 = \sqrt{\frac{\sum_{i=1}^{N_1=ROI \text{ pixels}} \left(\frac{Reflectance_{Wet}(i, \lambda_1)}{Reflectance_{Wet}(i, \lambda_2)} - \frac{\sum_{i=1}^{N_1=ROI \text{ pixels}} \left(\frac{Reflectance_{Wet}(i, \lambda_1)}{Reflectance_{Wet}(i, \lambda_2)} \right)}{N_1} \right)^2}{N_1}} \quad (5.2)$$

Each wavelength pairing was then sorted and ranked based on these two surfaces, with each wavelength pairing being ranked highest to lowest based on the subtraction surface, and lowest to highest based on the standard deviation surface. The rankings for each test were summed, and then plotted to form the ranking surface shown in Figure 5.5(c), with the idea being that the pairing with the lowest overall rank would have the best combination of high separation and low standard deviation. A flow chart summarising the method is shown in Figure 5.6. The same method was applied using the simple ratio mentioned above, and using the Weber and Michelson contrast ratios, shown in Table 5.1. The final ranking surface for these ratios is shown in Figure 5.7. All 3 contrast ratios converged towards to the same pair of wavelengths. For this application the Michelson ratio produced the lowest contrast, while the simple and Weber ratios produced similar contrast values. For simplicity, the simple ratio was chosen for further investigation.

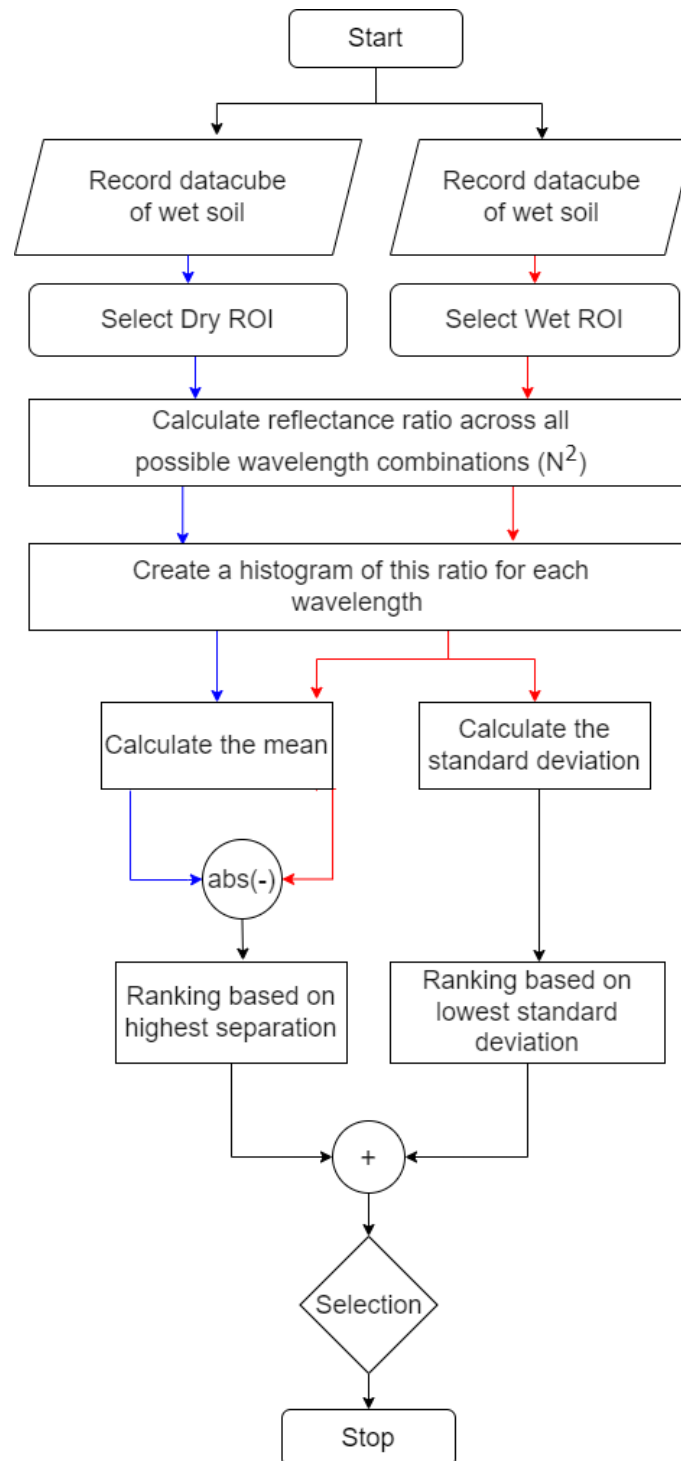


Figure 5.6: Flow chart describing the hyperspectral image analysis method (HIAM)

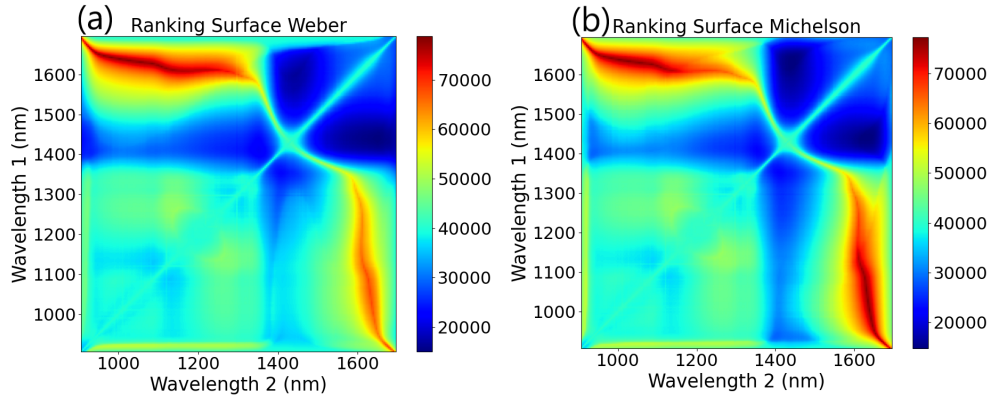


Figure 5.7: Ranking surface plots for (a) Weber contrast ratio and (b) Michelson contrast ratio

The wavelengths chosen for analysis were limited by the operating wavelength range of the FYMOS hyperspectral imager. As this instrument is using a high specification compact InGaAs camera, this wavelength range is applicable to many of the current generation of compact hyperspectral imagers. For the soil used in this experiment, the ratio of 1524/1480nm was found to be best. However, these wavelengths are close to the 1400nm atmospheric water absorption band, limiting the use of the ratio under certain lighting conditions, such as under variable cloud cover. Restricting the wavelength range to wavelengths available under solar illumination, a reflectance ratio of 1602/1516nm was chosen. A comparison of these chosen wavelengths against WISOIL and NSMI is shown in Figure 5.8.

Experimental Data

To test the use of this reflectance ratio in remote soil moisture measurement, an initial experiment was performed in the lab under controlled illumination. Soil samples were prepared by placing oven dried, sieved soil into 9 cm diameter petri dishes. The dishes were then hydrated to saturation, and oven dried at 60 °C until reaching the desired weight. The samples were then sealed and allowed to cool to room temperature over 24 hours to aid in uniform distribution of water content.

A hyperspectral image of each soil sample was then taken using the FYMOS hy-

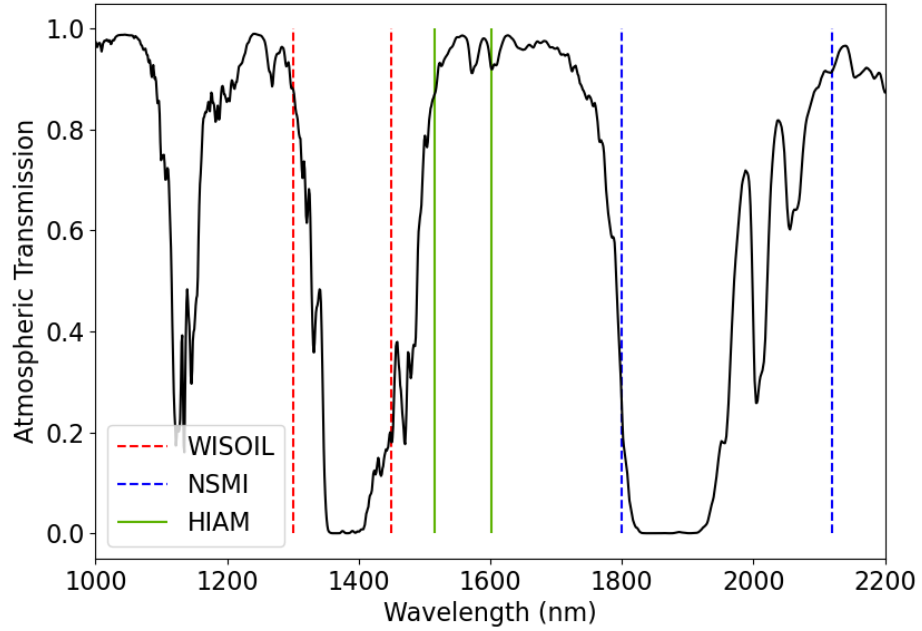


Figure 5.8: Wavelengths comprising existing indices WISOIL and NSMI, along with the index proposed in this work, imposed on atmospheric transmission spectrum computed using LOWTRAN. [105]

perspectral imager, set up normal to the soil surface and scanned using a rotation stage. [106] The light source was an ASD Illuminator halogen lamp placed at a 15° angle to the soil surface. From the hyperspectral datacubes, a mean reflectance ratio for each sample was calculated to create a calibration curve. Two more sets of soil samples from the same area were then prepared in an identical way, with their ratios plotted against the calibration curve shown in Figure 5.9(a).

A similar set of soil samples were then measured outdoors under varying lighting conditions. The hyperspectral imager was set up on a tripod, orientated to prevent shadowing on the soil samples. One set of measurements was taken under a clear sky with a low winter sun (solar elevation angle of 22.5°), shown in Figure 5.9(b). A hyperspectral image of a 50% reflectance Lambertian panel was used to measure the incident solar illumination, and to calibrate the measured soil data to true reflectance factors. The ratios calculated for these samples agree strongly with the measurements taken in the lab.

Using datasets provided by Dupiau et. al. [107], the wavelength ratio was tested

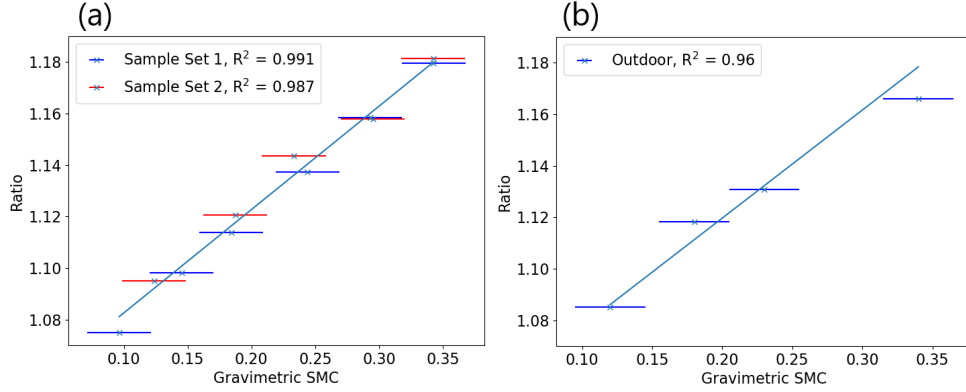


Figure 5.9: (a) Soil ratios from two sets of samples plotted against a mean calibration curve. These samples were measured under controlled illumination. The predicted and measured SMC_g values agree within a 3% error. (b) Soil samples measured under solar illumination, plotted against the same calibration curve.

against a range of various soil samples. As the spectra from these datasets have been captured using point spectrometers, the spatial imaging data required for the histogram analysis is not present. Instead, the best fit wavelengths found for the local soil were used for every database.

The datasets chosen for validation were Les08, Lob02, Bab16 and Dup20, described in [72, 107]. These datasets were chosen as their soil sample preparation methods and measurement geometry closely matched the experiments used in deriving the ratio. As each dataset contains a large number of soil samples, for brevity a set of 6 samples covering a range of soil texture characteristics was chosen for illustration here. Figure 5.10 shows the calculated reflectance ratio plotted against gravimetric soil moisture content for a variety of hydration levels and soil compositions. Individual soil samples have been removed where there was a suspicion of specular reflectance marked in the database. In Figure 5.10(c-f), a calibration curve for has been calculated for each individual data set, with the fit being good for most soil types. Where multiple sets of soil samples from the same region were available, they were plotted together, with a calculated mean best fit curve. The fit between these soil samples is still good, with examples of this are shown in Figure 5.10(a) and (b).

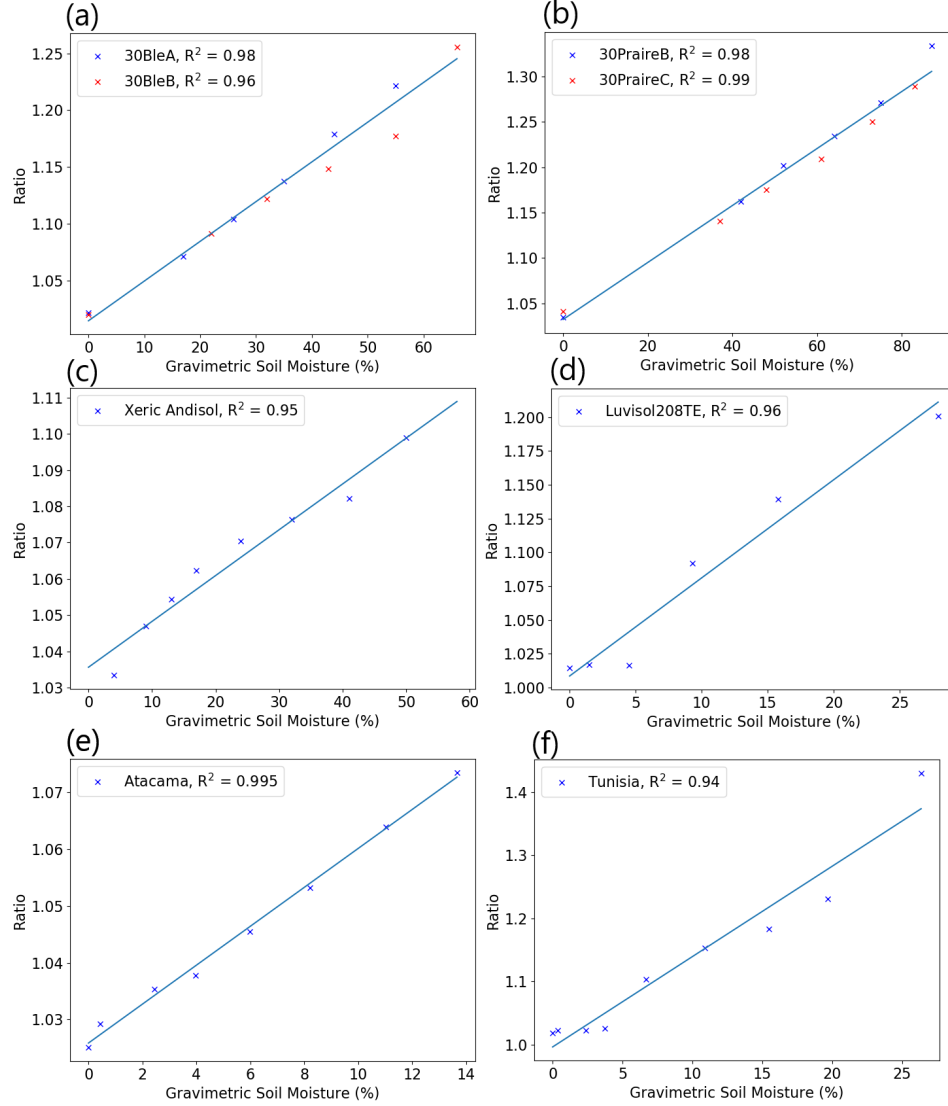


Figure 5.10: Calibration curves created for datasets provided by [107].

Feeding the calibration curves from Figure 5.10 back into the same datasets, the predicted and measured soil moisture contents can be compared, shown in Figure 5.11. The predicted values for Figures 5.11(a) and (b) were based off the mean best fit curves for each region. The datasets are best described by linear best fit curves, of the type $y = mx + c$, with m being the gradient and c being the y (Ratio) intercept. The predicted soil moisture content can then be found for a given soil moisture sample by using equation 5.3, where $Ratio_{obs}$ is the measured spectral

index.

$$SMC_{Predicted} = \frac{Ratio_{obs} - c}{m} \quad (5.3)$$

Generally, there is good agreement between the predicted and measured soil moisture contents, with an RMSE under 5% for all datasets. The fit of the model tends to struggle at low soil moisture contents (<5%), but tends to hold well from 10% SMC up until soil saturation. Sensitivity at lower moisture contents may be better in sandy soils, shown in Figures 5.11(e) and (f). While simple linear fits work for the majority of the soil datasets, some soils such as those shown in Fig 5.11(c) would benefit from non linear modelling. This suggests that the best performance could be found by calibrating the model independently for different soil types.

The estimated error in soil moisture retrieval can be calculated by taking into account a variety of factors. The three largest contributors to uncertainty in this model are the reflectance deviations of reflectance calibration panel, the digital number noise from reading out the camera's sensor, and the uncertainties in the intercept and gradient of the calibration curve during fitting. As discussed in Chapter 4, the expected reflectance error, which derives from reflectance panel deviations and camera noise, is estimated at approximately 1.1%.

The errors in gradient and intercept of the model best-fits depend on the soil sample under test. Across the soil samples plotted in Figure 5.11, the mean gradient uncertainty was 6.5%, while the mean intercept uncertainty was much lower at 0.7%. As expected, the datasets exhibiting the highest fitting uncertainties were those with the lowest R^2 values. These upper and lower uncertainty bounds were propagated numerically through the model, with the assumption that the uncertainty in the model (σ_{model}) is equal to

$$\frac{f_{model}(params + uncertainties) - f_{model}(params - uncertainties)}{2}$$

Using this method, the mean uncertainty of the HIAM model across the tested data sets was 4.2%. This uncertainty is around 1% than that of well developed direct

contact soil moisture sensors, such as the METER TEROS 11/12, while enabling much higher spatial coverage.

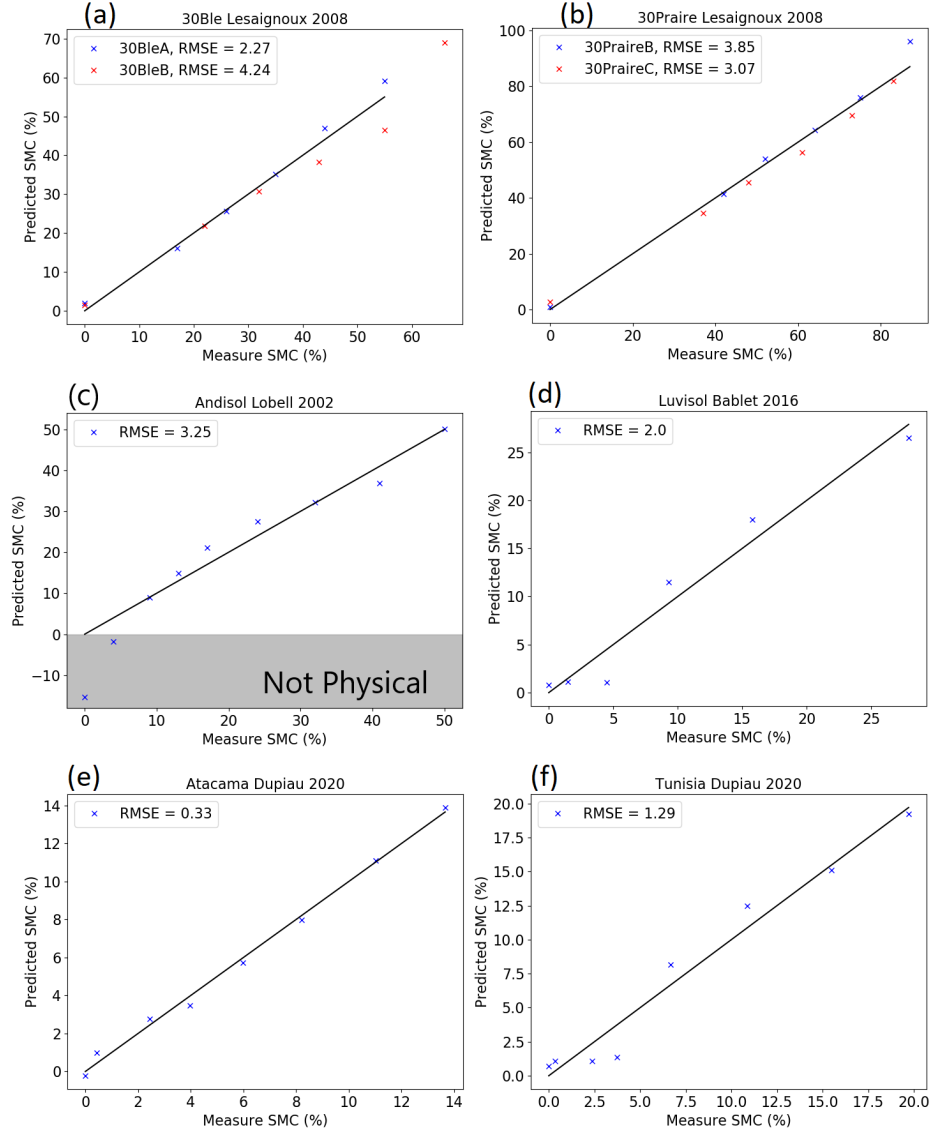


Figure 5.11: Predicted vs measured soil moisture content from calibration curves created in Figure 5.10.

Method Discussion

For this analysis, the two images chosen were of soil samples at the extreme ends of their soil moisture range, with one being oven dried and the other being brought close to saturation. As this method is purely image analysis based, with no under-

lying soil reflectance model, the method should be material agnostic. Besides soil, lab experiments have shown this method to work with other biological samples such as detached leaves, along with man made materials like fabric and paper. More details on the other uses of this method, mostly focused on plant health, will be given in later chapters.

From analysis on publicly available data sets, this index performs best at medium to high soil moisture contents for the loamy soils typical of farmland. Performance at low moisture contents is better in sandy soils, suggesting a link between the optimal soil moisture content range and the maximum soil moisture content supported by the soil before saturation. The performance is similar across a variety of soil classes, with marginally lower RMSE values found for clay loam/silty clay loam soils, where soil class data is available. However, only around half of the data sets contained textural information, making conclusions on the effects of soil texture difficult to draw.

5.4 Radiative Transfer Models

As discussed in Chapter 2, radiative transfer models represent an alternative spectral reflectance based method for measuring soil moisture content. For this work, the model tested was the recently developed MARMIT model, as the original development of the model was based on NIR/SWIR measurements in a similar wavelength range to the FYMOS instrument. [72]

Experimental Data

The main practical difference between radiative transfer models and spectral indices is that radiative transfer models attempt to model a sample's continuous spectrum, rather than set narrow wavebands. For more details on the parameters used in the MARMIT model, see Section 2.2.3. In order to test the use of the MARMIT model,

a series of soil samples taken from Spen Farm (managed by Leeds University) were used. The samples were prepared in a similar way to those used in Section 5.3. Using controlled illumination in a laboratory dark room, the spectral reflectance of the soil samples was recorded, plotted as the crossed lines on Figure 5.12. Looking at this plot, the two key spectral features of wet soil can be seen. Firstly, as the moisture content of the soil increases, the overall reflectance of the soil decreases at every wavelength. Secondly, it should be noted this decrease is not uniform, with a higher decrease in reflectance inside the water absorption bands like the 1400 nm band seen here. It is these features that are used to estimate water content in the soil.

Taking the dry soil reflectance as the base, the MARMIT model was then used to fit the dry reflectance to each hydrated soil sample, outputting a corresponding "mean water depth" value for each moisture content. The fitting was calculated using a least squares method, with the best fit for each soil shown as a solid line on Figure 5.12.

To enable the use of the model to remotely estimate moisture content, a calibration curve linking the "mean water depth" to the gravimetric soil moisture content must be calculated. From the data, the best fit line is an S-shape, following a sigmoid function:

$$SMC = \frac{K}{1 + ae^{-\psi\varphi}} \quad (5.4)$$

where K is the maximum value of the sigmoid curve, a is a translational scaling factor along the φ axis, φ is the "mean water thickness", and ψ the gradient of the curve. The K , a and ψ parameters are all specific to each soil, and so for best results a calibration curve must be measured for each different type of soil. The calibration curve for the farm soil from Leeds is shown in Figure 5.13. As can be seen from the curves, the best fit between the model and measurements was when the soil moisture content was in the middle of the possible range for the

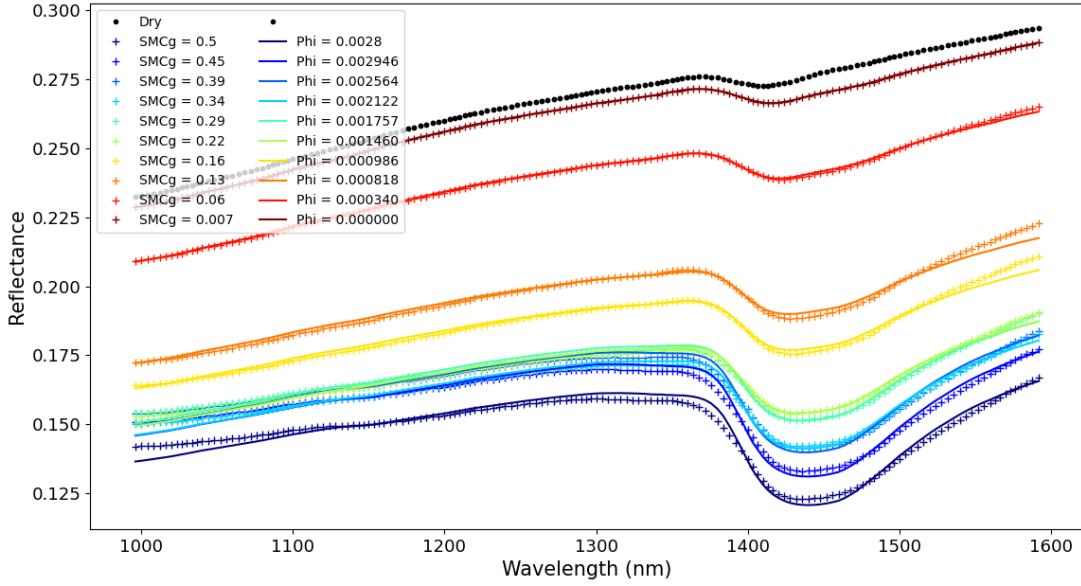


Figure 5.12: Plotting the mean reflectance spectrum of loose soil from Spen Farm in Leeds at a range of moisture levels. The lines marked with "+"s are the measured reflectance, while the solid lines are the calculated best fit using the MARMIT model. Measurements carried out under controlled illumination in a lab.

test soil samples. Particularly at high moisture contents, reflectance in the water absorption band is underestimated, causing errors in the moisture estimation when the model is used for prediction. This is in line with what was reported in the original MARMIT paper. [72]

Two more test samples were prepared, taken from another area of the same field. The data from these samples was not used in producing the calibration set. A similar pattern is seen here as with the other measurements, where the soil moisture prediction for mid level water content is more accurate than for more saturated soils. These test points were plotted against the calibration curve, shown in Figure 5.14.

A sample for testing contrast of the model was prepared in a similar manner to Section 5.3. The soil was heated using a hot plate to increase rate of evaporation, enabling a time-lapse of the soil drying to be recorded. The model showed very sharp contrast between the dry and wet soil regions, with an example image shown

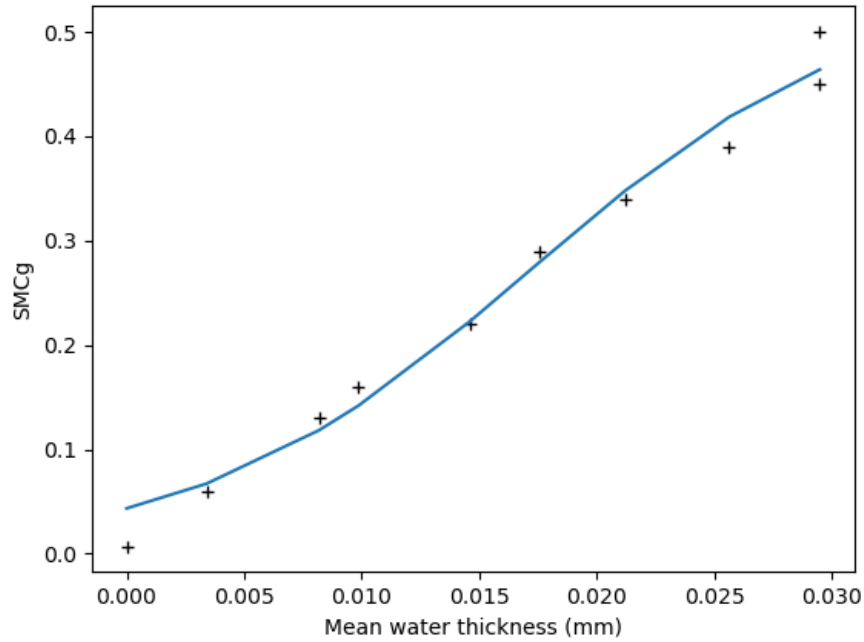


Figure 5.13: Calibration curve linking the mean water thickness estimated by the MARMIT model with the gravimetrically measured soil moisture content of the test samples. The best fit curve is plotted as a sigmoid function.

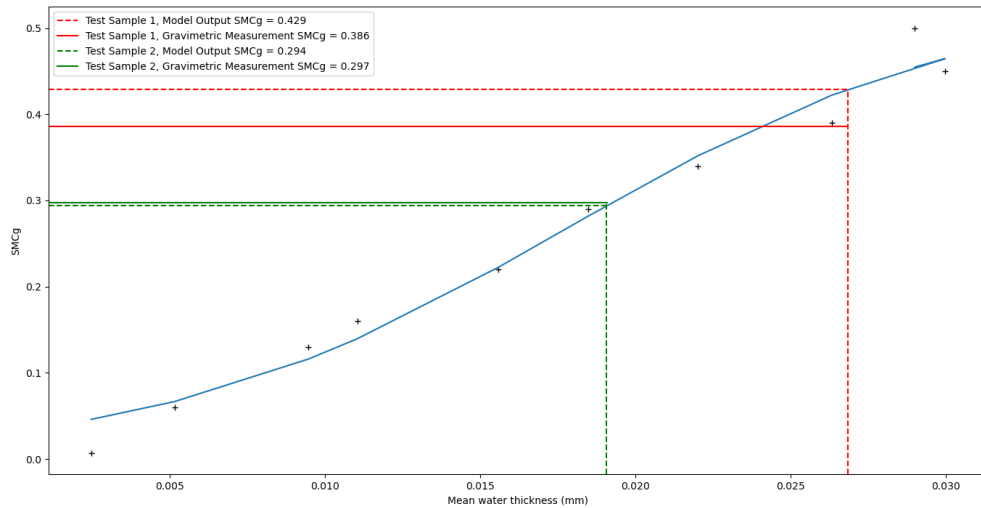


Figure 5.14: Estimated vs gravimetric soil moisture contents calculated for two test samples taken from another part of the field.

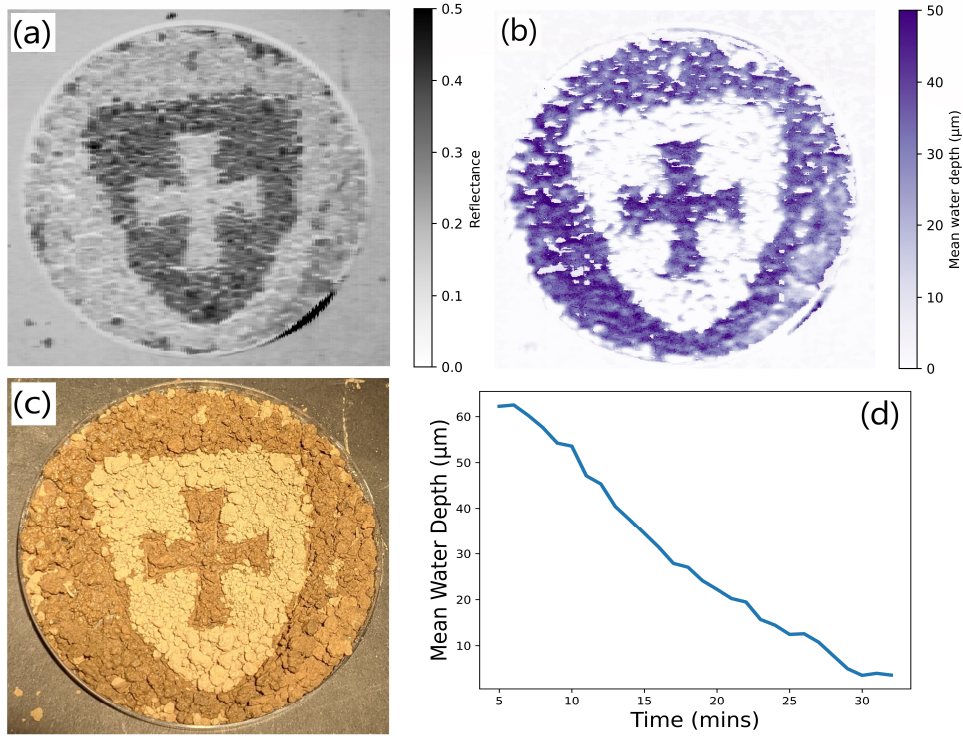


Figure 5.15: (a) Reflectance map of mixed wet and dry soil sample taken at 1440 nm. (b) Map of mean water depth (in micron), calculated excluding 1400 nm atmospheric absorption band. (c) Image of damp soil taken with a Pixel 4a. The petri dish has a diameter of 90 mm. (d) Mean water depth value calculated from MARMIT model decreasing monotonically with time. This was calculated as a mean of 100 spatial pixels in a 10x10 pixel square.

in Figure 5.15.

To test the use of the model under solar illumination, additional test samples were prepared. In order to use the model under natural illumination, data in the 1100-1180 nm and 1300-1500 nm bands was excluded from the fitting process, as atmospheric absorption at these wavelengths is strong. Under a clear sky, with strong summer mid-day sun, good results were obtained, with soil moisture estimates agreeing with lab results within 2% of absolute soil moisture content at a moisture level of 0.3 SMCg. At higher moisture contents, over 0.4 SMCg, the model consistently over estimates absolute soil water contents by 5%.

Under overcast conditions, an even smaller portion of the SWIR range is usable due to attenuation by the cloud cover. This is especially a problem for compact,

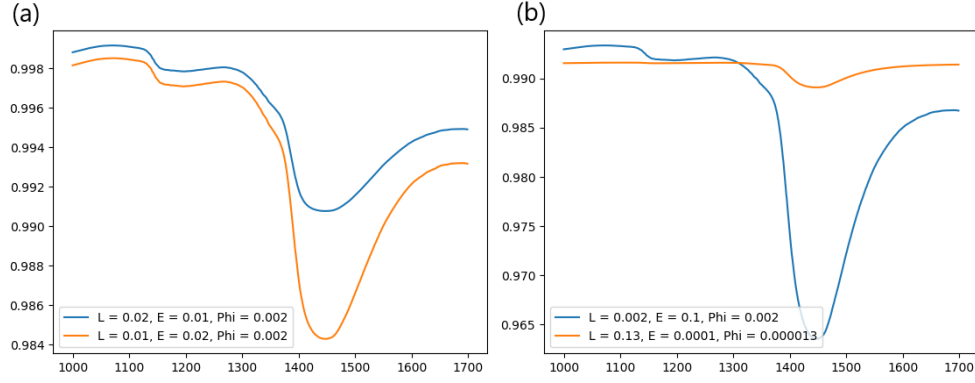


Figure 5.16: (a) Two lines with the same φ value, which don't overlap at any point. (b) Two lines with very different φ values, which do overlap and remain close in the 1200-1300 nm region. Both plots used a flat line at $y=1$ as a starting point.

low power hyperspectral imagers, which have less powerful sensor cooling leading to lower signal-to-noise ratios. The result is that the model fitting is restricted to an even smaller spectral bandwidth, with some groups fitting using a single wavelength. [78] Using the MARMIT model, two samples with the same mean water thickness can have very different spectra, and likewise two samples with widely differing mean water thickness can have their spectra overlap in some wavelength bands. This multi-valued nature of the model does not show up when fitting over large wavelength bands, but when using these small bandwidths the inversion method becomes very sensitive to initial conditions. To prevent the least squares fitting from getting trapped in local minima careful choice of the initial conditions and optimisation method is needed, which results in a method that requires significant manual input.

5.4.1 Method Discussion

For the analysis of the MARMIT model, a collection of different local soil samples were used, ranging from garden soil to farmland soil. Under laboratory conditions, the method was found to work well, especially with soils at low to mid levels of saturation. At high levels of saturation, the fit between the modelled and measured spectra would reduce, resulting in larger estimation errors during the inversion

process.

One quirk found was that for soils that have a very flat reflectance spectrum when dry, the model would have a hard time fitting the spectrum to a wet sample with a large water absorption feature. This could often be resolved by using the reflectance of a very slightly dampened sample as the "dry" spectrum, but indicates that the model's performance may vary significantly depending on soil type.

Atmospheric conditions restricting the spectral range for available for model fitting can also increase the error in soil moisture recovery. While this does not present so much of a problem in sunnier climates, or with cloudless satellite data, it does present an issue for use in cloudier temperate climates.

5.5 Conclusion

In this chapter, the data processing methods for creating corrected hyperspectral reflectance data sets are described, along with a demonstration of how this data can be used to remotely measure soil moisture content. In particular, application of both the HIAM model [98] and MARMIT model [72] are discussed in detail.

The process for recording and transforming the raw camera data into useful information is broadly similar for both lab and outdoor measurements. The main difference comes in correcting for variations in incident intensity due to intermittent cloud cover during solar illumination.

Two methods of measuring soil moisture content using this reflectance data have been investigated. MARMIT represents a radiative transfer model approach to soil moisture content measurements. In a lab setting, the MARMIT model was found to perform well. However, the effectiveness of the model was found to be dependant on soil type and sample preparation. This made the model difficult to apply to some local soil samples, and when comparing measurements made under solar illumination to those taken in the lab.

The HIAM spectral index model is also discussed. Initially developed using local soil samples, this model has been applied to a variety of soil samples under both laboratory and outdoor conditions. The RMSE for predicted soil moisture content was under 5% for all data sets. The method was more consistent across local soil samples, producing the expected linear fits from soil data sets where MARMIT struggled. From this comparison, it was decided that the HIAM model would be used going forward for other experiments.

Drone Integration

This chapter presents an overview of the use of the FYMOS hyperspectral imager onboard a custom UAV. The hardware changes required when moving to a UAV based system are detailed, along with a description of the changes in data processing required compared to ground based acquisitions. In particular, the process of generating geo-rectified hyperspectral data sets from GPS data is described, along with the methods for correcting distortions due to changes in the UAV platform's attitude.

6.1 Hardware Changes

When moving from a stationary laboratory based set up to one flying on a UAV, several hardware changes were necessary. Firstly, the large laptop running the system had to be replaced with a compact, low power single board computer (SBC). To minimise power requirements, a Linux based operating system was chosen. Initially, an Intel Atom based board (UP Board, x5-z8350 processor) was chosen to minimise power draw. However, the extremely low power processor was found to be too slow to continuously stream data to an attached USB 3.0 flash drive. This resulted in large time gaps during which no data was recorded, leading to large holes in data sets when flying over even a small area. Moving to a more powerful,

but still compact, Latte Panda Alpha 864 (Intel Core m3-8100y processor) solved this problem.

Issues were also found when using the USB flash drive to continuously save data during flight. While the USB drive would work at full speed on the ground with the rotors stopped, while flying the speed of the drive would dramatically decrease, and more errors in saved data could be seen. This was put down to the large amount of electromagnetic interference emitted by the four powerful drone motors. Switching to an PCIe Gen 4 NVMe drive attached directly to the SBC's M.2 slot has proved to be a more reliable configuration, while also significantly improving the performance of the drive.

Instead of carrying a separate power supply for the camera and computer systems, a 12 volt tap is taken from the main UAV power supply. An image of the system connected to a drone is shown in Figure 6.1. To prevent the camera from running constantly, consuming power and data storage, the system can be switched on and off using the flight controller. This can be manually toggled by the pilot using a remote controller, or be automatically toggled by the flight controller when flying along a series of way-points on autopilot.

6.2 UAV Data Collection

Compared to the process of collecting data in the lab, setting up a drone based aerial survey is more involved. To reduce battery capacity requirements, the shortest flight path required to cover the survey area should be calculated. This flight path should include some degree of overlap between contiguous scan lines, to ensure no areas of the field are missed during the scan. Planning and flying this precise flight path would be very challenging for a human pilot, especially in weather conditions with gusting or moderate winds.

Instead, flight planning and control software such as QGroundControl (see qground-control.com) can be used. This software can be used to plan aerial surveys, with a



Figure 6.1: Picture of FYMOS system attached to UAV in early testing.

screen shot shown in Figure 6.2. To plan a mission, the survey area is marked out, shown as the green rectangle. Options for altitude, degree of overlap, and survey direction can then be set, generating a flight plan shown in white. In areas with flight restrictions, such as nearby roads or buildings, geofences can be set up to prevent the aircraft from flying into these zones. Once the flight plan is created, it can be sent to a drone using a supported autopilot using the MAVLink protocol, ensuring the flight plan is followed precisely.

Before take off, the lens focus and aperture controls are set, along with the camera exposure time. The lens focus is generally set at infinity, which provides acceptable focus at the standard operating altitude of 30-50 metres. The lens aperture and exposure time are set using a 50% reflectance grey Spectralon panel. This should represent the most reflective natural object found on farmland, setting a level of exposure that should not get over-saturated under normal conditions.

Along with the hyperspectral data, it can be useful to collect standard RGB im-



Figure 6.2: Example capture of QGroundControl, software used to generate flight paths

agery of the target area, which can aid in reconstructing the full hyperspectral data cube. In order to do this, smaller drones such as the DJI Mavic Mini can be used, along with software such as Drone Harmony. The 2D images capture using this system can then be stitched into an orthomosaic using conventional image processing software.

6.3 UAV Data Processing

While the autopilot functions can keep the drone following a set path within a margin of error, it cannot keep the drone perfectly stable. In fact, the drone must roll and tilt to be able to move or turn at all! This motion affects the pointing of the camera system, making data post processing more complicated than just stacking up the recorded frames into a datacube. The attitude data from the drone's inertial measurement unit (IMU) and GPS loggers is recorded and timestamped alongside each frame, with the data used to calculate the angle that the camera lens was at relative to the ground being determined for each frame. The frames are then projected onto the location of the ground, and overlapped to create a georeferenced

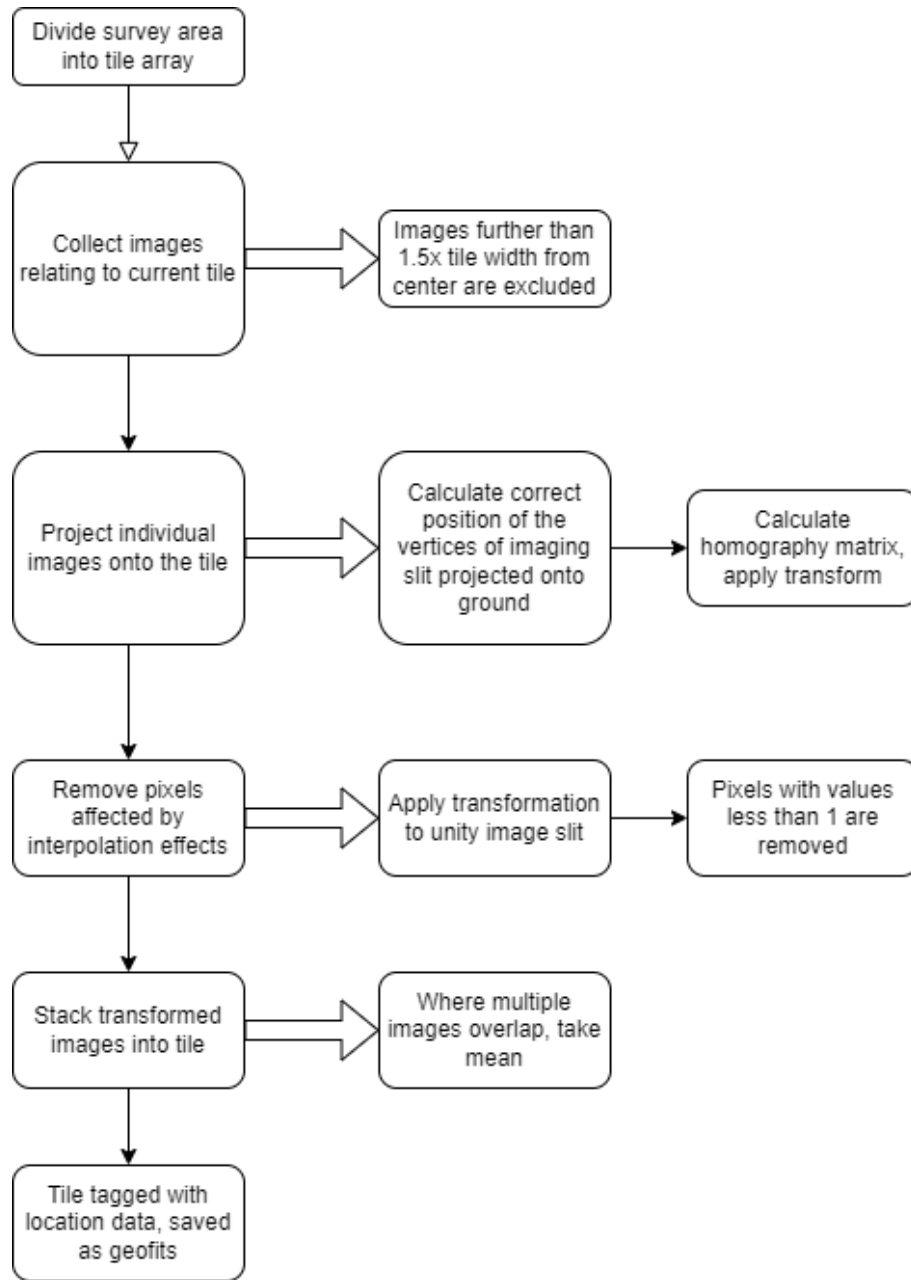


Figure 6.3: Flowchart detailing the processing pipeline for converting raw images taken with a UAV to geo-rectified images

image. A summary flow chart over viewing this method is shown in Figure 6.3.

In order to do this, firstly the area imaged by the UAV is split into an array of tiles, sized to reduce the volumes of data to process into smaller chunks. Once the tiles have been set, all image files relating to each tile are collected. To catch instances where the drone is positioned outside of the tile, but angled in such a way as to

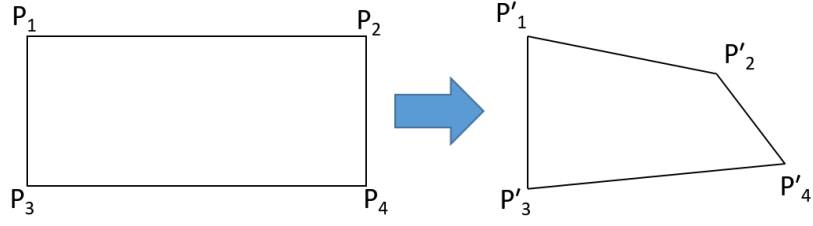


Figure 6.4: Generalised 2D Homographic transformation diagram placeholder

point the camera into the tile, images taken at a distance of up to 1.5 times the tile width from the centre of the tile are considered.

Following this, each image is projected onto the tile. Note that each image represents a line of spatial pixels, the combination of which forms the final two dimensional image tile. Each row of pixels represents a rectangular area on the ground. To calculate the correct transformation, the positions of the vertices of this rectangle are calculated using the latitude, longitude, pitch, roll and yaw data from the IMU. From these two sets of points, a homography transform matrix can be calculated. This matrix can then be used to map the rest of the pixels from the undistorted slit to the final image projection. The method of calculating this matrix follows.

Taking the point $P_1 = (x_1, y_1, 1)$ from Figure 6.4 as an example, a homography matrix H can be defined so that $P'_1 = HP_1$:

$$\begin{pmatrix} x'_1 \\ y'_1 \\ 1 \end{pmatrix} = \begin{pmatrix} h_{11} & h_{12} & h_{13} \\ h_{21} & h_{22} & h_{23} \\ h_{31} & h_{32} & h_{33} \end{pmatrix} \begin{pmatrix} x_1 \\ y_1 \\ 1 \end{pmatrix} \quad (6.1)$$

This can be rewritten as $P'_1 \times HP_1 = 0$, as the cross product of two identical vectors

is 0. By writing each row of the H matrix as h^{jT} , HP can be written as:

$$HP = \begin{pmatrix} h^{1T}P \\ h^{2T}P \\ h^{3T}P \end{pmatrix} \quad (6.2)$$

P' can be noted in a similar way, $P' = (x', y', z')$, giving

$$P'XHP = \begin{pmatrix} y'h^{3T}P - z'h^{2T}P \\ z'h^{1T}P - x'h^{3T}P \\ x'h^{2T}P - y'h^{1T}P \end{pmatrix} \quad (6.3)$$

As $h^{jT}P = P^T h^j$ for these matrices, this can be factored out into the form $Ah = 0$:

$$\begin{pmatrix} 0^T & -z'_i P_i^T & y'_i P_i^T \\ z'_i P_i^T & 0^T & -x'_i P_i^T \\ -y'_i P_i^T & x'_i P_i^T & 0^T \end{pmatrix} \begin{pmatrix} h^1 \\ h^2 \\ h^3 \end{pmatrix} = 0 \quad (6.4)$$

where x'_i is the x coordinate in point P'_i , represented in Figure 6.4. The last row of A is not linearly independent from the first two rows, and so can be omitted while solving for h . Filling in the rows for all 4 points gives

$$\begin{pmatrix} 0 & 0 & 0 & -x_1 & -y_1 & 1 & x_1 y'_1 & y_1 y'_1 & y'_1 \\ x_1 & y_1 & 1 & 0 & 0 & 0 & -x_1 x'_1 & -y_1 x'_1 & -x'_1 \\ & & & & & \vdots & & & \\ 0 & 0 & 0 & -x_4 & -y_4 & 1 & x_4 y'_4 & y_4 y'_4 & y'_4 \\ x_4 & y_4 & 1 & 0 & 0 & 0 & -x_4 x'_4 & -y_4 x'_4 & -x'_4 \end{pmatrix} \begin{pmatrix} h_{11} \\ h_{12} \\ \vdots \\ h_{32} \\ h_{33} \end{pmatrix} = 0 \quad (6.5)$$

As it is the relative values of elements in the H matrix that are important, rather than their absolute values, H can also be scaled so as one element (usually chosen as h_{33}) is equal to 1. This leaves a set of 8 linear equations and 8 unknowns, which can be solved. Homography perspective transforms can be calculated using

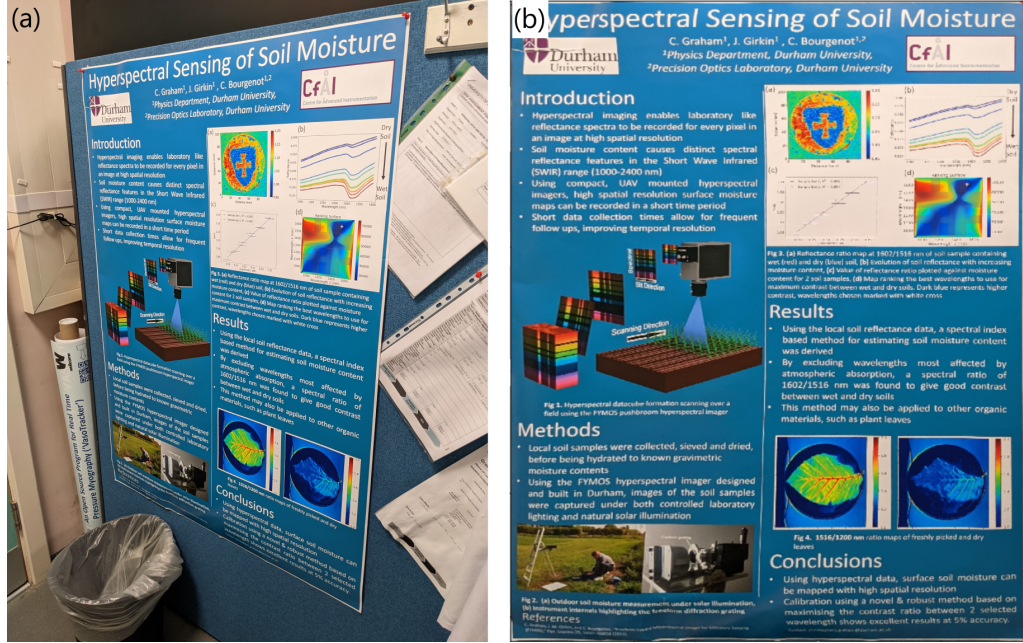


Figure 6.5: Example of an OpenCV perspective transform. Figure (a) shows an image of a poster taken at an angle with a smartphone. Figure (b) shows the transformed image to show the poster "square on".

functions in the Open CV library for Python. For more information on perspective transforms, see [108, 109].

To illustrate what this transform looks like in practice, Figure 6.5 shows an example made using a simple smartphone image. Figure (a) shows the original image of a poster, taken from an angle. Figure (b) shows the transformed image, warped and zoomed so as to give a "head-on" view of the poster, created using the same functions used for the UAV data processing pipeline.

Calculating the coordinates of the 4 corners required for the homography transform is more straightforward, using simple trigonometry. The geometry to do this is shown in Figure 6.6. To calculate the position of the point P'_2 , the positional offset u_x from in both x and y direction must be calculated. In the x direction, this is given by:

$$u_x = alt * \tan\left(\frac{FOV}{2} + Roll\right) \quad (6.6)$$

A similar equation is used for the y direction, using UAV pitch instead of roll. Once

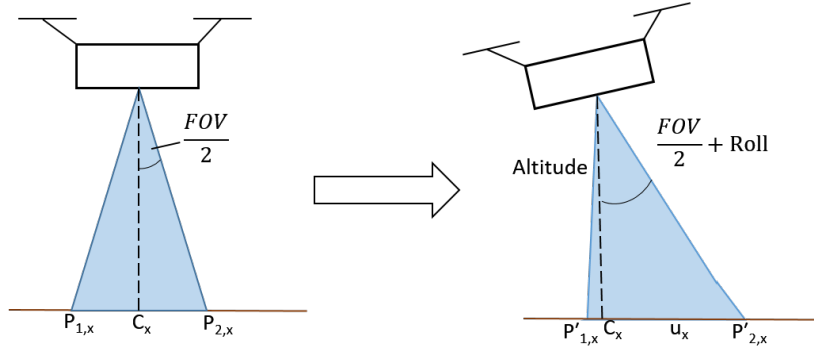


Figure 6.6: Geometry for calculating the coordinates of the vertices of the slit projection onto the ground in the x direction. The same geometry is used in the y direction, substituting roll for pitch.

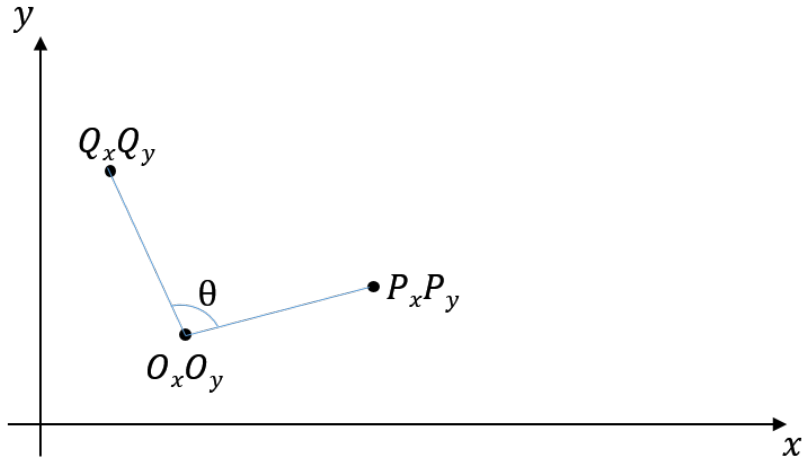


Figure 6.7: Calculating rotation around a point

these offsets have been calculated, they are then added to the centre coordinates of the rectangle (C_x, C_y) to find the corner coordinates. Finally, these corner coordinates are rotated around the centre point of the rectangle by the UAV's yaw value, again using simple trigonometry. Considering the example shown in Figure 6.7, the co-ordinates for point Q can be calculated as:

$$Q_x = O_x + (P_x - O_x)\cos(\theta) - (P_y - O_y)\sin(\theta) \quad (6.7)$$

$$Q_y = O_y + (P_x - O_x)\sin(\theta) + (P_y - O_y)\cos(\theta) \quad (6.8)$$

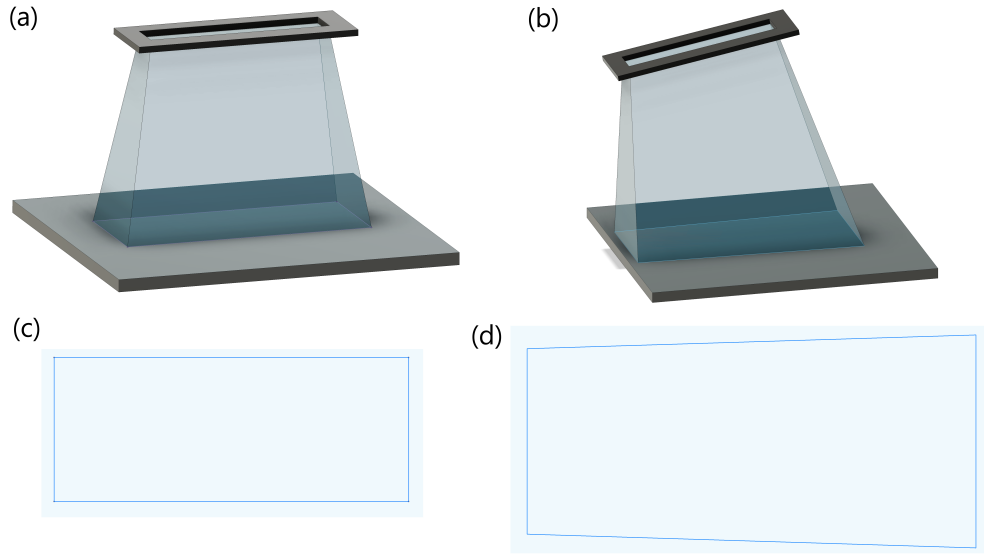


Figure 6.8: Figure demonstrating the change in shape of the entrance slit projection based on angle. (a) and (c) Illustrate the geometry and resultant slit projection for the slit positioned normal to the surface, while (b) and (d) show the same for an angled slit.

As the initial rectangular shape of the image will be different from the shape of the warped projection, the shape and area represented by each spatial pixel in a given image can vary. For the purposes of simplifying the data processing, the varying pixel shapes are not taken into account, with the assumption made that all pixels in initial and final images are square. This results in interpolation effects when the initial image from the camera is warped into the final ground image. Pixels affected by the interpolation are removed prior to final stacking. This change in shape is illustrated in Figure 6.8. When placing these projected images onto the final tile, there is a possibility of overlaps between neighbouring projections. Where pixels from two or more images overlap, the mean is taken.

The main simplification in this workflow is the assumption that the ground being imaged is flat. If the drone was flying above an angled surface, this would change the projection of the imaging slit onto the ground. Agricultural farmland generally does not feature steep gradients due to the impracticality of using large machinery on slopes, but this could be an issue in other applications. This could be addressed by projecting the images onto a digital terrain model, which can be created using

LiDAR measurements from a UAV. Provided there is no major soil erosion, grading, or land use change, these digital models may be used for several growing seasons before requiring updates.

Related to the above troubles with image distortions, the continuously varying attitude of the platform also causes issues with the fibre optic correction channel (Chapter 4), presenting the second major challenge for data processing. The diffuser on the end of the fibre, called the cosine corrector, accepts light from a 180° hemisphere, but its collection efficiency is angularly dependent. As the name suggests, the transmitted intensity is directly proportional to the cosine of the angle between the surface normal of the diffuser and the light source. In clear conditions, or in weather with scattered or broken cloud cover, this light source is the Sun, and so the angle between the Sun and the top of the drone must be recorded and accounted for at all times. During a measurement, this angle will have random variation due to wind gusting, and periodic variation due to changes in direction of the drone. Depending on the size of the UAV chassis, the UAV can angle by as much as 30 degrees in high wind conditions.

Using the Astropy Python module, the solar altitude and azimuthal angles can be calculated for a given time and location. As each image is tagged with the attitude data of the drone, the angle (θ) between the drone and the Sun can be calculated. The geometry for doing so is shown in Figure 6.9. Converting the polar coordinates into Cartesian vectors, the vectors for points P_1 and P_2 can be written as:

$$P_1 = \begin{pmatrix} \cos(A_1)\cos(\alpha_1) \\ \sin(A_1)\cos(\alpha_1) \\ \sin(\alpha_1) \end{pmatrix}, P_2 = \begin{pmatrix} \cos(A_2)\cos(\alpha_2) \\ \sin(A_2)\cos(\alpha_2) \\ \sin(\alpha_2) \end{pmatrix}$$

Considering a new "primed" coordinate system, rotated so that the angle $A'_1 = 0$, and $A'_2 = A_2 - A_1$, these vectors can be redefined as:

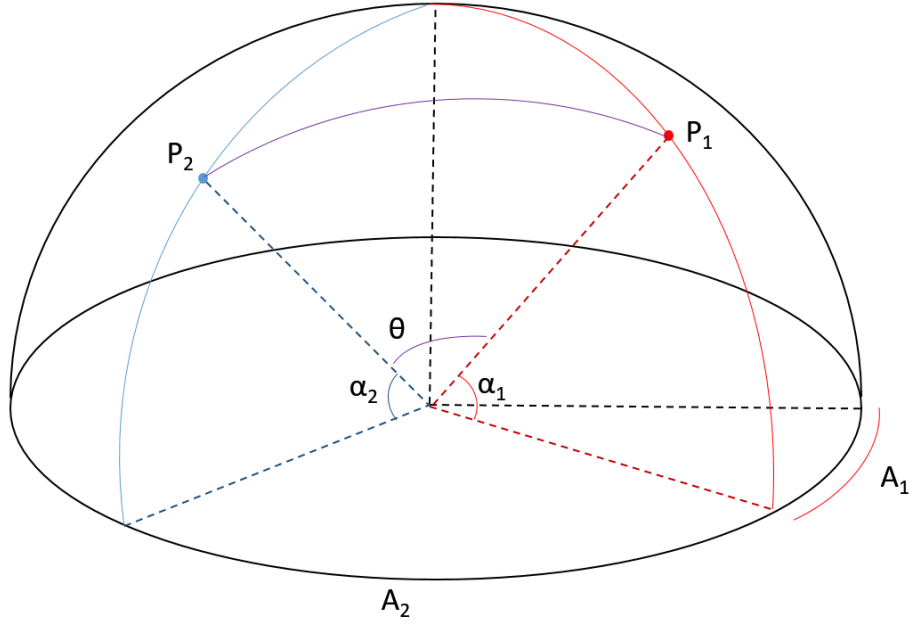


Figure 6.9: Geometry for calculating the scaling factor needed to account for the angle between the normal of the cosine corrector and the Sun.

$$P_1 = \begin{pmatrix} \cos(\alpha_1) \\ 0 \\ \sin(\alpha_1) \end{pmatrix}, P_2 = \begin{pmatrix} \cos(\alpha_2)\cos(A_2 - A_1) \\ \cos(\alpha_2)\sin(A_2 - A_1) \\ \sin(\alpha_2) \end{pmatrix}$$

To calculate the angle between these two, the dot product of these vectors can be calculated. As the magnitudes of the two vectors are both 1, the dot product $P_1 \cdot P_2 = \cos(\theta)$, which is exactly the scaling factor necessary for tilt correction. Computing this dot product gives:

$$\cos(\theta) = \sin(a_1)\sin(a_2) + \cos(a_1)\cos(a_2)\cos(A_2 - A_1) \quad (6.9)$$

where a_1 and a_2 are the altitude angles of the points P_1 and P_2 , and A_1 and A_2 are the respective azimuthal coordinates.

The main limitation to this method is when flying at times of lower solar elevation, when it is possible the face of the diffuser can be obscured from direct sunlight by its own shadow. In practice, this limitation is not severe, as low solar angles also

result in ground objects casting long shadows. In the example of ploughed land, this can result in most of the target field being obscured in shadow.

6.4 Conclusion

The work represented in this chapter was the most heavily affected by the COVID-19 pandemic. The organisation of drone flights over relevant targets requires the coordination of a large number of people, often across different research institutions and Universities. UAV flights are also very weather dependant, with the UAV unable to fly in rain or high winds. Coupling suitable conditions in the unpredictable British weather with the busy schedules of multiple research staff proved to be difficult, limiting the number of test flights that could be made.

This has limited the ability to trouble shoot some of the issues detailed in the chapter. Problems such as drive interference caused by the UAV's motors could not be spotted in the lab, where the drone's rotors are not switched on. Likewise, the data buffering issues with the slow processor on the original SBC were not obvious until extended flights were made with the full data logging system recording both camera and vehicle positioning data.

The result is that much of the immediate future work relating to this project stems from this chapter. With two prototypes of the instrument having been built, one instrument is available for flight testing while the other can be used for lab work. This should provide the ability to quickly deploy the UAV when suitable conditions come up.

Other agricultural uses

This section introduces the use of hyperspectral imagery in other areas of agricultural monitoring, specifically in direct leaf monitoring. The methods developed in Chapter 5 are applied to preliminary measurements of detached leaves, in order to develop methods for remote measurement of leaf moisture content.

7.1 Importance of Measuring Crop Stress

Outside of soil moisture, hyperspectral imagers have a wide variety of uses in agriculture. The main goal is to be able to remotely measure chemical and physical changes in plants which correlate to environmental stress with a high degree of accuracy. One of the more practical stress factors to control as a grower is water stress, which is associated with a wide range of effects on plant produce, especially in fleshy fruits. [110] Water stress has been linked to increased firmness in apples and pears, making the fruit more robust. [111] This decreases the risk of damage to the fruit in transit in modern supply chains, and increases shelf life. Water stress has also been linked to increased nutrition value of some fruit and vegetables, increasing the concentration of antioxidant compounds in broccoli. Understanding and controlling the benefits of controlled drought periods could be useful to regions most affected by climate change, where these techniques could help mitigate reduced access to irrigation water. [112]

However, precisely controlling the amount of stress a plant is subjected to can be difficult, with some staple crops like potatoes being very sensitive to small increases in water stress. [113] The use of standard point spectrometers in plant monitoring has been well documented, but has some drawbacks. Leaf clips allow for spectral measurements to be taken for precise locations on plants, but large surveys using these are slow and labour intensive. Using different optics to sample larger areas with these point spectrometers greatly reduces spatial resolution. The high spatial, high spectral resolution data provided by hyperspectral imaging provides an opportunity to remotely measure variations in reflectance across the leaves of one or more plants simultaneously.

7.1.1 Leaf Water Content Experiment

As an initial experiment to test the use of the FYMOS system a simple detached leaf water loss assay was performed using leaves taken from a bush near to Ogden Centre West. The freshly picked leaves were placed onto a lab balance connected to a computer, allowing for the mass of the leaf to be recorded automatically over time. The halogen lamp used for these measurements was placed 60 cm away from the leaves to reduce thermal infrared heating of the leaves. A time-lapse of the leaf drying out was then recorded, with the mass and reflectance of the leaf measured every 4 minutes for approximately 90 minutes. These measurements were taken with the uncooled Raptor Photonics SWIR camera, so 40 minutes prior to the start of the timelapse the camera was switched on to enable it to reach thermal equilibrium.

7.1.2 Results

This section is based on the same index selection analysis used in Section 5.3. Ideally, a ratio index would be found so that, when applied to a data-cube containing both a moist and a dry leaf, the resulting image histogram would be clearly

bi-modal. A demonstration of this is shown in Figure 7.1. Figure 7.1(a), shows the ratio of reflectance at 1564/1524 nm for a fresh leaf, while Figure 7.1(b) shows the same ratio but for a dry leaf. Figure 7.1(c) shows the histogram of ratio values for a 100x100 square pixel box at the centre of the leaf. The green peak corresponds to the fresh leaf, while the blue peak corresponds to the dry leaf.

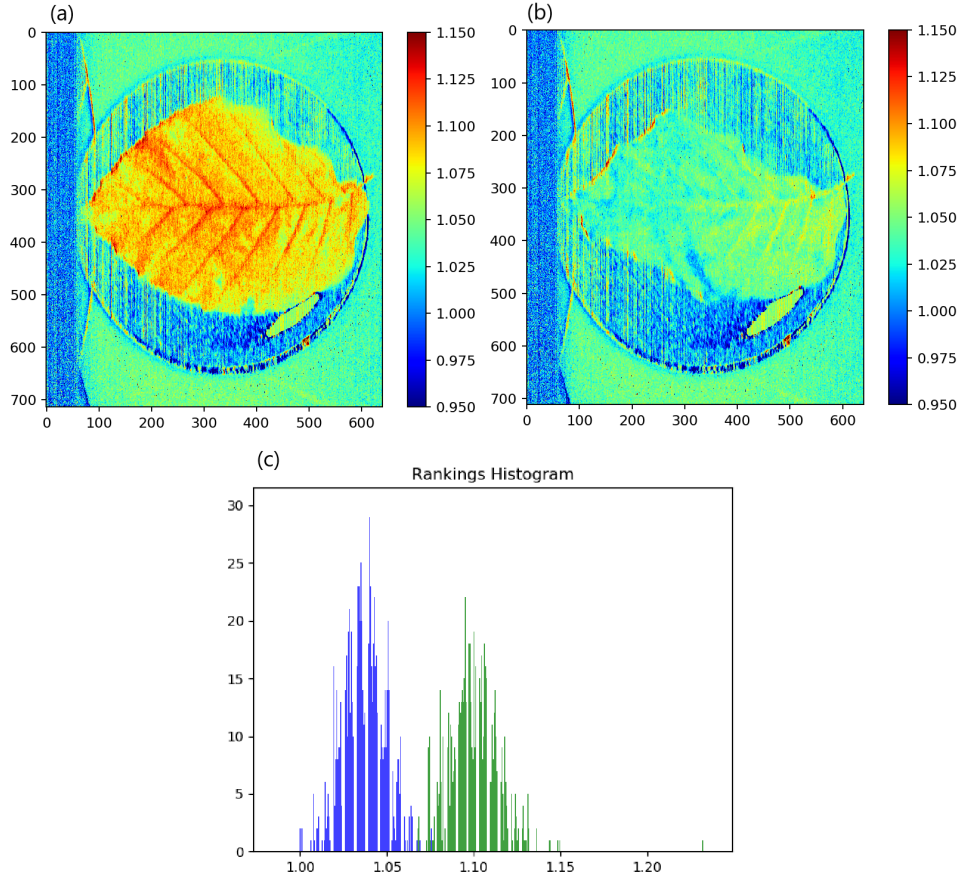


Figure 7.1: (a) Freshly picked leaf, (b) leaf after 90 minutes of drying, (c) histogram of ratios in a 100x100 pixel AOI in the centre of the leaf. The colour map represents the ratio of reflectance at 1564/1524 nm. The scales on the side indicates pixel numbers. For scale, the diameter of the plate under the leaf is 100 mm

The same process of generating contrast and standard deviation surface plots was followed, with Figure 7.2(a) showing the surface plot for a simple ratio of Wavelength 1/Wavelength 2, with lighter colours indicating higher separations. Figure 7.2(b) shows the standard deviation map for the leaves, with Figure 7.2(c) showing the overall ranking map, with darker colours indicating lower standard de-

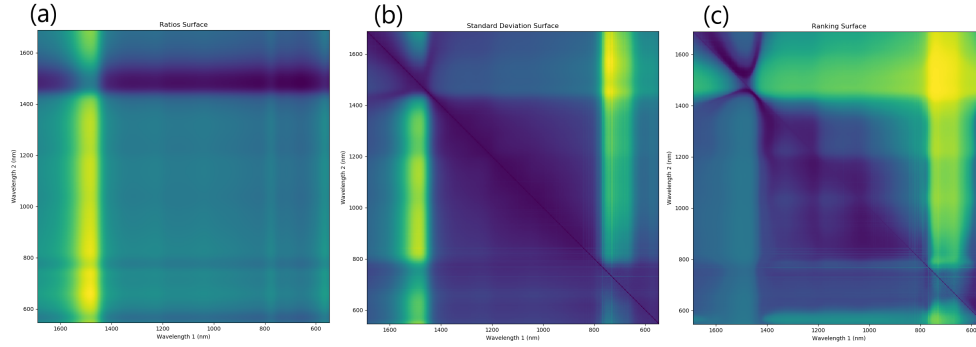


Figure 7.2: (a) Surface plot of 2 wavelength ratios between fresh and dry leaf, with brighter colours showing a larger difference between the leaves, (b) surface plot of standard deviation of wavelength ratios of the fresh leaf, with darker colours meaning a lower standard deviation, (c) overall ranking surface, with darker colours indicating the wavelength pairings best suited to differentiating fresh and dry leaves.

viations and better ranking respectively. For the leaves chosen for this experiment, a ratio of 1564/1524 nm was found to give good contrast.

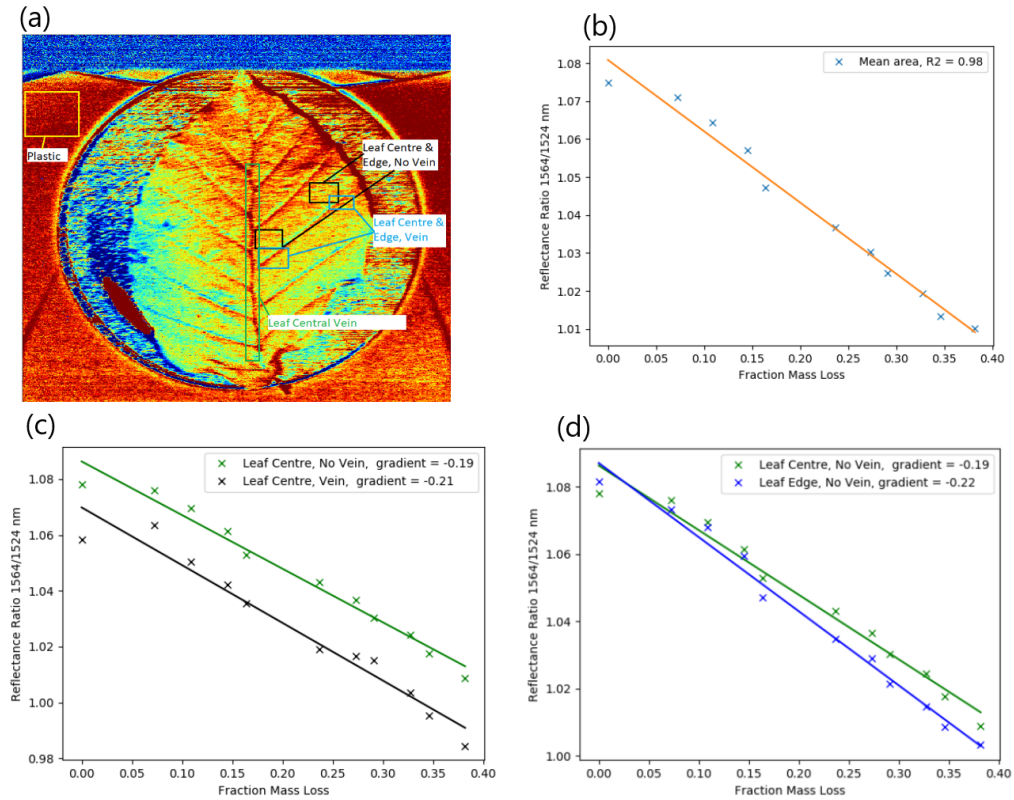


Figure 7.3: (a) Image of leaf, with areas of interest labeled, (b) Mean Ratio of leaf plotted against mass loss, (c) Comparing change in reflectance between leaf vein and lamina, (d) Comparing reflectance gradients of the lamina at the centre of the leaf and near the edge.

Figure 7.3(a) shows an example image of a fresh leaf at the chosen reflectance ratio. Focusing on an area of 10,000 pixels around the centre of the leaf, the mean reflectance ratio of the leaf was calculated for each step in the drying time-lapse. Plotted in Figure 7.3(b), the change in reflectance ratio correlates well with the fractional mass loss of the leaf in a linear fashion, with an R-Squared coefficient of 0.98. Using the high spatial resolution of a hyperspectral imager, it is possible to investigate how the change in reflectance differs between various areas on the leaf. Figure 7.3(c) shows a comparison between a leaf vein and lamina area close to the centre of the leaf, with the two showing a very similar gradient with an offset in reflectance ratio values. This offset may be due to the higher moisture level inside the veins. Meanwhile, comparing lamina areas at the centre of the leaf to the edge of the leaf, a difference in gradient is observed, shown in Figure 7.3(d). This could be explained by the varying cross sectional profile of the leaf, with the leaf being thickest in the centre and tapering towards the edges.

7.2 Conclusions

This section has introduced and discussed the application of remote soil sensing techniques to plant imaging. Using the method described in Chapter 5.3, the moisture content of detached leaves was measured, with the system able to capture the differing drying rates across the leaf lamina and vein structure.

This section was also affected by Covid, as a knock-on from delays in other areas. An ideal experiment would be to take a long time-lapse measurement of a plant being put under water stress, and then being watered correctly.

Conclusions

8.1 Summary

The main focus of this thesis was on the development of hyperspectral imaging technology, particularly aimed at compact instruments for use on UAVs in support of precision agriculture. The first objective was the optimisation of the geometrical aberrations and distortion (keystone and smile) of the spectrometer, by allowing the grating to take a freeform shape. The grating parameters were also optimised to deliver maximum efficiency over the InGaAs sensor's spectral range.

The second objective was to develop solutions for the challenges of using hyperspectral imagery in the temperate climate weather conditions found in the North-East of the UK. While the main body of work in this thesis is aimed at remote soil moisture content measurement, the broad spectral coverage of a hyperspectral imager enables the techniques discussed to be applied to other areas.

Chapter 3

Chapter 3 discusses the design of the FYMOS freeform Offner spectrograph, and compare its optical performances to other Offner type spectrographs utilising all spherical surfaces. By using of a freeform diffraction grating, a 30% decrease in RMS wavefront error in both the spatial and spectral fields was achieved in

comparison to an all spherical Offner Chrisp design. This work led to a publication in Optics Express:

"Christopher Graham, John M. Girkin, and Cyril Bourgenot, "Freeform based hYperspectral imager for MOisture Sensing (FYMOS)," *Optics Express* 29, 16007-16018 (2021)"

Chapter 4

Chapter 4 introduces the concept of an integrated fibre optic downwelling irradiance sensor, used for correcting reflectance measurements for the effects of changeable cloud cover. This technique is compared to other existing techniques in literature. The approach taken here is novel, using a fibre optic cable to feed light from a zenith facing diffuser directly into the entrance slit, creating a calibration channel for recording incident light levels without an additional spectrometer. This work resulted in a publication in Optics Express:

"Christopher Graham, John M. Girkin, and Cyril Bourgenot, "Integrated fiber optic spectrally resolved downwelling irradiance sensor for pushbroom spectrometers," *Optics Express* 30, 45592-45598 (2022)"

Chapter 5

Chapter 5 discusses the data collection and processing methods used to create and parse hyperspectral datasets under laboratory and outdoor ground testing conditions. Multiple methods of extracting soil moisture content from reflectance measurements have been tested, including both existing methods from literature and more novel techniques. The novelty in this approach comes from the focus of working under outdoor solar illumination. From this work, spectral index ratio methods were found to work the most consistently across different operating conditions. A method to determine the most suitable ratios, named HIAM, has been developed. This method has shown to offer a high dynamic range and contrast,

while being resilient to atmospheric absorption effects. Results from this chapter are published in Scientific Reports:

"Graham, C., Girkin, J. & Bourgenot, C. Spectral index selection method for remote moisture sensing under challenging illumination conditions. *Scientific Reports* 12, 14555 (2022)"

Chapter 6

Chapter 6 describes the mounting of the hyperspectral system to a UAV, along with the hardware and software requirements for running the system autonomously. The concepts behind geometrically correcting pushbroom images collected from an unstable platform are explained.

Chapter 7

Chapter 7 discusses the use of the FYMOS instrument for remote measurement of leaf moisture content. Applying a similar methods to those discussed in Chapter 5, the moisture content of detached leaves was estimated using spectral reflectance measurements. The use of the extended range dual channel setup for red edge imaging is also explored.

8.2 Future Work

The development path for for compact, UAV based hyperspectral imagers is extremely wide, leaving a large scope for further work on this topic.

Chapter 3

Regarding the optical design of the instrument, there is room for development, especially regarding optical throughput. In the FYMOS design, the primary and

tertiary mirrors are both spherical in design, sharing a common centre of curvature so as to be machined as a single monolithic piece to ease manufacturing. By combining the freeform diffraction grating with an Offner Chrisp style split mirror design, further improvements in the optical speed of the system could be found. This would reduce the camera exposure time required to image scenes in low light conditions, increasing the signal to noise ratio of the system.

Further improvements could be made to the optimisation of the diffraction grating. For the FYMOS design, the blaze angle of the grating was chosen to balance the grating efficiency at both ends of the camera's quantum efficiency curve. Now knowing that the most efficient wavelengths for determining soil moisture content lie in the 1500-1600 nm region, the blaze angle of the grating could be increased slightly to maximise the throughput in this range.

Away from pushbroom spectrometers, there is scope for research into other forms of hyperspectral imagers. The ease of use snapshot imagers provides strong motivation for developing these instruments. While current snapshot instruments are limited in both spatial and spectral resolution, much of this limitation derives from the small sensors available to compact camera manufacturers. Medium format sensors with global shutters are becoming available, which could enable compact IFU designs to be developed. The very high pixel counts of these sensors (with many over 100 megapixels) would also enable the production of filter array based snapshot imagers with high spatial and spectral resolutions. These systems could enable high resolution hyperspectral imagery to be recorded at video frame rates, which could be used in monitoring quickly changing scenes or processes.

Chapter 4

The fibre optic calibration channel is a fairly finalised concept. The biggest remaining issue with the design is that the manufacturing of the fibre guide is a very manual process, with both the bending of the needle fibre guide and the sanding

of the 3d printed bracket done by hand. The fibre positioning system could be improved and made simpler to manufacture, which would ease adoption if this integrated calibration unit becomes a critical component in future hyperspectral imagers.

Chapter 5

On the data analysis side, there is still plenty of work to be done on converting hyperspectral imagery into soil moisture maps. While the methods discussed in this paper have been demonstrated to work well in the lab, and have had limited testing in outdoor ground based experiments, they still need to be verified with data sampled from a drone. In particular, soil moisture retrieval over a large area involving pushbroom reconstruction, corrections for changing illumination conditions, soil heterogeneities, etc, all at once remains to be demonstrated.

All the of the data in this thesis relating to soil moisture has been captured on bare soils. While maintaining the correct soil moisture content is crucial during the germination and seedling stages of plant growth, it is also important during the ripening stages. This requires estimation of soil moisture content while the soil itself is not directly visible. There is an open question about whether soil moisture content may be accurately predicted using hyperspectral imagery of crop coverage. Investigating the link between crop reflectance and soil properties could be useful in monitoring soil moisture underneath perennial crops, such as in orchards or vineyards.

Chapter 6

The work relating to Chapter 6 was the most heavily impacted by the Covid-19 pandemic, with drone flights requiring physical collaboration by multiple people across research institutions. With the differing Covid safety regulations across these

organisations, this limited the opportunities for launching test flights in suitable locations.

With both the UAV and the data collection systems being new for the project, trouble shooting issues were expected. While most of these issues appear to now be solved, there is still a lack of usable flight data over an appropriate target. The main high impact work left to do related to this thesis is to fly the instrument of an area currently being sampled by other methods. This would enable the results from remotely sensed soil moisture to be compared directly to in-situ measurements in a field environment, which is the next important step in validating this approach for soil moisture measurement.

Chapter 7

Chapter 7 was also a casualty of the COVID-19 pandemic, with experiments in this chapter being squeezed in whenever time was found and access to the laboratory made possible. While hyperspectral imagery of plant leaves is well established, especially in visible wavelengths, SWIR hyperspectral imaging for the purpose of qualitative moisture content recovery is still an open research topic. Published literature has focused on detached leaf assays, with most live plant experiments being limited to clip-on point spectrometers. Time lapse recordings of plants being subjected to controlled water stresses could provide information on how hyperspectral data can be used to manage irrigation for plants. In the long term, larger field scale experiments combining hyperspectral imaging with precision irrigation and spraying techniques are needed to compare yield sizes and resource use against conventional farming practices. This would enable an accurate cost-benefit analysis of hyperspectral sensing and advanced precision agriculture techniques, and help to encourage farmers to take up these practices.

Route to operational model

Looking further ahead, the work from this thesis can be used to lay some of the ground work for larger scale deployments of the FYMOS system. The use of FYMOS in a commercial market could be split into two categories, based on the size and revenue of the target farms.

For the largest farms, many of which are already experimenting with automation and crop monitoring technologies, the still high barrier costs of full hyperspectral imaging systems may be affordable. These systems provide the most versatility, being capable of providing a range of data products such as soil and plant health metrics alongside soil moisture measurements. This widens their range of use from just being soil moisture measurement devices, and enables their use further into the growing season when soil may be obscured by vegetation. This is exemplified by the two channel FYMOS system, which has an expanded spectral range enabling both red-edge based plant health indicators and soil moisture metrics to be measured on a single <2 kg system. The additional versatility of these instruments compared to prior multispectral and hyperspectral systems means that fewer instrument changes will be needed during operations, reducing the system's down time.

For targeting smaller farms, FYMOS flights could be sold as a service. By looking at soil moisture variation across a field, issues such as slow or blocked drainage ditches can be highlighted quickly. FYMOS surveys could also be used in support of direct contact electrical sensors, such as by picking optimal positioning of soil sensors so as to get a more representative measurement of the whole field.

The disadvantage of the high spectral coverage of FYMOS is the high data volume associated with hyperspectral imaging. While some of the very largest and most automated farms may be equipped to store and process large data sets, for mass market appeal this needs to be mitigated. One option may be to develop and use more spectral index models such as HIAM, which are computationally easy to calculate. As small, single board computers become faster, it may be possible to

use the computer on board the UAV to process the data, and output simple data product maps, ready for interpretation by farmers. While storing only the preprocessed data maps removes the ability of retrospectively creating new products from the raw data, the file sizes for simple heatmaps are far smaller.

The second potential hurdle for commercialisation of the FYMOS instrument is the requirement for soil calibration samples to be collected and measured. To create the soil moisture-reflectance calibration curves, several samples of varying moisture contents need to be prepared, a process that can take 2-3 days. This issue is not unique to hyperspectral soil moisture measurement, as electrical soil probes also require calibration for optimal performance. Barring changes in land use, these calibrations should hold for several years, spreading the cost of these measurements. As government interest in soil health increases, projects like Northern Ireland's Soil Nutrient Health Scheme may also become more prevalent, enabling more robust models to be produced from much larger data sets. Post calibration, FYMOS/HIAM soil moisture estimates were found to have an uncertainty of 4.2%, which is on par with existing capacitance and resistance sensors. While impedance based sensors are still the gold standard of soil moisture measurement accuracy, the much larger area coverage of FYMOS measurements would give it a place in the market.

Bibliography

- [1] Stephen Bann. "When I was a photographer": Nadar and history, 2009.
- [2] Jayne Wilkinson. Animalizing the Apparatus: Pigeons, Drones and the Aerial View. *Shift: Graduate Journal of Visual and Material Culture*, (6):1–21, 2013.
- [3] Norris Pope. The reception of kodachrome sheet film in American commercial photography. *Technology and Culture*, 61(1):1–41, 2020.
- [4] Donald T. Lauer, Stanley A. Morain, and Vincent V. Salomonson. The landsat program: Its origins, evolution, and impacts. *Photogrammetric Engineering and Remote Sensing*, 63(7):831–838, 1997.
- [5] Jack C. Lansing, Jr. and Richard W. Cline. The Four- and Five-Band Multispectral Scanners for Landsat. *Optical Engineering*, 14(4):144312, 8 1975.
- [6] Jack L Engel and O Weinstein. The Thematic Mapper—An Overview. *IEEE Transactions on Geoscience and Remote Sensing*, GE-21(3):258–265, 1983.
- [7] M. Drusch, U. Del Bello, S. Carlier, O. Colin, V. Fernandez, F. Gascon, B. Hoersch, C. Isola, P. Laberinti, P. Martimort, A. Meygret, F. Spoto, O. Sy, F. Marchese, and P. Bargellini. Sentinel-2: ESA's Optical High-Resolution Mission for GMES Operational Services. *Remote Sensing of Environment*, 120:25–36, 2012.

- [8] Alexander F.H. Goetz, Gregg Vane, Jerry E. Solomon, and Barrett N. Rock. Imaging spectrometry for earth remote sensing. *Science*, 228(4704):1147–1153, 1985.
- [9] Gregg Vane, Alexander F.H. Goetz, and John B. Wellman. Airborne Imaging Spectrometer: a New Tool for Remote Sensing. *Digest - International Geoscience and Remote Sensing Symposium (IGARSS)*, 2(6):546–549, 1983.
- [10] Michael F. Gross and Vytautas Klemas. The use of Airborne Imaging Spectrometer (AIS) data to differentiate marsh vegetation. *Remote Sensing of Environment*, 19(1):97–103, 1986.
- [11] Gregg Vane, Robert O. Green, Thomas G. Chrien, Harry T. Enmark, Earl G. Hansen, and Wallace M. Porter. The airborne visible/infrared imaging spectrometer (AVIRIS). *Remote Sensing of Environment*, 44(2-3):127–143, 1993.
- [12] Alexander F.H. Goetz. Three decades of hyperspectral remote sensing of the Earth: A personal view. *Remote Sensing of Environment*, 113(SUPPL. 1):S5–S16, 2009.
- [13] NASA. Lewis Spins Out of Control. *System Failure Case Studies*, 1(8):1–4, 2007.
- [14] Stephen G. Ungar, Jay S. Pearlman, Jeffrey A. Mendenhall, and Dennis Reuter. Overview of the Earth Observing One (EO-1) mission. *IEEE Transactions on Geoscience and Remote Sensing*, 41(6 PART I):1149–1159, 2003.
- [15] John W. Chapman, David R. Thompson, Mark C. Helmlinger, Brian D. Bue, Robert O. Green, Michael L. Eastwood, Sven Geier, Winston Olson-Duvall, and Sarah R. Lundeen. Spectral and Radiometric Calibration of the Next Generation Airborne Visible Infrared Spectrometer (AVIRIS-NG). *Remote Sensing*, 11(18):2129, 9 2019.
- [16] Elia Vangi, Giovanni D’amico, Saverio Francini, Francesca Giannetti, Bruno Lasserre, Marco Marchetti, and Gherardo Chirici. The new hyperspectral

- satellite prisma: Imagery for forest types discrimination. *Sensors (Switzerland)*, 21(4):1–19, 2021.
- [17] M Rast, J Nieke, J Adams, C Isola, and F Gascon. COPERNICUS HYPER-SPECTRAL IMAGING MISSION FOR THE ENVIRON- MENT (CHIME). *International Geoscience and Remote Sensing Symposium (IGARSS)*, pages 108–111, 2021.
- [18] Christine M. Lee, Morgan L. Cable, Simon J. Hook, Robert O. Green, Susan L. Ustin, Daniel J. Mandl, and Elizabeth M. Middleton. An introduction to the NASA Hyperspectral InfraRed Imager (HyspIRI) mission and preparatory activities. *Remote Sensing of Environment*, 167:6–19, 2015.
- [19] Stephen K. Babey and Clifford D. Anger. Compact airborne spectrographic imager (CASI): a progress review. In Gregg Vane, editor, *Imaging Spectrometry of the Terrestrial Environment*, volume 1937, page 152, 9 1993.
- [20] Naiqian Zhang, Maohua Wang, and Ning Wang. Precision agriculture - A worldwide overview. *Computers and Electronics in Agriculture*, 36(2-3):113–132, 2002.
- [21] G. S. Hendricks, S. Shukla, F. M. Roka, R. P. Sishodia, T. A. Obreza, G. J. Hochmuth, and J. Colee. Economic and environmental consequences of over-fertilization under extreme weather conditions. *Journal of Soil and Water Conservation*, 74(2):160–171, 2019.
- [22] Jonathan A. Foley, Ruth DeFries, Gregory P. Asner, Carol Barford, Gordon Bonan, Stephen R. Carpenter, F. Stuart Chapin, Michael T. Coe, Gretchen C. Daily, Holly K. Gibbs, Joseph H. Helkowski, Tracey Holloway, Erica A. Howard, Christopher J. Kucharik, Chad Monfreda, Jonathan A. Patz, I. Colin Prentice, Navin Ramankutty, and Peter K. Snyder. Global consequences of land use. *Science*, 309(5734):570–574, 2005.

- [23] Paul J.A. Withers, Colin Neal, Helen P. Jarvie, and Donnacha G. Doody. Agriculture and eutrophication: Where do we go from here? *Sustainability (Switzerland)*, 6(9):5853–5875, 2014.
- [24] Elena M. Bennett, Stephen R. Carpenter, and Nina F. Caraco. Human impact on erodable phosphorus and eutrophication: A global perspective. *BioScience*, 51(3):227–234, 2001.
- [25] John Boardman. Soil erosion in britain: Updating the record. *Agriculture (Switzerland)*, 3(3):418–442, 2013.
- [26] Jerry W. Knox, Melvyn G. Kay, Tim M. Hess, and Ian P. Holman. The challenges of developing an irrigation strategy for UK agriculture and horticulture in 2020: Industry and research priorities. *CAB Reviews: Perspectives in Agriculture, Veterinary Science, Nutrition and Natural Resources*, 15(50), 2020.
- [27] Stanley Wood, Kate Sebastian, and Sara Scherr. *Pilot analysis of global ecosystems: agroecosystems, a joint study by International Food Policy Research Institute and World Resources Institute*. 2000.
- [28] Rui Machado and Ricardo Serralheiro. Soil Salinity: Effect on Vegetable Crop Growth. Management Practices to Prevent and Mitigate Soil Salinization. *Horticulturae*, 3(2):30, 5 2017.
- [29] Alexandratos N. and J. Bruinsma. WORLD AGRICULTURE TOWARDS 2030 / 2050 The 2012 Revision. *ESA Working paper*, 12(03):146, 2012.
- [30] Olakunle Elijah, Tharek Abdul Rahman, Igbafe Orikumhi, Chee Yen Leow, and Mhd Nour Hindia. An Overview of Internet of Things (IoT) and Data Analytics in Agriculture: Benefits and Challenges. *IEEE Internet of Things Journal*, 5(5):3758–3773, 2018.

- [31] Jorge A. Delgado, Nicholas M. Short, Daniel P. Roberts, and Bruce Vandenberg. Big Data Analysis for Sustainable Agriculture on a Geospatial Cloud Framework. *Frontiers in Sustainable Food Systems*, 3(July), 2019.
- [32] Carolyn B. Hedley and Ian J. Yule. Soil water status mapping and two variable-rate irrigation scenarios. *Precision Agriculture*, 10(4):342–355, 2009.
- [33] F. M. Ziadat and A. Y. Taimeh. Effect of rainfall intensity, slope, land use and antecedent soil moisture on soil erosion in an arid environment. *Land Degradation and Development*, 24(6):582–590, 2013.
- [34] Bikash R. Parida, W. B. Collado, R. Borah, M. K. Hazarika, and L. Samarakoon. Detecting drought-prone areas of rice agriculture using a MODIS-derived soil moisture index. *GIScience and Remote Sensing*, 45(1):109–129, 2008.
- [35] Jing Yuan, Xin Wang, Chang-xiang Yan, Shu-rong Wang, Xue-ping Ju, and Yi Li. Soil Moisture Retrieval Model for Remote Sensing Using Reflected Hyperspectral Information. *Remote Sensing*, 11(3):366, 2 2019.
- [36] Willem W. Verstraeten, Frank Veroustraete, and Jan Feyen. Assessment of evapotranspiration and soil moisture content across different scales of observation. *Sensors*, 8(1):70–117, 2008.
- [37] R. Tognetti, R. d’Andria, A. Lavini, and G. Morelli. The effect of deficit irrigation on crop yield and vegetative development of *Olea europaea* L. (cvs. Frantoio and Leccino). *European Journal of Agronomy*, 25(4):356–364, 2006.
- [38] Vincent Humphrey, Alexis Berg, Philippe Ciais, Pierre Gentine, Martin Jung, Markus Reichstein, Sonia I. Seneviratne, and Christian Frankenberg. Soil moisture–atmosphere feedback dominates land carbon uptake variability. *Nature*, 592(7852):65–69, 2021.
- [39] Dongqin Yin, Michael L. Roderick, Guy Leech, Fubao Sun, and Yuefei Huang. The contribution of reduction in evaporative cooling to higher surface air

- temperatures during drought. *Geophysical Research Letters*, 41(22):7891–7897, 2014.
- [40] T. J. Dean, J. P. Bell, and A. J.B. Baty. Soil moisture measurement by an improved capacitance technique, Part I. Sensor design and performance. *Journal of Hydrology*, 93(1-2):67–78, 1987.
- [41] H. R. Bogaen, J. A. Huisman, C. Oberdörster, and H. Vereecken. Evaluation of a low-cost soil water content sensor for wireless network applications. *Journal of Hydrology*, 344(1-2):32–42, 2007.
- [42] Fawwaz T. Ulaby. Radar Measurement of Soil Moisture Content. *IEEE Transactions on Antennas and Propagation*, 22(2):257–265, 1974.
- [43] Dara Entekhabi, Eni Njoku, Peggy O’Neill, Kent Kellogg, and Jared Entin. The NASA Soil Moisture Active Passive (SMAP) mission formulation. *International Geoscience and Remote Sensing Symposium (IGARSS)*, pages 2302–2305, 2011.
- [44] Yann H. Kerr, Philippe Waldteufel, Jean Pierre Wigneron, Jean Michel Martinuzzi, Jordi Font, and Michael Berger. Soil moisture retrieval from space: The Soil Moisture and Ocean Salinity (SMOS) mission. *IEEE Transactions on Geoscience and Remote Sensing*, 39(8):1729–1735, 2001.
- [45] Jiang Hongtao, Shen Huanfeng, Li Xinghua, Zeng Chao, Liu Huiqin, and Lei Fangni. Extending the SMAP 9-km soil moisture product using a spatio-temporal fusion model. *Remote Sensing of Environment*, 231(May):111224, 2019.
- [46] Dianjun Zhang and Guoqing Zhou. Estimation of soil moisture from optical and thermal remote sensing: A review. *Sensors (Switzerland)*, 16(8), 2016.
- [47] S. Chabrillat, E. Ben-Dor, J. Cierniewski, C. Gomez, T. Schmid, and B. van Wesemael. *Imaging Spectroscopy for Soil Mapping and Monitoring*, volume 40. Springer Netherlands, 2019.

- [48] Dimosthenis C. Tsouros, Stamatia Bibi, and Panagiotis G. Sarigiannidis. A review on UAV-based applications for precision agriculture. *Information (Switzerland)*, 10(11), 2019.
- [49] M. Zreda, W. J. Shuttleworth, X. Zeng, C. Zweck, D. Desilets, T. Franz, and R. Rosolem. COSMOS: The cosmic-ray soil moisture observing system. *Hydrology and Earth System Sciences*, 16(11):4079–4099, 2012.
- [50] Marek Zreda, Darin Desilets, T. P.A. Ferré, and Russell L. Scott. Measuring soil moisture content non-invasively at intermediate spatial scale using cosmic-ray neutrons. *Geophysical Research Letters*, 35(21):1–5, 2008.
- [51] Fred Sigernes, Mikko Syrjäsoo, Rune Storvold, João Fortuna, Mariusz Eivind Grøtte, and Tor Arne Johansen. Do it yourself hyperspectral imager for handheld to airborne operations. *Optics Express*, 26(5):6021, 2018.
- [52] Pilar Gonzalez, Julien Pichette, Bart Vereecke, Bart Masschelein, Andy Lambrechts, Leonid Krasovitski, and Leonid Bikov. An extremely compact and high-speed line-scan hyperspectral imager covering the SWIR range. *SPIE-Intl Soc Optical Eng*, (May 2018):19, 2018.
- [53] NEELAM Gupta. ACOUSTO-OPTIC TUNABLE FILTERS. *Optics and Photonics News*, 8(11):23, 11 1997.
- [54] Y. Inoue and J. Penuelas. An AOTF-based hyperspectral imaging system for field use in ecophysiological and agricultural applications. *International Journal of Remote Sensing*, 22(18):3883–3888, 2001.
- [55] Nathan Hagen, Robert T Kester, Liang Gao, and Tomasz S. Tkaczyk. Snapshot advantage: a review of the light collection improvement for parallel high-dimensional measurement systems. *Optical Engineering*, 51(11):111702, 6 2012.
- [56] Neelam Gupta, Philip R. Ashe, and Songsheng Tan. Miniature snapshot multispectral imager. *Optical Engineering*, 50(3):033203, 2011.

- [57] Kang Zhu, Yujia Xue, Qiang Fu, Sing Bing Kang, Xilin Chen, and Jingyi Yu. Hyperspectral light field stereo matching. *IEEE Transactions on Pattern Analysis and Machine Intelligence*, 41(5):1131–1143, 2019.
- [58] Grigorios Tsagkatakis, Maarten Bloemen, Bert Geelen, Murali Jayapala, and Panagiotis Tsakalides. Graph and Rank Regularized Matrix Recovery for Snapshot Spectral Image Demosaicing. *IEEE Transactions on Computational Imaging*, 5(2):301–316, 6 2019.
- [59] J. L. Beuzit, A Vigan, D Mouillet, K Dohlen, R Gratton, A Boccaletti, J. F. Sauvage, H M Schmid, M. Langlois, C. Petit, A. Baruffolo, M. Feldt, J. Milli, Z. Wahhaj, L. Abe, U. Anselmi, J. Antichi, R. Barette, J. Baudrand, P. Baudoz, A. Bazzon, P. Bernardi, P. Blanchard, R. Brast, P. Bruno, T. Buey, M. Carbillet, M. Carle, E. Cascone, F. Chapron, J. Charton, G. Chauvin, R. Claudi, A. Costille, V. De Caprio, J. De Boer, A. Delboulb , S. Desidera, C. Dominik, M. Downing, O. Dupuis, C. Fabron, D. Fantinel, G. Farisato, P. Feautrier, E. Fedrigo, T. Fusco, P. Gigan, C. Ginski, J. Girard, E. Giro, D. Gisler, L. Gluck, C. Gry, T. Henning, N. Hubin, E. Hugot, S. Incorvaia, M. Jaquet, M. Kasper, E. Lagadec, A. M. Lagrange, H. Le Coroller, D. Le Mignant, B. Le Ruyet, G. Lessio, J. L. Lizon, M. Llored, L. Lundin, F. Madec, Y. Magnard, M. Marteaud, P. Martinez, D. Maurel, F. M nard, D. Mesa, O. M ller-Nilsson, T. Moulin, C. Moutou, A. Orign , J. Parisot, A. Pavlov, D. Perret, J. Pragt, P. Puget, P. Rabou, J. Ramos, J. M. Reess, F. Rigal, S. Rochat, R. Roelfsema, G. Rousset, A. Roux, M. Saisse, B. Salasnich, E. Santambrogio, S. Scuderi, D. Segransan, A. Sevin, R. Siebenmorgen, C. Soenke, E. Stadler, M. Suarez, D. Tiph ne, M. Turatto, S. Udry, F. Vakili, L. B.F.M. Waters, L. Weber, F. Wildi, G. Zins, and A. Zurlo. SPHERE: The exoplanet imager for the Very Large Telescope. *Astronomy and Astrophysics*, 631:A155, 11 2019.
- [60] Kevin Bundy, Matthew A. Bershady, David R. Law, Renbin Yan, Niv Drory,

- Nicholas MacDonald, David A. Wake, Brian Cherinka, José R. Sánchez-Gallego, Anne Marie Weijmans, Daniel Thomas, Christy Tremonti, Karen Masters, Lodovico Coccato, Aleksandar M. Diamond-Stanic, Alfonso Aragón-Salamanca, Vladimir Avila-Reese, Carles Badenes, Jesús Falcón-Barroso, Francesco Belfiore, Dmitry Bizyaev, Guillermo A. Blanc, Joss Bland-Hawthorn, Michael R. Blanton, Joel R. Brownstein, Nell Byler, Michele Cappellari, Charlie Conroy, Aaron A. Dutton, Eric Emsellem, James Etherington, Peter M. Frinchaboy, Hai Fu, James E. Gunn, Paul Harding, Evelyn J. Johnston, Guinevere Kauffmann, Karen Kinemuchi, Mark A. Klaene, Johan H. Knapen, Alexie Leauthaud, Cheng Li, Lihwai Lin, Roberto Maiolino, Viktor Malanushenko, Elena Malanushenko, Shude Mao, Claudia Maraston, Richard M. McDermid, Michael R. Merrifield, Robert C. Nichol, Daniel Oravetz, Kaike Pan, John K. Parejko, Sebastian F. Sanchez, David Schlegel, Audrey Simmons, Oliver Steele, Matthias Steinmetz, Karun Thanjavur, Benjamin A. Thompson, Jeremy L. Tinker, Remco C.E. Van Den Bosch, Kyle B. Westfall, David Wilkinson, Shelley Wright, Ting Xiao, and Kai Zhang. Overview of the SDSS-IV MaNGA survey: Mapping Nearby Galaxies at Apache Point Observatory. *Astrophysical Journal*, 798(1), 2015.
- [61] E. Prieto and S. Vivès. A proposal of image slicer designed for integral field spectroscopy with NIRSpec/JSWT. *New Astronomy Reviews*, 50(4-5):279–284, 2006.
- [62] S. J. Zhang, S. To, Z. W. Zhu, and G. Q. Zhang. A review of fly cutting applied to surface generation in ultra-precision machining. *International Journal of Machine Tools and Manufacture*, 103:13–27, 2016.
- [63] Shahrokh Hatefi and Khaled Abou-El-Hossein. Review of single-point diamond turning process in terms of ultra-precision optical surface roughness. *International Journal of Advanced Manufacturing Technology*, 106(5-6):2167–2187, 2020.

- [64] Kent F. Palmer and Dudley Williams. Optical Properties of Water in the Near Infrared. *J Opt Soc Am*, 64(8):1107–1110, 1974.
- [65] W. R. Whalley, P. B. Leeds-Harrison, and G. E. Bowman. Estimation of soil moisture status using near infrared reflectance. *Hydrological Processes*, 5(3):321–327, 1991.
- [66] Ross Bryant, David Thoma, Susan Moran, David Goodrich, Tim Keefer, Ginger Paige, and Susan Skirvin. Evaluation of Hyperspectral , Infrared Temperature and Radar Measurements for Monitoring Surface Soil Moisture. *Proceedings of the First Interagency Conference on Research in the Watersheds, Benson, Arizona, 27-30 October 2003*, page 528–533, 2003.
- [67] Sophie Fabre, Xavier Briottet, and Audrey Lesaignoux. Estimation of soil moisture content from the spectral reflectance of bare soils in the 0.4–2.5 μm domain. *Sensors (Switzerland)*, 15(2):3262–3281, 2015.
- [68] Ramakrishna Nemani, Lars Pierce, Steve Running, and Samuel Goward. Developing Satellite-derived Estimates of Surface Moisture Status. *Journal of Applied Meteorology*, 32(3):548–557, 3 1993.
- [69] Morteza Sadeghi, Ebrahim Babaeian, Markus Tuller, and Scott B. Jones. The optical trapezoid model: A novel approach to remote sensing of soil moisture applied to Sentinel-2 and Landsat-8 observations. *Remote Sensing of Environment*, 198:52–68, 2017.
- [70] Ebrahim Babaeian, Morteza Sadeghi, Trenton E. Franz, Scott Jones, and Markus Tuller. Mapping soil moisture with the OPTical TRAPezoid Model (OPTRAM) based on long-term MODIS observations. *Remote Sensing of Environment*, 211(April):425–440, 2018.
- [71] Anders Ångström. The Albedo of Various Surfaces of Ground. *Geografiska Annaler*, 7(1925):323, 1925.

- [72] A. Bablet, P. V.H. Vu, S. Jacquemoud, F. Viallefont-Robinet, S. Fabre, X. Briottet, M. Sadeghi, M. L. Whiting, F. Baret, and J. Tian. MARMIT: A multilayer radiative transfer model of soil reflectance to estimate surface soil moisture content in the solar domain (400–2500 nm). *Remote Sensing of Environment*, 217(August):1–17, 2018.
- [73] Frank Stern. Transmission of Isotropic Radiation Across an Interface Between Two Dielectrics. *Applied Optics*, 3(1):111, 1964.
- [74] Eyal Ben Dor, Cindy Ong, and Ian C. Lau. Reflectance measurements of soils in the laboratory: Standards and protocols. *Geoderma*, 245-246:112–124, 5 2015.
- [75] Sabine Chabrillat, Asa Gholizadeh, Carsten Neumann, Daniel Berger, Robert Milewski, Yaron Ogen, and Eyal Ben-Dor. Preparing a soil spectral library using the Internal Soil Standard (ISS) method: Influence of extreme different humidity laboratory conditions. *Geoderma*, 355(August):113855, 12 2019.
- [76] Asa Gholizadeh, Carsten Neumann, Sabine Chabrillat, Bas van Wesemael, Fabio Castaldi, Luboš Borůvka, Jonathan Sanderman, Aleš Klement, and Christian Hohmann. Soil organic carbon estimation using VNIR–SWIR spectroscopy: The effect of multiple sensors and scanning conditions. *Soil and Tillage Research*, 211(July 2020), 2021.
- [77] Yufeng Ge, Cristine L.S. Morgan, Sabine Grunwald, David J. Brown, and Deoyani V. Sarkhot. Comparison of soil reflectance spectra and calibration models obtained using multiple spectrometers. *Geoderma*, 161(3-4):202–211, 2011.
- [78] Rehman S. Eon and Charles M. Bachmann. Mapping barrier island soil moisture using a radiative transfer model of hyperspectral imagery from an unmanned aerial system. *Scientific Reports*, 11(1):1–11, 2021.

- [79] Christopher Graham, John M. Girkin, and Cyril Bourgenot. Freeform based hYperspectral imager for MOisture Sensing (FYMOS). *Optics Express*, 29(11):16007, 5 2021.
- [80] William T. Plummer. Unusual optics of the Polaroid SX-70 Land camera. *Applied Optics*, 21(2):196, 1982.
- [81] Kevin P. Thompson and Jannick P. Rolland. Freeform Optical Surfaces: A Revolution in Imaging Optical Design. *Optics and Photonics News*, 23(6):30, 2012.
- [82] Dewen Cheng, Yongtian Wang, Hong Hua, and M. M. Talha. Design of an optical see-through head-mounted display with a low f-number and large field of view using a freeform prism. *Applied Optics*, 48(14):2655, 2009.
- [83] Robert R. Boye, William C. Sweatt, Bradley H. Jared, Aaron M. Ison, Edward G. Winrow, Michael P. Saavedra, and Jeffery P. Hunt. Design of head-mounted binoculars utilizing freeform surfaces. *Optical Engineering*, 53(3):031310, 2013.
- [84] Kyle Fuerschbach, Jannick P. Rolland, and Kevin P. Thompson. A new family of optical systems employing ϕ -polynomial surfaces. *Optics Express*, 19(22):21919, 2011.
- [85] Martin P J Lavery, David J Robertson, Gregorius C G Berkhout, Gordon D Love, Miles J Padgett, and Johannes Courtial. Refractive elements for the measurement of the orbital angular momentum of a single photon. *Optics Express*, 20(3):2110, 1 2012.
- [86] S Barbero and J Rubinstein. Adjustable-focus lenses based on the Alvarez principle. *Journal of Optics*, 13(12):125705, 2011.
- [87] Fabian Duerr, Youri Meuret, and Hugo Thienpont. Potential benefits of freeform optics in on-axis imaging applications with high aspect ratio. *Optics Express*, 21(25):31072, 2013.

- [88] Daniel Vukobratovich and John P. Schaefer. Large stable aluminum optics for aerospace applications. *Optomechanics 2011: Innovations and Solutions*, 8125(September 2011):81250T, 2011.
- [89] Yuan-Chieh Cheng, Wei-Yao Hsu, Khaled Abou-El-Hossein, Oluwale Olu-fayo, and Timothy Otieno. Investigation of diamond turning: of rapidly so-lidified aluminum alloys. *Current Developments in Lens Design and Optical Engineering XV*, 9192(September 2014):919214, 2014.
- [90] Laurens Katgerman and Fred Dom. Rapidly solidified aluminium alloys by meltspinning. *Materials Science and Engineering A*, 375-377(1-2 SPEC. ISS.):1212–1216, 2004.
- [91] Guido P. H. Gubbels, Bart W. H. van Venrooy, Albert J. Bosch, and Ro-ger Senden. Rapidly solidified aluminium for optical applications. *Ad-vanced Optical and Mechanical Technologies in Telescopes and Instrumenta-tion*, 7018(July 2008):70183A, 2008.
- [92] C. Bourgenot, D. J. Robertson, D. Stelter, and S. Eikenberry. Towards free-form curved blazed gratings using diamond machining. In *Advances in Optical and Mechanical Technologies for Telescopes and Instrumentation II*, volume 9912, page 99123M, 2016.
- [93] Coralie De Clercq, Vincent Moreau, Jean-François Jamoye, Alessandro Zuc-caro Marchi, and Pierre Gloesener. ELOIS: an innovative spectrometer design using a free-form grating. *Optical Systems Design 2015: Optical Design and Engineering VI*, 9626(September 2015):96261O, 2015.
- [94] W. T. Welford. *Aberrations of Optical Systems*. Routledge, New York, 1st edition, 11 1986.
- [95] Jacob Reimers, Aaron Bauer, Kevin P Thompson, and Jannick P Rolland. Freeform spectrometer enabling increased compactness. *Light: Science & Applications*, 6(7):e17026–e17026, 2017.

- [96] Paul Jerram and James Beletic. Teledyne’s high performance infrared detectors for Space missions. In Nikos Karafolas, Zoran Sodnik, and Bruno Cugny, editors, *International Conference on Space Optics — ICSO 2018*, volume 11180, page 120. SPIE, 7 2019.
- [97] Luwei Feng, Zhou Zhang, Yuchi Ma, Qingyun Du, Parker Williams, Jessica Drewry, and Brian Luck. Alfalfa Yield Prediction Using UAV-Based Hyperspectral Imagery and Ensemble Learning. *Remote Sensing*, 12(12):2028, 6 2020.
- [98] Christopher Graham, John Girkin, and Cyril Bourgenot. Spectral index selection method for remote moisture sensing under challenging illumination conditions. *Scientific Reports*, (0123456789):1–9, 2022.
- [99] Kebiao Mao, Zijin Yuan, Zhiyuan Zuo, Tongren Xu, Xinyi Shen, and Chunyu Gao. Changes in Global Cloud Cover Based on Remote Sensing Data from 2003 to 2012. *Chinese Geographical Science*, 29(2):306–315, 2019.
- [100] Christian J. Köppl, Radu Malureanu, Carsten Dam-Hansen, Sheng Wang, Hongxiao Jin, Stefano Barchiesi, Juan M. Serrano Sandí, Rafael Muñoz-Carpena, Mark Johnson, Ana M. Durán-Quesada, Peter Bauer-Gottwein, Ursula S. McKnight, and Monica Garcia. Hyperspectral reflectance measurements from UAS under intermittent clouds: Correcting irradiance measurements for sensor tilt. *Remote Sensing of Environment*, 267(February), 2021.
- [101] Helge Aasen and Andreas Bolten. Multi-temporal high-resolution imaging spectroscopy with hyperspectral 2D imagers – From theory to application. *Remote Sensing of Environment*, 205(February 2016):374–389, 2018.
- [102] Andreas Burkart, Sergio Cogliati, Anke Schickling, and Uwe Rascher. A novel UAV-Based ultra-light weight spectrometer for field spectroscopy. *IEEE Sensors Journal*, 14(1):62–67, 2014.

- [103] Juha Suomalainen, Teemu Hakala, Raquel Alves de Oliveira, Lauri Markelin, Niko Viljanen, Roope Näsi, and Eija Honkavaara. A novel tilt correction technique for irradiance sensors and spectrometers on-board unmanned aerial vehicles. *Remote Sensing*, 10(12):1–18, 2018.
- [104] David M. Kim, Hairong Zhang, Haiying Zhou, Tommy Du, Qian Wu, Todd C. Mockler, and Mikhail Y. Berezin. Highly sensitive image-derived indices of water-stressed plants using hyperspectral imaging in SWIR and histogram analysis. *Scientific Reports*, 5(September):1–11, 2015.
- [105] F. X. Kneizys, E. P. Shettle, and W. O. Gallery. Atmospheric Transmittance And Radiance: The LOWTRAN 5 Code. In Robert W. Fan, editor, *AFGL-TR-0177*, number August, pages 116–124, 7 1981.
- [106] Christopher Graham, John M. Girkin, and Cyril Bourgenot. Freeform based hYperspectral imager for MOisture Sensing (FYMOS). *Optics InfoBase Conference Papers*, 29(11):16007–16018, 2021.
- [107] A. Dupiau, S. Jacquemoud, X. Briottet, S. Fabre, F. Viallefont-Robinet, W. Philpot, C. Di Biagio, M. Hébert, and P. Formenti. MARMIT-2: An improved version of the MARMIT model to predict soil reflectance as a function of surface water content in the solar domain. *Remote Sensing of Environment*, 272(April 2022):112951, 2022.
- [108] Richard Hartley and Andrew Zisserman. Estimation – 2D Projective Transformations. In *Multiple View Geometry in Computer Vision*, pages 87–131. Cambridge University Press, 3 2004.
- [109] Richard Hartley and Andrew Zisserman. Scene planes and homographies. *Multiple View Geometry in Computer Vision*, pages 325–343, 2011.
- [110] Julie Ripoll, Laurent Urban, Michael Staudt, Félicie Lopez-Lauri, Luc P.R. Bidel, and Nadia Bertin. Water shortage and quality of fleshy fruits-making

- the most of the unavoidable. *Journal of Experimental Botany*, 65(15):4097–4117, 2014.
- [111] Leonardo Nora, Gabriel O., Fabiana R., and Cesar V. Controlled Water Stress to Improve Fruit and Vegetable Postharvest Quality. *Water Stress*, 2012.
- [112] J.P. Mitchell, C. Shennan, S.R. Grattan, and D.M. May. Tomato Fruit Yields and Quality under Water Deficit and Salinity. *Journal of the American Society for Horticultural Science*, 116(2):215–221, 2019.
- [113] Sermet Onder, Mehmet Emin Caliskan, Derya Onder, and Sevgi Caliskan. Different irrigation methods and water stress effects on potato yield and yield components. *Agricultural Water Management*, 73(1):73–86, 2005.

Colophon

This thesis is based on a template developed by Matthew Townson and Andrew Reeves. It was typeset with \LaTeX 2 ϵ . It was created using the *memoir* package, maintained by Lars Madsen, with the *madsen* chapter style. The font used is Latin Modern, derived from fonts designed by Donald E. Kuth.